



# Contrast-enhanced MRI using nanosystems

Dissertation  
zur Erlangung des Grades  
"Doktor der Naturwissenschaften"  
im Promotionsfach Chemie

am Fachbereich Chemie, Pharmazie und Geowissenschaften  
der Johannes Gutenberg-Universität Mainz

Sandro Ebert

geb. in Mainz

Mainz, 2015

---

Dekan: Herr Prof. Dr. Holger Frey

1. Berichterstatter: Frau Prof. Dr. Katharina Landfester

2. Berichterstatter: Herr Prof. Dr. Wolfgang Tremel

Tag der mündlichen Prüfung:

---

# Contents

<b>1</b>	<b>Introduction</b>	<b>5</b>
<b>2</b>	<b>Theory</b>	<b>7</b>
2.1	Longitudinal and transverse relaxation . . . . .	7
2.2	Correlation and spectral density functions . . . . .	8
2.3	Relaxation mechanisms . . . . .	12
2.4	Relaxation induced by paramagnetic species . . . . .	12
2.5	Superparamagnetism . . . . .	13
2.6	MRI fundamentals . . . . .	14
2.7	Comparison between positive and negative contrast agents . . . . .	17
<b>3</b>	<b>Methods and materials</b>	<b>20</b>
3.1	NMR scanner . . . . .	20
3.2	NMR relaxation rates . . . . .	21
3.3	Diffusion measurements . . . . .	22
3.4	MRI pulse sequence . . . . .	22
3.5	Exchange measurements . . . . .	23
3.6	NMR Dispersion . . . . .	25
<b>4</b>	<b>Results and Discussion</b>	<b>26</b>
4.1	Positive contrast agents . . . . .	26
4.1.1	Theory of longitudinal relaxivity . . . . .	26
4.1.2	Relaxivity in solution . . . . .	31
4.1.3	High relaxivity in nanocapsules . . . . .	40
4.1.4	Increasing relaxivity by co-encapsulation . . . . .	51
4.1.5	Exchange of water in and out of nanocapsules . . . . .	51
4.1.6	In vivo imaging . . . . .	57

4.2	Negative contrast agents . . . . .	61
4.2.1	Introduction of the systems . . . . .	61
4.2.2	Theory and simulation of transverse relaxivity . . . . .	62
4.2.3	The unified approach . . . . .	69
4.2.4	Results and discussion . . . . .	71
<b>5</b>	<b>Summary</b>	<b>77</b>
<b>6</b>	<b>Zusammenfassung</b>	<b>79</b>
<b>7</b>	<b>Experimental and Simulations</b>	<b>81</b>
7.1	Positive contrast agents . . . . .	81
7.1.1	Relaxivity in solution - Simulation . . . . .	81
7.1.2	Relaxivity for different diffusion coefficients . . . . .	84
7.1.3	Relaxivity for unloaded nanocapsules . . . . .	86
7.1.4	In vivo experiments . . . . .	86
<b>8</b>	<b>Appendix</b>	<b>87</b>
8.1	Abbreviations . . . . .	87
8.2	Parameters . . . . .	88
8.3	Matlab code . . . . .	89
8.3.1	Automatic evaluation of relaxation times . . . . .	89
8.3.2	Relaxivity in solution for different viscosities . . . . .	92
8.3.3	Negative contrast agents - Matlab code . . . . .	97
	<b>Bibliography</b>	<b>102</b>

---

# 1 Introduction

Since the first use of nuclear magnetic resonance for tumor detection<sup>1</sup> and the first imaging of objects,<sup>2</sup> magnetic resonance imaging has become a powerful tool in medicine. Whereas the first images of human anatomy were clearly a tremendous success,<sup>3</sup> it turned out that the use of contrast agents (CA) can highly improve the performance and functionality of MRI.<sup>4,5</sup> Though extremely successful, the true potential of MRI lies still ahead with its use as a molecular imaging method.<sup>6</sup> There are more sophisticated approaches under investigation to gain a high local contrast in MR images, like hyperpolarization techniques<sup>7</sup> or chemical shift imaging,<sup>8</sup> which however mostly are still under investigation or have not made it yet to daily routine in clinics. Apart from these more sophisticated approaches, clinically approved CA actually alter either the  $T_1$  or the  $T_2$  relaxation time of nearby proton spins.<sup>9,10</sup> The key parameter of these CA is the relaxivity, which is a measure of how bright or dark a signal appears in the image.

Contrast agents, that alter the  $T_1$  time, also referred to as positive contrast agents, give a bright signal in the image and are mostly based on gadolinium complexes. In fact and right now, all of the U.S Food and Drug Administration (FDA) approved CA and which are commercially available are of this kind.<sup>11</sup> The second class of CA reduces the  $T_2^*$  time, cancel the signal and give rise to black spots in the image and hence are also known as negative contrast agents. These CA are mostly composed from iron oxide. Although there are many  $T_2^*$  contrast agents which are FDA approved, nowadays there is none on the market, due to poor demand.<sup>11</sup> However, research in this area is still active and of increasing interest, since iron oxide CA are potentially less toxic than the ones based on gadolinium.<sup>11</sup>

The development of MRI to a molecular imaging method calls for contrast agents, that have relaxation rates which exceed the relaxation rate of clinical approved agents by several orders of magnitude. A synthetical trial and error approach however is becoming more and more unlikely to achieve high relaxivities. Hence, more effort is put on the understanding of relaxation mechanisms generating a high MRI contrast.

Different approaches have been developed to achieve high relaxivity  $T_1$  CA.<sup>9, 12, 13</sup> All of them have in common, that the rotation of the contrast agent complex is changed.<sup>14–17</sup> Another kind of  $T_1$  CA are gadolinium complexes, that are encapsulated in polymeric nanocapsules (NC).<sup>18</sup> In this thesis, the FDA approved CA Gadovist is encapsulated and the resulting NC are studied as potential high relaxivity CA, by investigating and analyzing important parameters for the special circumstances that arise through the encapsulation. First, relaxivities are investigated in different polymer solutions and for different conditions like different magnetic fields and temperatures. Then, different capsule compositions will be investigated to reveal their ability to work as high relaxivity CA. They will be measured by several NMR techniques and compared to each other and to neat Gadovist solution. The findings from the measurements in different polymer solutions will then be used, to further tune the relaxivity to even higher values. Eventually, *in-vivo* imaging experiments will demonstrate the feasibility of these contrast agents to tune the contrast in living objects and prove their potential for medical applications.

For  $T_2^*$  contrast agents, mostly superparamagnetic iron oxides (SPIO) are used, for which the transversal relaxivity rate  $r_2$  is the key parameter. SPIOs can possess high magnetization values and thus strongly affect  $T_2^*$ . Therefore, they are ideal candidates for MRI examinations.<sup>19</sup> Since the first reports of SPIO size dependent relaxivities a lot of progress has been made in this area to understand and tune the relaxivities to ever higher values.<sup>20–22</sup> However, the combination of a high contrast in imaging and a targeted drug delivery makes SPIOs encapsulated in nanocarriers very promising and fascinating candidates as molecular contrast agents.<sup>6, 23, 24</sup> In this work, several SPIO based particle systems, including nanocapsules, are investigated with a focus on the understanding of NC as high relaxivity  $T_2^*$  CA. First, the particular relaxivities are simulated with theoretical approaches which are designed for the understanding of SPIO clusters and nanoparticles (NP).<sup>10, 25, 26</sup> In a second step, the relaxivities are simulated using a different approach, namely with an empirical equation found by Monte Carlo (MC) simulations, in which the special conditions arising through the encapsulation process are included.<sup>27</sup> Finally, both theoretical approaches and their outcome will be compared with experimental results, again to evaluate the potential of nanocapsules as high relaxivity contrast agents.

---

## 2 Theory

In this chapter the underlying physics of  $T_1$  and  $T_2$  relaxation with and without contrast agents will be presented. It starts by explaining the concept of relaxation in NMR and the different sources of relaxation. A more detailed theory for different relaxation mechanisms will be introduced in the respective sections in the result chapter. Subsequently the theoretical concept of relaxivity is introduced in section 2.1 as a measure for the effectiveness of contrast agents. Thereafter the basics of MRI will be briefly introduced. Eventually, the difference between  $T_1$  and  $T_2$  contrast agents will be elucidated and demonstrated by *in vitro* imaging.

### 2.1 Longitudinal and transverse relaxation

Nuclear magnetic resonance is based on the splitting of nuclear energy states in a magnetic field  $B_0$ .<sup>28-31</sup> The splitting of the energy levels arises from the Zeeman interaction of the nuclear spin and the external field.<sup>28,30</sup> At thermal equilibrium the energy levels possess slightly different spin populations which follow the Boltzmann distribution. This population difference gives rise to a longitudinal magnetization, mostly referred to as z-Magnetization  $M_z$ . The energy difference between the levels is given by the so called Larmor frequency  $\omega_0$ , which is given by

$$\omega_0 = \gamma_I B_0 \quad (2.1)$$

where  $\gamma_I$  is the gyromagnetic ratio of the nucleus. With radio frequency (RF) pulses which match the Larmor frequency, it is possible to saturate the transition between the energy levels which results in the loss of longitudinal magnetization. The nuclear spins under investigation will also undergo thermal motion and feel the local magnetic field induced by other molecules.<sup>29</sup> If the thermal motion makes the local field induced by other molecules oscillate close to the Larmor frequency, the spin will be rotated into a new direction, similar to applying an RF pulse. Since the spins have a higher energy after applying an RF pulse, this thermal motion induced relaxation is a natural way of losing this energy and coming back to thermal

equilibrium. Hence, this relaxation is connected with a change of energy and it is the thermal energy of a system, with which the spin energy comes into equilibrium. This mechanism is called longitudinal relaxation and the time constant for this process is the  $T_1$  relaxation time. The inverse of the  $T_1$  time is the  $T_1$  relaxation rate constant  $R_1$ , which is a measure for how fast the magnetization comes back to thermal equilibrium. At equilibrium, the magnetization has only a z component. But directly after a  $90^\circ$  pulse exists no z component, but only x and y components in the transverse plane, see also Figure 2.1. These components give

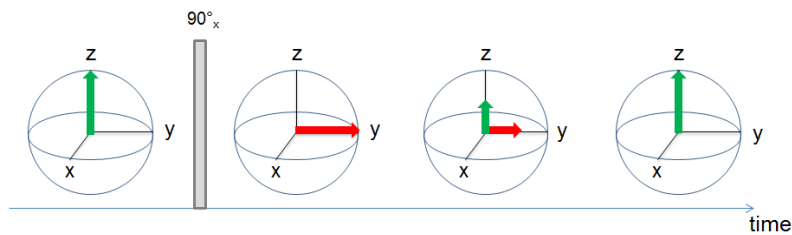


Figure 2.1: At equilibrium it exists only a magnetization in z direction, indicated by the green arrow. After a  $90^\circ$  pulse (gray bar), there are only components in the x and y plane. Over time, the magnetization in the x/y plane relaxes to zero, whereas the magnetization in z-direction builds up again, thus recovering the thermal equilibrium.

rise to a transverse magnetization in x/y plane.<sup>29</sup> Of course, thermal motion and therefore oscillating local fields can again bring these magnetic components into new directions. But more importantly, because of local fields in z-direction, which change the external magnetic field, different spins will precess at different Larmor frequencies. They will therefore dephase in the x/y plane and lose their coherence between each other. This kind of relaxation is called transverse relaxation or  $T_2$  relaxation. Analog to  $R_1$  the inverse of the  $T_2$  time is  $R_2$ . Unlike the longitudinal relaxation, the transverse relaxation is not causing any energy change in the system.

## 2.2 Correlation and spectral density functions

Since the thermal motion in the end gives rise to the relaxation of magnetic moments, a measure is needed, which describes how fast and effective the reorientation of spins take place. This can be done by correlation times and the corresponding functions.<sup>29</sup> The corre-



lation time  $\tau_c$  describes how long it takes for an ensemble of spins to reorient their magnetic moments by a certain degree. If a spin  $i$  experiences at a time  $t$  a field  $B_i(t)$  and because of thermal motion at a time  $t + \tau$  a different field  $B_i(t + \tau)$ , the so called correlation function  $G(t, \tau)$  is the ensemble average over  $N$  spins<sup>29</sup>

$$G(t, \tau) = \frac{1}{N} \sum_{i=1}^N B_i(t)B_i(t + \tau) = \overline{B(t)B(t + \tau)} \quad (2.2)$$

For long times  $\tau$  the local fields will have all kind of orientations, such that the average over the whole sample will be zero and hence the correlation function will be zero. Since the exact point at which the observation starts is not of interest, the time point  $t$  usually is set to zero. The correlation function then can be written as  $G(\tau)$ . For  $\tau = 0$ , the correlation function is simply

$$G(0) = \overline{B^2} \quad (2.3)$$

If the molecules are assumed to be spherical, the correlation function decays exponentially<sup>29</sup>

$$G(\tau) = \overline{B^2} e^{-\frac{\tau}{\tau_c}} \quad (2.4)$$

where  $\tau_c$  is the correlation time, characteristic for the motion of the spin. However,  $\tau_c$  is yet unspecified. Apart from other reasons, it is important that the local field oscillates close to the Larmor frequency to be an efficient source of relaxation. Therefore it is interesting to have a function, describes this effect in the frequency domain rather than the time domain. This gives rise to the spectral density function  $J(\omega)$ , which is connected with the correlation function via a Fourier transformation  $FT$ <sup>29</sup>

$$J(\omega) = FT(G(\tau)) = \overline{B^2} \frac{2\tau_c}{1 + \omega^2\tau_c^2} \quad (2.5)$$

The general behavior of these functions is shown in Figure 2.2. As one can see, the correlation function decays faster for shorter correlation times  $\tau_c$ . And the spectral density function decays faster for longer  $\tau_c$ , whereas for short  $\tau_c$  the spectral density function shows a broad distribution of frequencies. However, only frequencies lead to reorientations which are close to the Larmor frequency  $\omega_0$ . Hence, the spectral density function at the Larmor frequency

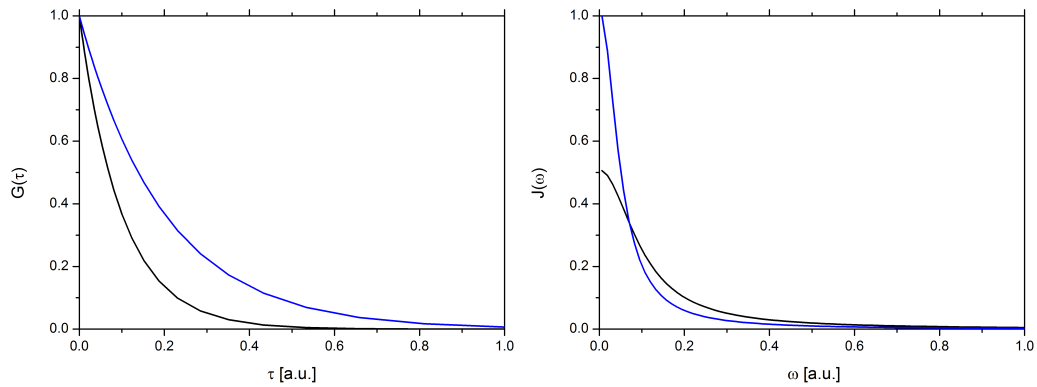


Figure 2.2: Left: Correlation function for two different correlation times  $\tau_c$ . For the blue curve, the correlation time  $\tau_c$  is chosen two times longer than for the black curve. Right: Spectral density function for two different correlation times. Again, for the blue curve, the correlation time  $\tau_c$  is chosen two times longer than for the black curve.

is relevant for relaxation processes,

$$J(\omega_0) = \overline{B^2} \frac{2\tau_c}{1 + \omega_0^2 \tau_c^2} \quad (2.6)$$

It can be easily verified, that the maximum of the spectral density is reached for  $\omega_0 \tau_c = 1$ , which is equivalent to  $\tau_c = 1/\omega_0$ . Interestingly the relaxation rate  $R$  is proportional to the spectral density function  $J(\omega_0)$ . It should be mentioned that  $B$  is the strength of the local field, which is very high for paramagnetic species and if the field changes at the right frequency due to thermal motion, this resembles a highly efficient source of relaxation. If  $B$  as well as the correlation time is known, the relaxation rate can be calculated with help of equation 2.6. In the result chapter, the spectral density functions and  $B$  will be calculated explicitly. As already mentioned, the relaxation mechanisms relevant for  $T_1$  relaxation can also drive the transverse magnetization to equilibrium. However, in case of transversal relaxation, a second mechanism exists. Since the relaxing spins will not only feel the external magnetic field  $B_0$  but in addition the z-component of local fields, the Larmor frequency is different for every spin in the solution. This causes the individual spins to precess at different Larmor frequencies, hence they start to dephase and the transverse magnetization decays. In fact, this is a very powerful way of relaxation. It can be shown, that this gives rise to a second

component in the relaxation, namely<sup>29</sup>

$$J(\omega_0) = \overline{B^2} \frac{2\tau_c}{1 + \omega_0^2 \tau_c^2} + \overline{B^2} \tau_c \quad (2.7)$$

In order to illustrate equation 2.6 and 2.7, they are plotted in Figure 2.3. The Larmor

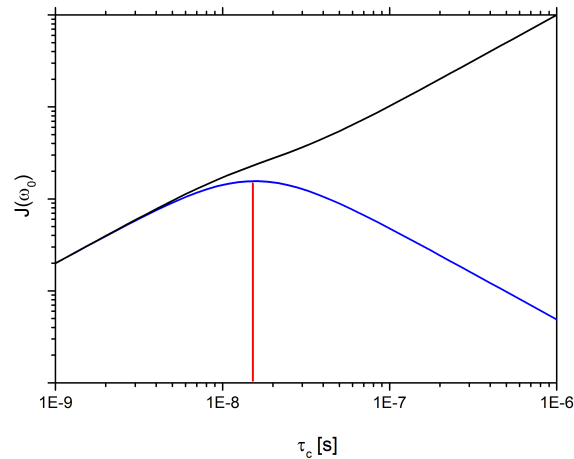


Figure 2.3: Spectral density function  $J(\omega_0)$  for different correlation times  $\tau_c$ , for the longitudinal relaxation (blue) and the transversal relaxation (black).

frequency was set to 64 MHz, which corresponds to the field strength of most clinical MRI scanners of 1.5 T. As one can see, there is a distinct maximum at a correlation time of around 15.6 ns, which corresponds to  $1/\tau_c = \omega_0 = 64$  MHz, like expected. However, the important consequence is that for longitudinal relaxation no general rule applies e.g. like longer correlation times result in higher relaxation rates. For every Larmor frequency, there is an optimal correlation time, it must not be too long nor too short. This is a crucial step in designing contrast agents. A second consequence is, that the maximum value of the spectral density function for longitudinal relaxation rate is given by  $\overline{B^2}$ . Eventually, that means that the maximum of the relaxation rate is given by the strength of the local magnetic fields  $B$ , which are given by the molecules in solution and that the highest relaxivity is centered at the correlation time, that corresponds to the Larmor frequency. In contrast, the transversal relaxation given by equation 2.7 has a second term, which in opposite to the first term has no maximum, but is steadily increasing with increasing correlation time  $\tau_c$ . This is the reason why  $R_2$  is at least equal, but in most cases bigger than  $R_1$ .

## 2.3 Relaxation mechanisms

So far, only the difference between  $R_1$  and  $R_2$  has been described but not the different physical sources of local fields. The dominant ones are dipolar and chemical shift anisotropy mechanisms. Apart from that, a very efficient relaxation by paramagnetic species exists, which will be discussed in the next subsection. The dipolar relaxation mechanism is induced by magnetic moments of adjacent spins, irregardless if they are from other molecules or from a neighboring spin within the same molecule. Since there is one spin generating the field and another spin experiencing it, this mechanism is called dipole-dipole interaction.<sup>29</sup> It falls off rapidly with  $\frac{1}{r^3}$ , where  $r$  is the vector connecting the two dipoles. The strength is proportional to the gyromagnetic ratio  $\gamma_I$  of a spin. A higher gyromagnetic ratio leads to a larger magnetic moment and hence to a stronger interaction. Another source is the chemical shift. That is electrons in a molecule give rise to a local field at the nucleus and therefore the spin under investigation. Again due to thermal motion, this local field permanently changes and can cause relaxation of the spins. In principle all relaxation mechanisms for  $T_1$  affect also  $T_2$ .

## 2.4 Relaxation induced by paramagnetic species

As already mentioned, another source of relaxation are paramagnetic species, which is the most important relaxation mechanism in this work. Paramagnetic relaxation comes from dipolar interactions. But this time it is not induced by an interplay between only nuclear spins but by the spins from unpaired electrons, affecting the investigated nuclear spins. As already noted in the previous section, the strength of the dipolar interaction is proportional to the gyromagnetic ratio. Due to the fact, that the gyromagnetic moment of an electron exceeds the one of a proton by the factor of 650, dipolar interaction with unpaired electrons is a very efficient way of relaxation.<sup>30</sup> Typically, one tries to avoid paramagnetic impurities for instance by  $O_2$  gas, that has unpaired electrons which again results in fast relaxation. However, in the case of MRI contrast agents, this is exactly what is tried to achieve in a controlled manner. To differentiate it from all other relaxation pathways  $R_i^{dia}$ , it will be

called paramagnetic relaxation. The total relaxation rate in a given solution is then

$$R_i^{tot} = R_i^{dia} + R_i^{para} \quad i \in \{1, 2\} \quad (2.8)$$

The paramagnetic relaxation is dependent on the concentration  $[c]$  of paramagnetic species,

$$R_i^{para} = r_i[c] \quad i \in \{1, 2\} \quad (2.9)$$

Here the so called relaxivity  $r_i$  is introduced. It is one of the most important parameters for contrast agents, since the paramagnetic relaxation rate and therefore the total relaxation rate is linear proportional to the relaxivity. The paramagnetic relaxation rate usually exceeds the diamagnetic rate by several order of magnitudes and is therefore a highly efficient way to locally alter the relaxation rate. Since this high relaxation rate provides a good contrast, paramagnetic species are often used as contrast agents. Depending on if a paramagnetic species mainly changes the  $T_1$  or the  $T_2$  time, the according complex is called  $T_1$  or  $T_2$  contrast agent. There are several comprehensive review articles on  $T_1$  contrast agents<sup>9, 13, 32</sup> and  $T_2$  contrast agents,<sup>10, 22, 33</sup> in which more details can be found. The most important aspects and differences between the two relaxation mechanism will be discussed in the result chapter.

## 2.5 Superparamagnetism

In fact most of the negative contrast agents are superparamagnetic, rather than paramagnetic. Superparamagnetism has been predicted by Frenkel *et al.*<sup>34</sup> and experimentally observed by Bean *et al.*<sup>35</sup> Ferromagnetica show typical hysteresis curves in external magnetic fields.<sup>36</sup> Once ferromagnets are magnetized, they keep their magnetization known as remanence, because of single magnetized Weiss domains. If a ferromagnet is heated above a certain temperature, i.e. the Curie temperature, it loses its remanence. The reason is that at this temperature the thermal energy is high enough to randomly reorient the before aligned electronic spins in the Weiss domains.<sup>36</sup> The spins are kept aligned by the anisotropy energy barrier

$$E_A = K \cdot V \quad (2.10)$$

with  $K$  being the anisotropy constant and  $V$  the volume, for example of a ferromagnetic particle.<sup>10,32</sup> It is now possible to give a relaxation rate for the magnetization<sup>10,32</sup>

$$\frac{1}{\tau} = \frac{1}{\tau_N} + \frac{1}{\tau_B} \quad (2.11)$$

with the Brownian relaxation

$$\tau_B = \frac{3V\eta}{k_B T} \quad (2.12)$$

and the Néel relaxation

$$\tau_N \propto e^{E_A/k_B T} \quad (2.13)$$

where all parameters have their usual meaning. One should note, that  $\tau$  in this case refers to the relaxation of the electronic moment and not to the nuclear spin relaxation. If the particle gets smaller, the energy barrier decrease as well. Below a size of typically some tenths of nanometers, the spins reorient all the time. That leads to paramagnetic behavior of formerly ferromagnetic materials. Thus, the term superparamagnetism is somewhat misleading since in fact the underlying materials are ferromagnetic. Superparamagnets usually have a very high permeability  $\mu_r$  due to their ferromagnetic nature. Considering that the magnetization  $M \propto \mu_r H$ , with  $H$  being the external magnetic field strength, superparamagnets are excellent negative contrast agents, as will be shown later.

## 2.6 MRI fundamentals

So far the discussion included only NMR spectroscopy. Contrast agents, however, are mainly used in magnetic resonance imaging (MRI). In MRI spatially encoded signals are generated, which eventually leads to the use in medicine. For the following explanation an NMR tube filled with water is assumed to be measured in an MRI scanner. If a field gradient  $G_x$  is applied along the x-axis like in Figure 2.4 the Larmor frequency will differ along the x-axis because of<sup>37</sup>

$$\omega_0(x) = \gamma_I(B_{0,x} + G_x x) \quad (2.14)$$

Now one can differentiate different spin positions along the x-axis. This is the so called

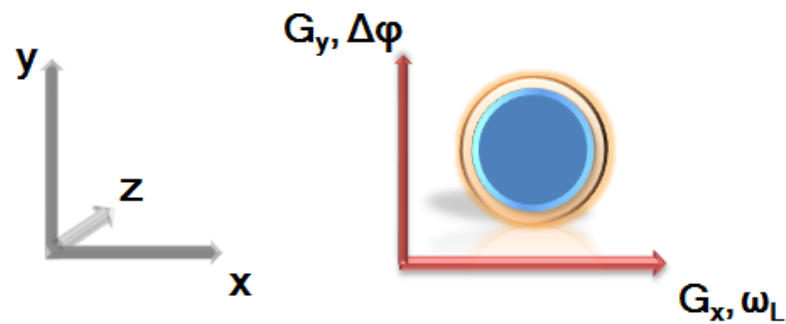


Figure 2.4: Tube filled with water in an MRI scanner with applied field gradient  $G_x$  in x-direction and  $G_y$  in y-direction respectively, which are colored red. The Larmor frequency  $\omega_L$  increases with increasing gradient strength in x direction. With increasing gradient strength in y direction increases the phase difference  $\Delta\varphi$ .

frequency encoding step. The signal  $S(t)$  coming from the sample along the x-axis then is<sup>38</sup>

$$S(t) = \int \rho(x) \cdot \exp(i\gamma_l G_x x t) dx \quad (2.15)$$

where  $\rho(x)$  denotes the spin density. A second gradient is applied in y direction to change the phase of the spins, hence it is also called phase encoding gradient.<sup>37</sup> Depending on the position of the spins in the sample, the gradient increases or decreases the local field. Therefore, some spin packages will precess slower than the Larmor frequency and others will precess faster. Thus they begin to dephase, analog to  $T_2$  relaxation, but in a controlled manner. If the gradient is switched off after a certain time the spins will have the same Larmor frequency again but different phases. This step is called phase encoding and is necessary to probe the second spatial dimension. The amplitude of the phase encoding gradient gets larger with every step. The reason for this is easier to explain in the so called k-space, see Figure 2.5. First one defines the reciprocal space vector

$$\mathbf{k} = \gamma_l \mathbf{G} t \quad (2.16)$$

where  $\mathbf{G}$  is the gradient in two dimensions and  $t$  the time. Assuming that the spin density at a certain place is  $\rho(\mathbf{r})$ , the two dimensional form of equation 2.15 is

$$S(\mathbf{k}) = \int \rho(\mathbf{r}) \cdot \exp(i\mathbf{k}\mathbf{r}) d\mathbf{r}. \quad (2.17)$$

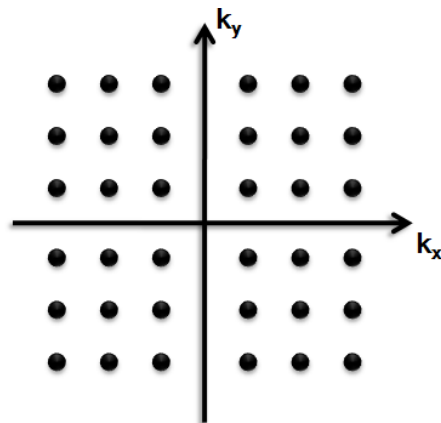


Figure 2.5: Depiction of k-space.

Thus the signal intensity in the k-space is related to the spin density in normal space with a Fourier transformation.

If the gradient  $G_y$  is not changing, the same line of  $k_x$  would be sampled in every step. If the amplitude of the gradient  $G_y$  increases in every step by  $\Delta G$ ,  $k_y$  increases to  $k_y = \gamma_l(G_y + \Delta G_y)t$ . This corresponds to the next line of  $k_y$  in k-space. To cover the whole k-space the  $G_y$  gradient needs to become stronger with every step.<sup>38</sup> Eventually a set of position encoded signals is collected, which can be reconstructed via Fourier transformation in order to obtain an image. So far the signal intensity only depends on the spin density and the location. In fact the signal intensity in MRI also depends on both the  $T_1$  and the  $T_2$  time,<sup>37</sup>

$$S(T_1, T_2, t_R, t_E) \equiv S(t) = S_0 \cdot \left(1 - e^{-t_R/T_1}\right) \cdot \left(e^{-t_E/T_2}\right) \quad (2.18)$$

where  $S_0$  is the signal intensity at zero time,  $t_R$  the repetition delay between different experiments, and  $t_E$  the echo time, which is the time between the excitation pulse and the signal detection during which the echo occurs. To illustrate equation 2.18 it is calculated and displayed in Figure 2.6. The shorter the  $T_1$  time and the longer the  $T_2$  time, the higher is the signal intensity. Correspondingly a high signal intensity for short  $T_1$  times can be reduced by a short  $T_2$  time. This is the reason why MRI resolve the anatomy of the body, because of different relaxation times in different body regions. This is where contrast agents come into play and their use in MRI, in order to change relaxation times in a controlled manner. Thus, even if in most cases the performance of a contrast agent is discussed on the basis of



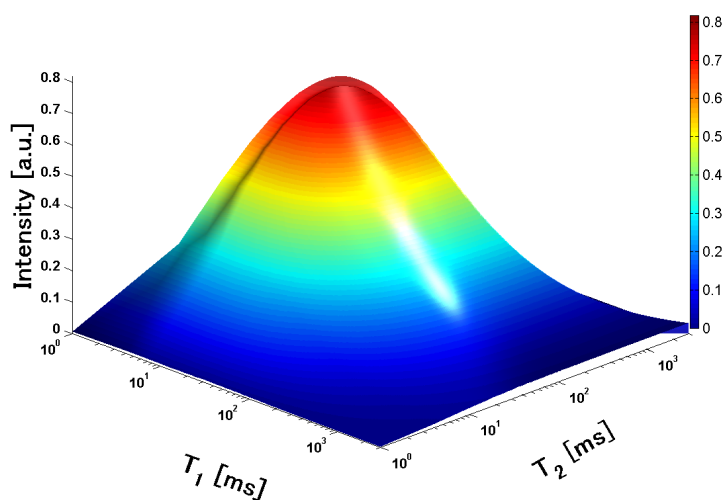


Figure 2.6: Signal intensity for different  $T_1$  and  $T_2$  times for a fixed repetition delay  $t_R$  of 300 ms and echo time  $t_E$  of 5 ms.

either its  $R_1$  or  $R_2$  rate, one should keep in mind that both rates are of importance. Still, it is uncommon to equivalently report both values. Moreover one should keep in mind, that the actual contrast also depends on the values chosen for  $t_R$  and  $t_E$ .

## 2.7 Comparison between positive and negative contrast agents

To get an impression how contrast agents are working, a so called  $T_1$  map (Left side of Figure 2.7) and a  $T_1$  weighted image (right side) of three Magnevist containing samples was recorded. A  $T_1$  map is simply an image, which graphically shows the  $T_1$  time of different regions, in this case of the three different sample tubes. Magnevist is a commercially available gadolinium based  $T_1$  contrast agent. The samples are numbered according to an increasing concentration of Magnevist. In a  $T_1$  weighted image the repetition delay between subsequent scans is chosen to be on the order or shorter than the average  $T_1$  time of the sample. Thus, the time to recover the magnetization is too short for regions which exhibit long  $T_1$  times. That leads to diminished signal intensities for samples with a long  $T_1$  time and high intensities for samples with a low  $T_1$  time.

Both images show samples with equal amounts of water, but different concentrations of

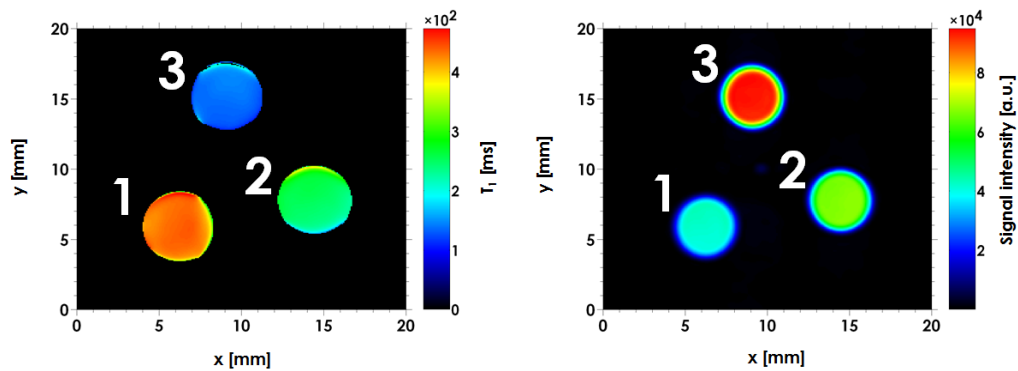


Figure 2.7:  $T_1$  map and  $T_1$  weighted image of Magnevist in 1 wt% Agarose. Samples are numbered in accordance to an increasing concentration of Magnevist. Repetition delay for the  $T_1$  weighted image was 150 ms and  $t_E$  1.6 ms.

Magnevist. The  $T_1$  time depends on the Magnevist concentration, with a decreasing  $T_1$  time for increasing concentrations. If for the same samples a  $T_1$  weighted image is recorded, the signal intensity is proportional to the concentration of Magnevist. The reason is an only partial recovery of the magnetization for samples with high  $T_1$  times. If the repetition delay is chosen short, the time for recovering the magnetization is too short for samples with a low concentration of Magnevist. That leads to a diminished signal intensity in this  $T_1$  weighted image. On the other hand, if the concentration is high a bright signal can be observed, although the repetition delay is short. This is why these kind of especially  $T_1$  reducing contrast agents are also called positive contrast agents.

The counterpart to a  $T_1$  weighted image is a so called  $T_2$  weighted image. Normally the echo time for MRI is chosen as short as possible, in order to obtain the maximum intensity, see also equation 2.18. In a  $T_2$  weighted image, a rather long echo time is chosen. Thus the intensity decreases for samples with short  $T_2$  times. To demonstrate this behavior, a  $T_2$  map (left side of Figure 2.8) and a  $T_2$  weighted image (right side) of magnetite containing nanocapsules (named NC-250 which will be introduced in the result chapter) were recorded. As one can see and in opposite to Magnevist containing samples, the intensity is diminished to almost zero for sample 3, which has the highest magnetite concentration. Therefore, it is possible to distinguish areas with high magnetite concentration from those with no magnetite. The vanishing signal intensity is the reason why these predominantly  $T_2$  reducing contrast agents

are also called negative contrast agents.

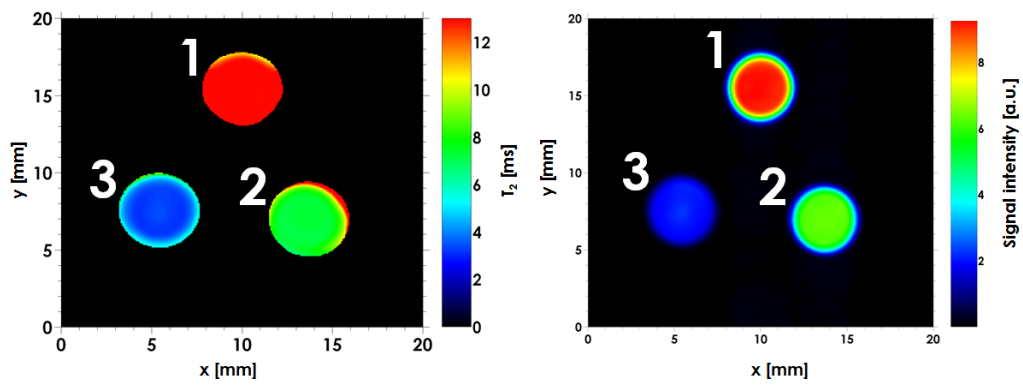


Figure 2.8:  $T_2$  map and  $T_2$  weighted image of magnetite containing samples. Samples are numbered in accordance to an decreasing amount of magnetite. Repetition delay for the  $T_2$  weighted image was 15 s and  $t_E$  4.6 ms.

---

## 3 Methods and materials

In this chapter the experimental setup as well as important measurement sequences will be introduced.

### 3.1 NMR scanner

Several magnets have been used for relaxation rate measurements and imaging. The first one, which has also been used for the *in vitro* MRI in the last chapter, was a 4.7 T horizontal, 20 cm-bore solenoidal magnet (Magnex Scientific Ltd., UK). It was equipped with a Maran DRX spectrometer from Oxford Instruments (Oxfordshire, UK) and a SGRAG 195/120/S 12 cm-bore gradient system from Magnex Scientific Ltd. (Oxford, UK) with a maximal field gradient strength of 2.0 T/m.

Due to a movement of the equipment from the MPI for Polymer Research to the physics department of the Johannes Gutenberg University (Mainz), the horizontal NMR scanner has been replaced by a vertical one (Bruker / Spektrospin, UK). The vertical magnet is equipped with the same Maran DRX spectrometer from Oxford Instruments (Oxfordshire, UK) as used before. The gradient system was a micro imaging system (Micro 2.5 Bruker, UK). Everything else was left unchanged. The used coils were a single resonant coil R1/20 40 MI 200 or a double resonant R1/13 20 MI 200 (m2m Imaging Corp., USA), both in birdcage geometry. For reasons, that will be shown later, the vertical 4.7 T scanner has been discharged to a field strength of 1.5 T later on. More details can be found in the result chapter 4. A single resonant coil originally designed for 300 MHz Xenon NMR has been modified to match the proton frequency of 64 MHz, corresponding to the Larmor frequency of protons at 1.5 T. For high field measurements a superconducting magnet operating at 300 MHz Larmor frequency equipped with a Tecmag console was used.

For temperature controlled experiments, samples were heated to 37 °C in a tempered water bath prior to measurements. Temperature control during measurement was achieved

in the NMR coil by application of a tempered stream of nitrogen gas using a home-built liquid nitrogen evaporator and a VT-1000 temperature controller from Bruker (Karlsruhe, Germany).

### 3.2 NMR relaxation rates

The longitudinal relaxation times  ${}^1\text{H}-T_1$  were measured with an inversion recovery sequence.<sup>29</sup> For the determination of one  $T_1$  time the spectra for 15 different relaxation delays were recorded. The resulting spectra were integrated and the data points fitted with a mono-exponential curve in order to determine the  $T_1$  time via

$$M(t) = M(t=0)e^{-t/T_1} + c \quad (3.1)$$

where  $t$  is the time between the RF pulse and the data acquisition,  $M(t)$  the magnetization at time  $t$  and  $c$  the noise. Whenever a multiexponential analysis was performed, the geometric mean (gm)  $T_1$  or  $T_2$  time was calculated, respectively.<sup>39</sup>

The transverse relaxation time  ${}^1\text{H}-T_2$  was measured with a Carr-Purcell-Maiboom-Gill (CPMG) echo train.<sup>40</sup> The echos were integrated and the resulting data points fitted with a mono-exponential curve in order to determine the  $T_2$  times. The equation is similar to equation 3.1 only with  $T_1$  now being  $T_2$ .

The transversal relaxivity can depend on the echo time of the CPMG sequence, as will be shown later (Equation 4.38 in chapter 2). To keep the influence of the sequence as small as possible, the shortest possible echo time was chosen. The measured data have been evaluated with a home written code in Matlab R2012a, see section 8.3.1.

In both cases, for the determination of the relaxivities  $r_1$  and  $r_2$ , a linear fit was applied

$$R_i = R_i^{dia} + r_i[c] \quad i \in \{1, 2\} \quad (3.2)$$

For some measurements water as well as 1 wt% agarose was used as sample matrix. Agarose is known to influence the relaxation rate, via chemical exchange between the hydroxyl protons on polymer side-chains and the protons of bulk water.<sup>41</sup> However this only affects the diamagnetic part of the total relaxation rate. Thus the total relaxation rate can change, without a change in relaxivity, see equation 3.2.<sup>42, 43</sup> Therefore it does not matter for relaxivity measurements if agarose or water is used as sample matrix.<sup>25</sup>

### 3.3 Diffusion measurements

For the determination of diffusion coefficients of water in nanocapsules, diffusion ordered NMR spectroscopy (DOSY-NMR) has been performed with help of Dr. Manfred Wagner (Max Planck Institute for Polymer Research). The NMR scanner was an Avance-III operating at 700 MHz from Bruker (Karlsruhe, Germany). The used probehead was a 5 mm  $^1\text{H}/\text{X}$  coil for heteronuclear detection. Here, the second nucleus was  $^{17}\text{O}$ . In addition the probehead possesses a z-gradient with maximum gradient strength of 0.4 T/m. The temperature was set to 298 K. The diffusion measurements were performed using a 2D DOSY sequence.<sup>44</sup> In order to increase the  $^{17}\text{O}$  signal intensity, an Insensitive Nuclei Enhanced by Polarization Transfer (INEPT) sequence with proton decoupling was used.<sup>29</sup> For one measurement the gradients were increased linearly in 16 steps. To calculate the diffusion coefficient, the Fourier transformed free induction decay (FID) were integrated and plotted against the according gradient strength. Then a mono-exponential decay was fitted to the data points

$$I(G) = I(0) \cdot \exp\left(\sqrt{2\pi\gamma_I G \delta} \cdot \frac{\Delta - \delta}{3}\right) \quad (3.3)$$

where  $G$  is the gradient strength,  $I(0)$  the intensity without applying a gradient,  $\delta$  is the duration for which the gradient is switched on, and  $\Delta$  is the diffusion time, hence the time between the two gradients.

### 3.4 MRI pulse sequence

In this work, a so called spin echo (SE) sequence have been used exclusively for MRI. In the SE sequence, the echo is induced by a  $180^\circ$  pulse after the phase encoding and first read gradient. The advantage of the SE sequence in comparison to a gradient echo sequence is that the signal only decays with  $T_2$  and not  $T_2^*$ , because field inhomogeneities are refocused by the  $180^\circ$  pulse.<sup>37</sup> Additionally the SE sequence is less sensitive to susceptibility artifacts.<sup>45</sup> The disadvantages are a longer scan time and more applied rf-power because of the additional  $180^\circ$  pulses. For the denotation of the parameters see also section 2.6 in chapter 2.

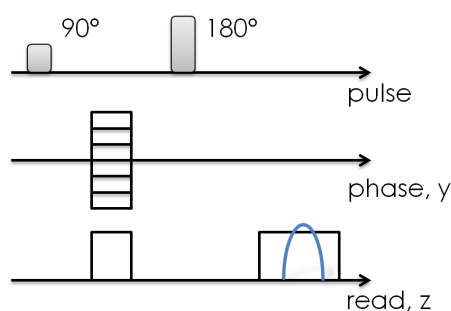


Figure 3.1: Sketch of the Spin echo sequence used in this work. The blue arc in the read out gradient depicts the echo.

### 3.5 Exchange measurements

In this thesis, it has turned out, that the water exchange from the bulk phase to the core of nanocapsules is very important for the efficiency as contrast agents. There are several NMR techniques, that are able to measure the water exchange between different phases, for example Diffusion Exchange Spectroscopy (DEXSY)<sup>46</sup> or Altered Relaxation Times Detect Exchange Correlation (ARTDECO).<sup>47</sup> The concept behind this kind of exchange sequences is the same, no matter if the diffusion (DEXSY) or  $T_2$ -time (ARTDECO) is recorded. In this work, ARTDECO has been used.<sup>48</sup> ARTDECO can differentiate between two environments in a solution exhibiting different  $T_2$  times, see also sketch 3.2. Bulk water has a certain  $T_2$  time, which will be named  $T_{2,2}$ . However, in the case of water in a nanocapsule, the water will experience different local fields than the bulk water and therefore has a different  $T_2$  time, which will be named  $T_{2,1}$ . The idea is, that at time zero, the  $T_2$  time of the sample will be measured resulting in two  $T_2$  times, one coming from the bulk, one stemming from the close environment of the capsule. After a so called exchange time  $\tau_n$ , the  $T_2$  time is measured again. For  $\tau_n = 0$ , there are  $a_{11}$  water molecules, with  $T_2$  times  $T_{2,1}$  and  $a_{22}$  water molecules with a  $T_2$  time of  $T_{2,2}$ . At time zero no exchange took place and  $a_{12}$  and  $a_{21}$  are simply zero. If the exchange time is  $\tau_n \neq 0$ ,  $a_{12}$  water molecules will diffuse from the capsule into the bulk phase and  $a_{21}$  molecules from the bulk phase into the capsule. Hence, these molecules experience different  $T_2$  times. The longer  $\tau_n$  is, the more water molecules will change their environments and the fewer will stay in their initial environment. In the experiment, the exchange time is increased stepwise and the amplitudes of the corresponding

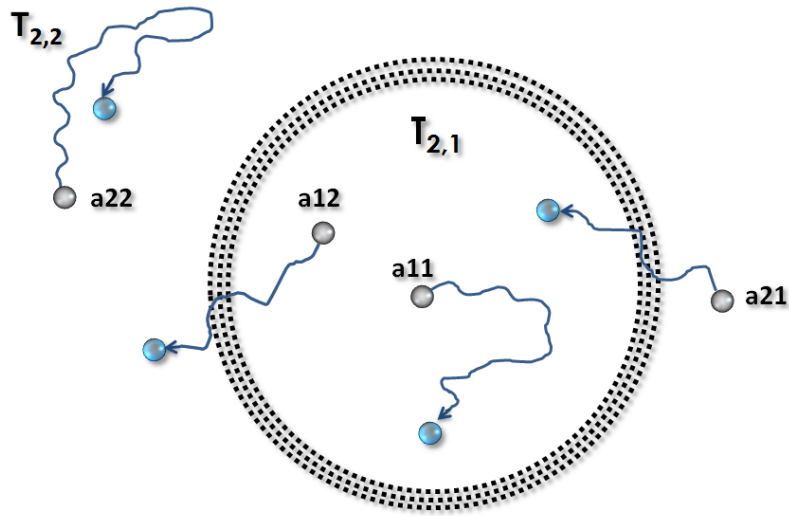


Figure 3.2: Sketch of a nanocapsule (black dashed lines) and water (blue spheres). The coefficient  $a_{mn}$ , where  $m, n \in \{1, 2\}$ , represents the number of water molecules in a certain environment. In total  $a_{22}$  water molecules diffuse in the bulk,  $a_{11}$  diffuse in the capsule,  $a_{12}$  exchange from the capsule to bulk and  $a_{21}$  exchange from bulk to the capsule.

signals will be compared. For short exchange times, there is a big amount of molecules, that does not change its environment, resulting in large  $a_{11}$  and  $a_{22}$  and small  $a_{12}$  and  $a_{21}$ . With increasing exchange time, more and more molecules will change their environment, hence  $a_{11}$  and  $a_{22}$  start to decrease, whereas  $a_{12}$  and  $a_{21}$  start to increase. By altering  $\tau_n$ , the exchange time for which molecules start to exchange from capsules to bulk and *vice versa* is measurable. To underline the physical meaning, it is helpful to look at the extreme situations. One is no exchange at all, for instance for a capsule that is impermeable to any molecule. The coefficients  $a_{11}$  and  $a_{22}$  would then just reflect the amount of water inside and outside the capsules, respectively. On the other hand, in case of very fast exchange, where a water molecule experiences all environments within the given exchange time, the individual  $T_2$  times and amplitudes lose their meaning. Instead an averaged  $T_2$  time and an averaged amplitude will be measured. The sequence is shown in Figure 3.3. The delay  $\tau$  is  $350 \mu\text{s}$ . The variable  $n$  is incremented logarithmically in order to avoid long measurement times. The resulting 2D data set had a size of 1024 times 128 and was fitted directly in the time domain with a two



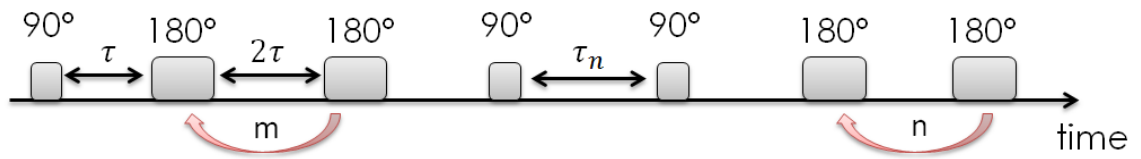


Figure 3.3: Sketch of the ARTDECO pulse sequence, not drawn to scale. The echo time  $t_E$  between two  $180^\circ$  pulses equals  $2\tau$ . The exchange time is  $\tau_n$ . In the first block  $m$  and in the second block  $n$  echos are acquired, respectively.

dimensional fit,

$$S(m, n) = a_{11} \cdot e^{-t_1/T_{2,1}} \cdot e^{-t_2/T_{2,1}} + a_{12} \cdot e^{-t_1/T_{2,1}} \cdot e^{-t_2/T_{2,2}} + a_{21} \cdot e^{-t_1/T_{2,2}} \cdot e^{-t_2/T_{2,1}} + a_{22} \cdot e^{-t_1/T_{2,2}} \cdot e^{-t_2/T_{2,2}} \quad (3.4)$$

where  $S(m, n)$  is the signal intensity, the parameters  $a_{mn}$ ,  $T_{2,1}$  and  $T_{2,2}$  have their meaning like defined above.

### 3.6 NMR Dispersion

As shown in section 2.1, the relaxivity depends on the Larmor frequency. In fast field cycling (FFC) measurements the  $T_1$  time for different magnetic field strengths is accessible, resulting in the relaxation rates for different Larmor frequencies, also known as NMR dispersion (NMRD) profiles.<sup>49,50</sup> Fitting of an appropriate model can give access to different correlation times.<sup>51</sup> The FFC measurements have been performed by Dr. Oliver Neudert (Max Planck Institute for Polymer Research) at the Ilmenau University of Technology on a Fast Field Cycling (FFC) relaxometer (Spinmaster FFC2000, Stelar s.r.l., Pavia, Italy) for magnetic field strengths in the range of 0.23 mT to 0.54 T.

---

## 4 Results and Discussion

In this chapter, the  $T_1$  and  $T_2$  contrast agents will be characterized. It consists of two parts. The first section deals with positive  $T_1$  contrast agents. The second section shows the results on negative  $T_2$  contrast agents.

### 4.1 Positive contrast agents<sup>#</sup>

This section starts with a more detailed theoretical approach describing gadolinium containing contrast agents. Subsequently the relaxation rate for Gadovist at different magnetic fields, temperatures and in different polymer solutions is investigated and simulated. Having established a general understanding of relaxivity, section 4.1.5 deals with the exchange of water molecules and protons in general in and out of nanocapsules. Thereafter, different nanocapsule systems are introduced and discussed as high relaxivity contrast agents. In the end, *in vivo* experiments demonstrate the value of the investigated systems as contrast agents.

#### 4.1.1 Theory of longitudinal relaxivity

Before describing nanocapsules as  $T_1$  contrast agents, it is helpful to look at the relaxivity of different solutions and to establish the theoretical concept behind  $r_1$ . One should keep in mind, that the relaxation rate is proportional to the relaxivity. The longitudinal relaxivity  $r_1$  usually consists of an inner and outer sphere contribution

$$r_1 = \frac{1}{T_1} = \frac{1}{T_1^{IS}} + \frac{1}{T_1^{OS}} \quad (4.1)$$

---

<sup>#</sup>This section is based on the publication "Increasing relaxivity of magnetic resonance contrast agents induced by confinement in semipermeable nanocapsules" by Kerstin Malzahn<sup>‡</sup>, Sandro Ebert<sup>‡</sup>, Isabel Schlegel, Oliver Neudert, Gunnar Schütz, Andreas Ide, Farnoosh Roohi, Daniel Crespy, Kerstin Münnemann, Katharina Landfester, currently under review at "Advanced Healthcare Materials".<sup>‡</sup>: Authors contributed equally.

with IS and OS denoting the inner and outer sphere, respectively. The inner sphere contribution arises from molecules temporarily bound to a paramagnetic center of a molecule and the dipole-dipole interaction between the ion and the hydrogen of a molecule.<sup>52</sup> This kind of interaction has been described by Solomon, Bloembergen, and Morgan and is consequently called SBM theory.<sup>53–55</sup> In most  $T_1$  contrast agents the paramagnetic center is a gadolinium

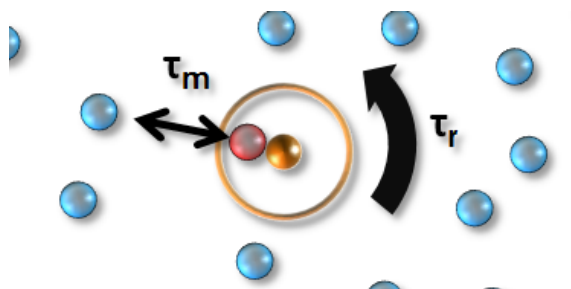


Figure 4.1: Inner sphere relaxation by water molecules temporarily binding to an ionic center (Orange sphere inside orange circle). The correlation time describing the water molecule binding is the water exchange time  $\tau_m$ .

ion ( $Gd^{3+}$ ) which is incorporated in a chelate complex, because of its toxicity.<sup>9,56</sup> Often only the hydrogen atoms of water are regarded as the relaxing molecule. However, every hydrogen atom of any solvent molecule can be relaxed, as also stated by Bloembergen and Morgan.<sup>9,32,55</sup> However, because the gadolinium ion is bound to a chelate complex, only small molecules can approach close enough to interact with the electron. In addition, the partially negatively charged oxygen of water can temporarily bind to the positively charged gadolinium ion. Therefore, water is considered as the most important molecule to be relaxed, strictly spoken the hydrogen atoms of it. After a characteristic water exchange time  $\tau_m$ , a water molecule from the inner sphere exchanges with a water molecule from the outer sphere which is not yet relaxed. Due to this reason a fast water exchange is favorable up to a certain limit, because more protons can be relaxed. However, the water exchange must not be too fast, to ensure effective relaxation. This allows the propagation of the relaxing effect to the entire solvent.<sup>56</sup> Due to this exchange the inner sphere contribution is sometimes called chemical exchange model.<sup>56</sup>

The inner sphere relaxivity is given by<sup>57</sup>

$$\frac{1}{T_1^{IS}} = \rho_m q \frac{1}{T_{1,m} + \tau_m} \quad (4.2)$$

In equations 4.2  $p_m$  refers to the mole fraction of metal ion,  $q$  to the number of bound water molecules per metal ion,  $\tau_m$  the residence time of the water molecule at the metal ion, and  $T_{1,m}$  the  $T_1$  time of the solvent molecule in the inner sphere, respectively. The latter must not be confused with the total  $T_1$  time of the system.

The  $T_1$  time of the solvent molecule in the inner sphere consists of two parts,

$$\frac{1}{T_{1,m}} = \frac{1}{T_1^S} + \frac{1}{T_1^D} \quad (4.3)$$

with  $T_1^S$  and  $T_1^D$  denoting the scalar and dipolar term, respectively. The scalar term stems from the hyperfine interaction between the electrons of the  $\text{Gd}^{3+}$  and the nuclear spins of the water protons and the dipolar term from electron nuclear spin coupling. Before making the next steps, it is convenient to introduce a constant  $C$ , containing the physical constants of the system,

$$C = \frac{2}{15} \left( \frac{\mu_0}{4\pi} \right)^2 \frac{\gamma_I^2 g^2 \mu_B^2 S(S+1)}{r^6} \quad (4.4)$$

with  $\mu_0$  being the permeability of vacuum,  $\gamma_I$  the nuclear gyromagnetic ratio,  $r$  the distance between the metal ion and the proton,  $\omega_I$  and  $\omega_S$  the proton and electron Larmor frequencies, respectively. One should note that the theory was derived in the early 50ies of the last century. At that time the Système international d'unités (SI) system was not yet established. Therefore, the constant  $C$  is often given in Gaussian Centimetre Gram Second (CGS) units.<sup>54</sup> For the CGS system the relation  $\mathbf{B}_{CGS} = \sqrt{4\pi/\mu_0} \mathbf{B}_{SI}$  holds true, where  $\mathbf{B}_{CGS,SI}$  denotes the magnetic flux density in the Gauss CGS and the SI system, respectively.<sup>54,56</sup>

The dipolar term for  $T_1$  can then be written as

$$\frac{1}{T_1^D} = C \left[ \frac{3\tau_{c,1}}{1 + \omega_I^2 \tau_{c,1}^2} + \frac{7\tau_{c,2}}{1 + \omega_S^2 \tau_{c,2}^2} \right] \quad (4.5)$$

and the scalar term as

$$\frac{1}{T_1^S} = \frac{2}{3} S(S+1) \left( \frac{A}{\hbar} \right)^2 \left[ \frac{\tau_{e,2}}{1 + \omega_S^2 \tau_{e,2}^2} \right] \quad (4.6)$$

At this point, one should note the analogy of the equations above to the equations given in section 2.2. There it was shown, that the relaxation rate is proportional to the strength of the local magnetic field and the spectral density function. In equation 4.5 the strength of the local field is given by  $C$ , which is basically determined by the gadolinium complex, whereas the

the spectral density function is given by the other terms of the equation. If the parameters are known, the relaxivity and therefore relaxation rate in solution can be calculated. This will be done in the next section. The correlation times are defined by

$$\frac{1}{\tau_{c,i}} = \frac{1}{T_{i,e}} + \frac{1}{\tau_m} + \frac{1}{\tau_r} \quad i \in \{1, 2\} \quad (4.7)$$

and

$$\frac{1}{\tau_{e,i}} = \frac{1}{T_{i,e}} + \frac{1}{\tau_m} \quad i \in \{1, 2\} \quad (4.8)$$

$T_{1,e}$  and  $T_{2,e}$  are the electron longitudinal and transversal relaxation times of the metal ion,  $\tau_m$  the residence time of the water molecule at the Gd ion, and  $\tau_r$  the rotational correlation time. For the interpretation of the results, it is important to note, that the electronic relaxation times are increasing quadratically with magnetic field.<sup>52</sup> For spherical molecules  $\tau_r$  can be expressed as<sup>32</sup>

$$\tau_r = \frac{4\pi r^3 \eta}{3k_B T} \quad (4.9)$$

with  $\eta$  being the viscosity, and  $r$  the radius of the molecule.

The equations are similar for  $T_2$ , namely the dipolar term

$$\frac{1}{T_2^D} = \frac{1}{2} C \left[ \frac{3\tau_{c,1}}{1 + \omega_I^2 \tau_{c,1}^2} + \frac{13\tau_{c,2}}{1 + \omega_S^2 \tau_{c,2}^2} + 4\tau_{c,1} \right] \quad (4.10)$$

and the scalar one

$$\frac{1}{T_2^S} = \frac{1}{3} S(S+1) \left( \frac{A}{\hbar} \right)^2 \left[ \frac{\tau_{e,2}}{1 + \omega_S^2 \tau_{e,2}^2} + \tau_{e,1} \right] \quad (4.11)$$

The scalar contribution is usually not very efficient in comparison to the dipolar relaxation. Because of the temporarily binding of the water molecule to the paramagnetic center the proton is two bonds separated from the gadolinium ion. This makes the hyperfine coupling constant  $\frac{A}{\hbar}$  from the electronic spin of the gadolinium ion to the nuclear spin of the proton relatively small.<sup>9</sup> In addition, it is dependent on  $\omega_S$  and therefore decreases rapidly already at low fields.

In a second step, the outer sphere contribution is introduced. Outer sphere relaxation has been described by Ayant *et al.* and later by Freed, who took into account the volume excluded by the paramagnetic center.<sup>58,59</sup> The outer sphere part stems from water molecules passing

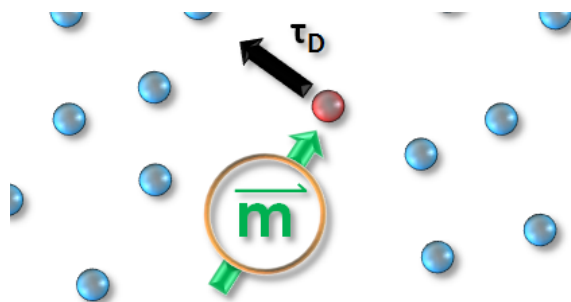


Figure 4.2: Outer sphere relaxation stems from water molecules passing the magnetic moment  $m$  of a paramagnetic center.

the magnetic moment of the paramagnetic complex. The determining correlation time for outer sphere relaxation is the diffusional correlation time  $\tau_D$  and is given by

$$\tau_D = \frac{d^2}{D} \quad (4.12)$$

where  $d$  denotes the distance of closest approach between the solvent molecule and the complex and  $D$  the relative diffusion coefficient between the paramagnetic complex and the solvent molecule.<sup>59</sup> The relative diffusion is given by

$$D = D_p + D_s \quad (4.13)$$

where  $D_p$  and  $D_s$  stand for the diffusion coefficient of the paramagnetic complex and of the solvent molecule respectively. By this definition  $\tau_D$  is the time that a solvent molecule needs to diffuse a distance of  $\sqrt{2}d$ .<sup>60</sup> According to Freed, outer sphere relaxation is only governed by water diffusing past the metal complex:

$$R_1^{OS} = \frac{6400\pi}{81} r^6 \frac{15}{2} C N_A \frac{[C]}{dD} [7j(\omega_S \tau_D) + 3j(\omega_I \tau_D)] \quad (4.14)$$

with

$$j(\omega, \tau_D) = \text{Re} \left[ \frac{1 + \frac{1}{4} \left( i\omega\tau_D + \frac{\tau_D}{T_{1,e}} \right)^{1/2}}{1 + \left( i\omega\tau_D + \frac{\tau_D}{T_{1,e}} \right)^{1/2} + \frac{4}{9} \left( i\omega\tau_D + \frac{\tau_D}{T_{1,e}} \right) + \frac{1}{9} \left( i\omega\tau_D + \frac{\tau_D}{T_{1,e}} \right)^{3/2}} \right] \quad (4.15)$$

In equation 4.14  $N_A$  denotes the Avogadro constant and in 4.15 Re stands for "the real part of" and  $\omega$  for  $\omega_S$  or  $\omega_I$ , respectively. All other parameters are denoted like above. The magnetic center is normally much bigger than the water molecule, due to its chelate complex

resulting in slow diffusion of the complex. Hence, the relative diffusion coefficient is replaced by the self diffusion coefficient of water, which is  $2.27 \cdot 10^{-9} \text{ m}^2/\text{s}$  at room temperature.<sup>61</sup> From the introduced formulas one can understand why mostly ions like  $\text{Gd}^{3+}$  are used. Because of seven unpaired electrons  $\text{Gd}^{3+}$  has a spin quantum number  $S$  of  $7/2$ . Since  $R_i \propto S^2$  is valid for all relaxation rates, a high spin quantum number  $S$  is very desirable. Since  $\omega_S \approx 650\omega_I$ , terms with  $\omega_S$  in the denominator decrease rapidly with increasing field.<sup>13,31</sup> Thus, terms with  $\omega_S$  can be neglected for magnetic fields higher than a few mT, like for example the complete scalar contribution given by equation 4.6, in addition to the reasons already mentioned.

Apart from the parameters introduced above, which are mostly given and hardly changeable, especially the rotational correlation time  $\tau_r$  has attracted a lot of interest.<sup>62,63</sup> This parameter can be altered by changing the environment of the metal ion, like encapsulation,<sup>17,64–66</sup> immobilizing on particle surfaces,<sup>67,68</sup> attaching different surfactants or grouping several ions together in a hyperbranched polymer,<sup>69,70</sup> just to name few.<sup>13,71</sup> The SBM theory for low molecular gadolinium-based contrast agents in water is able to properly describe the relaxation rates over a broad range of different magnetic fields.<sup>9</sup> With the above introduced equations, the relaxivity can now be simulated in a semi-empirical approach. For that, experimentally gained literature values are inserted in the above equations. Then the relaxivity can be simulated. Details can be found in section 7.1.1. In Figure 4.3 the influence of the rotational correlation time  $\tau_r$  on  $r_1$  is simulated. The lines show relaxivities for different water exchange times  $\tau_m$ . The black line corresponds to commercially available contrast agents like Magnevist or Gadobutrol. Their rotational time is around 50 ps. To see the influence of  $\tau_r$ , the simulation is performed with  $\tau_r = 125$  ps (blue line). One can see that the relaxivity has doubled in case of the slowly rotating agent.

#### 4.1.2 Relaxivity in solution

Commercially available and FDA approved contrast agents like Magnevist and Gadovist in solution have rather low relaxivities, between three and five  $\text{s}^{-1}\text{mM}^{-1}$ , depending on their local environment. The actual chelate complex in the Gadovist solution is called gadobutrol. For gadobutrol in water, the relaxivity  $r_1$  is  $2.8 \pm 0.1 \text{ s}^{-1}\text{mM}^{-1}$  in blood plasma the value

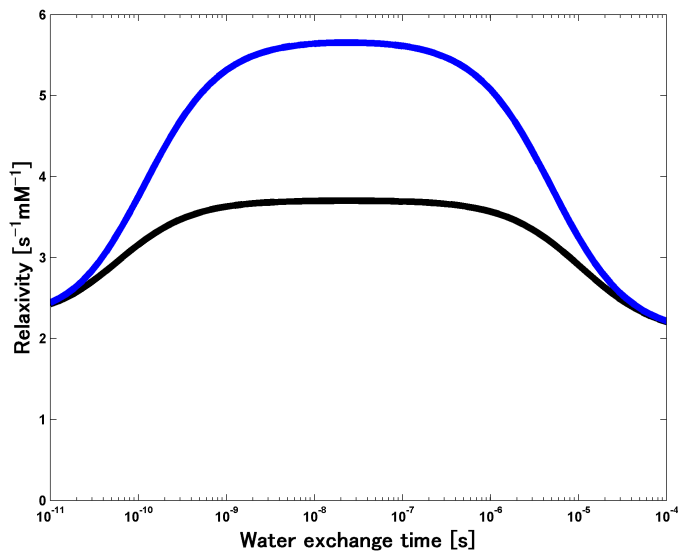


Figure 4.3: Relaxivity  $r_1$  for a rotational correlation time  $\tau_r$  of 54 ps (black line) and 125 ps (blue line).

is reported to be  $5.6 \text{ s}^{-1}\text{mM}^{-1}$ .<sup>72</sup> Different environments typically also have different viscosities. Since the rotational correlation time  $\tau_r$  and the diffusional correlation time  $\tau_D$  are proportional to the viscosity, that leads to different relaxivities. An easy way to change the viscosity is the introduction of sucrose into a solution of gadobutrol and water. It has already been shown that sucrose can mimic an *in vivo* environment.<sup>73</sup> On the left side of Figure 4.4  $R_1^{dia}$  is displayed as determined from the line fit via equation 3.2 (black circles). In addition,  $R_1^{dia}$  has been measured directly, so without gadobutrol, for different sucrose concentrations (blue circles), showing that both lead to the same results. Even more interestingly is the direct measurement of  $R_1^{dia}$  in  $\text{D}_2\text{O}$  (gray circles). Instead of water, the sucrose is dissolved by  $\text{D}_2\text{O}$ . If only water protons would be measurable, one would expect a difference in the results measured for sucrose in water. However, the results of  $R_1^{dia}$  obtained in water and  $R_1^{dia}$  obtained in  $\text{D}_2\text{O}$  led to comparable results. This is because the -OH groups of the sucrose can chemically exchange their protons with  $\text{D}_2\text{O}$ , leading to a situation, where water contains also protons, not just deuterium. This chemical proton exchange, in addition to the proton exchange via water diffusion, is very important for nanocapsules, as will be shown later. In addition to the measurements, semi-empirical simulations with a home-written



Matlab code were performed. Details of the calculations and its code can be found in the experimental section 7.1.1. First, measurements were performed at a magnetic field of 4.7 T and a temperature of around 7 °C. The calculations were performed for a magnetic field of 4.7 T and 10 °C. On the right side of Figure 4.4 the experimental results for  $r_1$ , as well as the simulated values for different sucrose concentrations are displayed. The higher the sucrose concentration, the higher the viscosity. As expected the relaxivities change, but in a

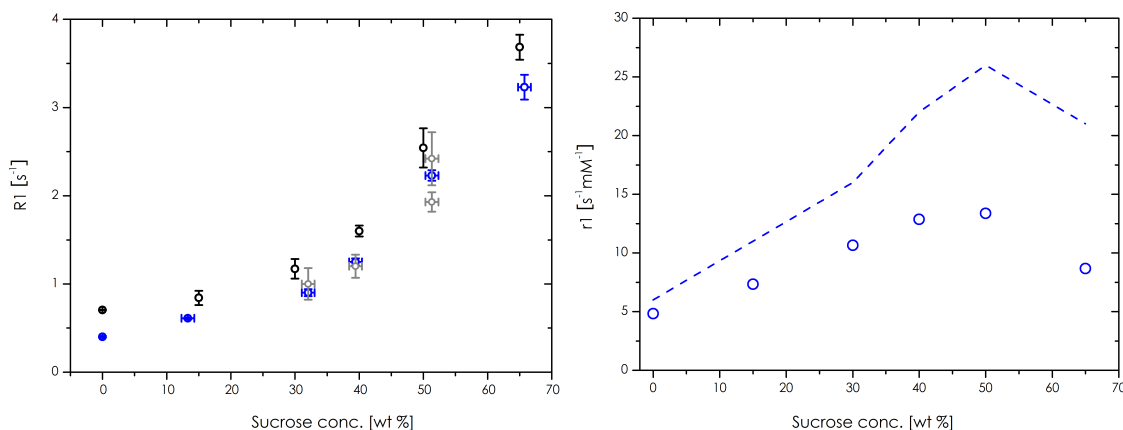


Figure 4.4: Left: Diamagnetic relaxation rate  $R_1^{dia}$  for the different sucrose concentrations as determined from the line fit (black), measured (blue) and measured in  $\text{D}_2\text{O}$  (gray). Right: Experimental relaxivity  $r_1$  (blue circles) and simulated relaxivity (blue dashed line) for gadobutrol in a solution of water and sucrose, for different sucrose concentrations.

non-trivial way. Whereas up to 40 wt% sucrose the relaxivity increases, for 65 wt% it drops to lower values. The simulation overestimates the experimental results by a factor of two. However, it is able to describe the bending of the curve, the most important feature at this point. To understand this behavior, it is helpful to look at the relaxivity of different water exchange rates and rotational correlation times. On the left side of Figure 4.5 the relaxivity for different values of the water exchange and the rotational correlation time is shown. On the right side, the projection into the plane is shown. Red areas and blue areas correspond to high and low relaxivities, respectively. In analogy to the island of stability for isotopes one might call it an isle of high relaxivity. For gadobutrol, the water exchange time is 176 ns.<sup>71</sup> It is also believed, that the water exchange is not influenced by changes in the environment.<sup>74</sup> And for  $\text{Mn}^{2+}$  solutions it has been shown, that even for sucrose concentrations as high as 78 wt% the environment stays aqueous.<sup>75</sup> Therefore one can assume that the

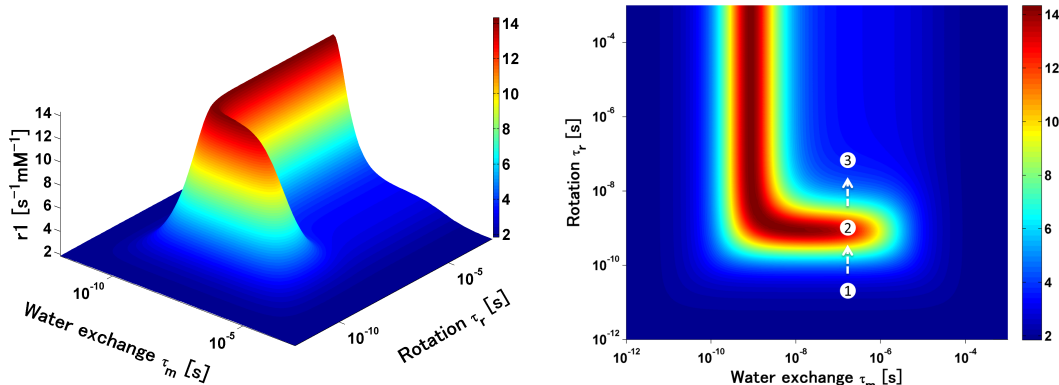


Figure 4.5: Simulated relaxivity for gadobutrol in water for different water exchange and rotational correlation times. Simulation is performed for 4.7 T and 283 K.

water exchange is unaffected by the presence of molecules other than water. The rotational correlation time has been determined to be 57 ps.<sup>71</sup> If one looks at Figure 4.5 and looks at the relaxivity for the water exchange of 176 ns and the rotational correlation time of around 56 ps (Step 1, indicated by number one in a white circle, on the right Figure), one gets a value of around three  $\text{s}^{-1}\text{mM}^{-1}$ , which is close to the measured value. If now, however, the sucrose concentration is increased, and by that the viscosity, the rotational correlation time is increased, whereas the water exchange rate stays the same (Step 2). The rotational correlation time is shifted to higher values, which up to a few nanoseconds is beneficial. If however the rotational correlation time is increased even further, the relaxivity starts to drop to lower values (Step 3). This is why of the beginning in Figure 4.4 the relaxivity increased, whereas for sucrose concentrations as high as 65 wt% the relaxivity dropped to a lower value. In addition to changing the viscosity, one can also change the temperature. Since

$$\tau_r \propto \frac{\eta(T)}{T} \quad (4.16)$$

and if one assumes an Arrhenius behavior of the viscosity, with

$$\eta(T) \propto e^{\frac{1}{RT}} \quad (4.17)$$

the rotational correlation time gets smaller for increasing temperatures. In Figure 4.6 the measured relaxivities for different sucrose solutions and different temperatures are displayed. As one can see, the relaxivity for the 50 wt% sucrose decreases for temperatures higher

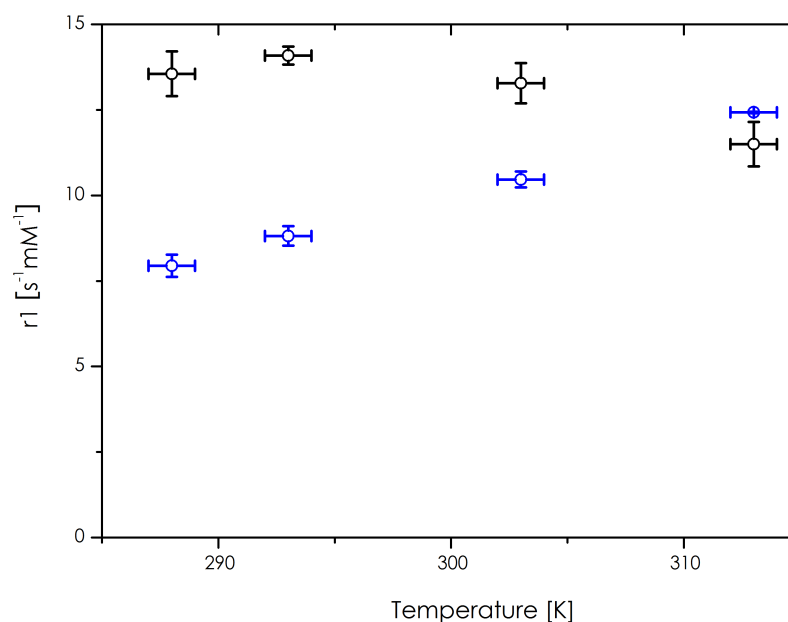


Figure 4.6: Measured relaxivity for Gadovist in sucrose solutions of 50 wt% (black) and 65 wt% (blue) for different temperatures.

than 293 K and for 65 wt% increases all the way up, until it is higher than for 50 wt%. Again the relaxivity is simulated, this time dependent on the temperature and an increasing sucrose concentration which is equivalent to an increasing viscosity. The result is shown in Figure 4.7. The simulation shows a good qualitative agreement with the experiment. If one looks at a temperature of 280 K, the relaxivity indeed first increases with increasing sucrose concentration and then starts to decrease again if the sucrose concentration is too high (As indicated by the white dashed arrow 1). This behavior was already observed in Figure 4.4. If one now looks at the sucrose concentration of 50 wt% (White arrow 2) and 65 wt% (White arrow 3), and goes from 280 K to 310 K, one can again see the experimentally observed behavior. For 50 wt% sucrose concentration the relaxivity decreases with increasing temperature, whereas for 65 wt% the relaxivity steadily increases. Hence, the simulation is able to describe the observed behavior qualitatively, even if the quantitative agreement is only modest. The simulations, therefore, are able to give valuable hints as to which are the limiting parameters. Because of the L-shape of the isle of high relaxivity, the rotational correlation time leading to a high relaxivity has an optimum value. Though all experiments so far have been performed at 4.7 T, the clinical standard field strength is still 1.5 T. Less than 20% of

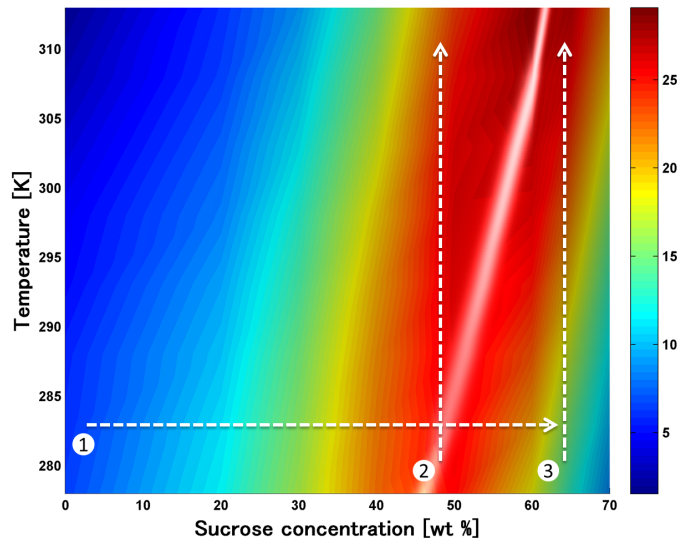


Figure 4.7: Relaxivity  $r_1$  for different temperatures and sucrose concentrations. Red areas correspond to high relaxivities, blue areas to low relaxivities. Arrows are guide to the eye, details are given in the text.

the MRI scanner works at 3 T and higher.<sup>76</sup> Based on this fact together with the findings described above, the magnetic field of the MRI scanner was changed from 4.7 T to 1.5 T. In addition to that and to satisfy the physiological conditions, the temperature is set to 310 K, if not mentioned other. Again the relaxivity is simulated for different water exchange and rotational correlation times in Figure 4.8. The major differences to the simulated relaxivity

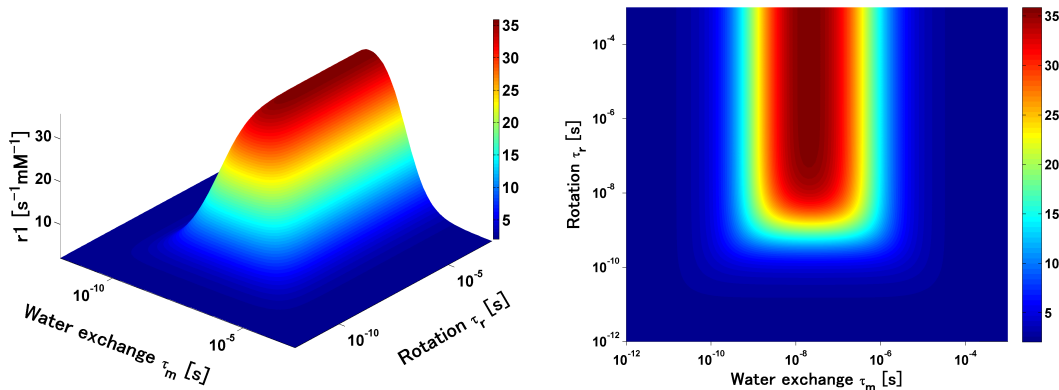


Figure 4.8: Simulated relaxivity  $r_1$  for different water exchange times  $\tau_m$  and rotational correlation times  $\tau_r$ , performed for 1.5 T and 310 K.

for 4.7 T are a higher total relaxivity and a very different shape of the isle of high relaxivity. For the water exchange of 176 ns, there is no optimum value for  $\tau_r$  anymore. An increasing  $\tau_r$ , leads in all cases to a high relaxivity, different to the situation at 4.7 T. Based on the simulations one would expect, that the relaxivity for 1.5 T increases with an increasing  $\tau_r$ . Again the relaxivity is measured for different sucrose concentrations, but this time at a field of 1.5 T and a temperature of 310 K. The experimental results together with the simulation are shown in Figure 4.9. Very different to the case at 4.7 T, the relaxivity is now increasing,

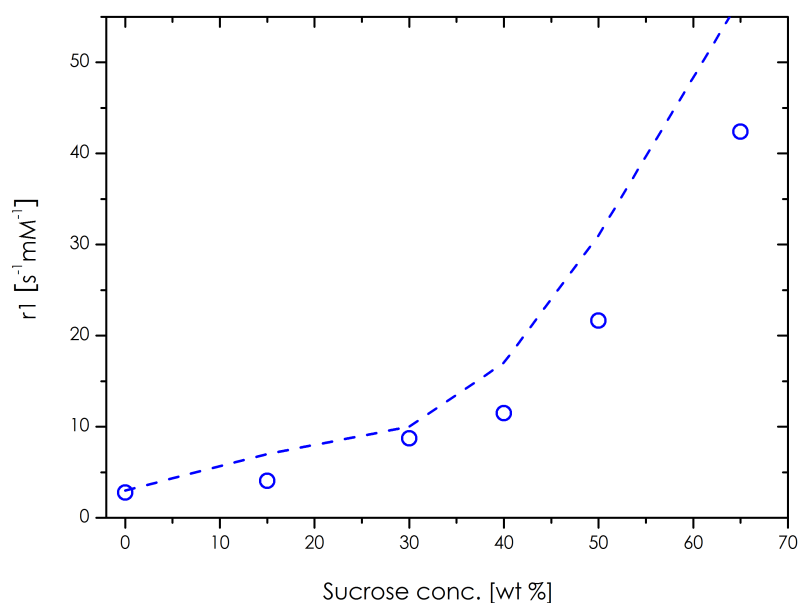


Figure 4.9: Measured relaxivity  $r_1$  for different sucrose concentrations at 1.5 T and 310 K (blue circles). The dashed blue line is the simulation, performed for 1.5 T and 313 K.

again like predicted by the simulation. It is hence possible, to tune the relaxivity in solution in a controlled fashion and the simulations are able to give good qualitative agreements.

Since it is possible to control the relaxivity via the viscosity one can think about additives other than sucrose. Therefore several different polymer solutions were tested, like poly(vinyl alcohol) (PVA), dextran (Dex), poly(ethylene glycol) (PEG) for different wt% and different molecular weights  $M_W$ . Details can be found in the experimental section 7.1.2. The results are displayed in Figure 4.10. As one can see, the relaxivity increases with the viscosity, but in addition is very dependent on the investigated polymer. Therefore, different polymer solutions with the same viscosities do not have the same relaxivities. Here, the concept

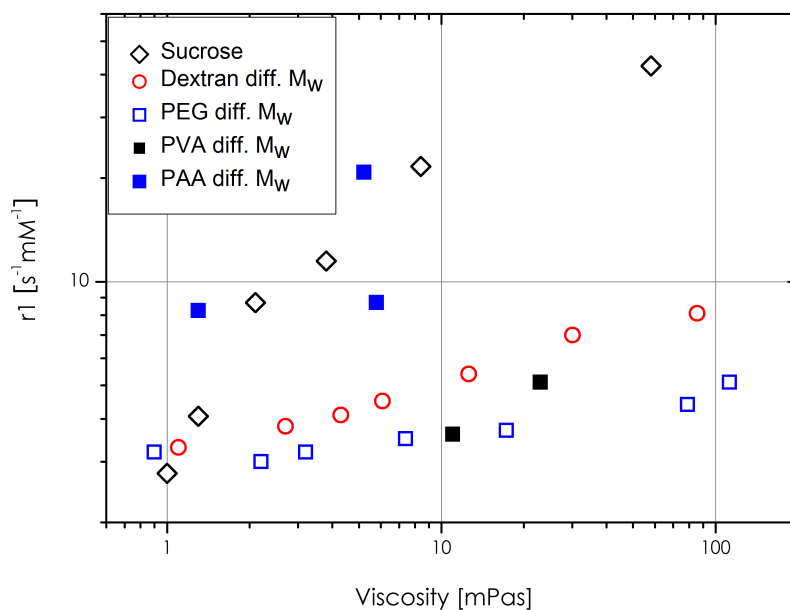


Figure 4.10: Relaxivities  $r_1$  for different polymer solutions of different wt% and different molecular weight  $M_W$  plotted against their measured viscosity.

of microviscosity comes into play. It is known, that the measured macroscopic viscosity in heterogeneous solutions must not coincide with the microviscosity experienced by water.<sup>9, 12</sup> It has been observed for proteins in solution with water and dextran, that the diffusion coefficient of the protein can become independent of the macroviscosity.<sup>77</sup> This means, that the local viscosity experienced by the protein is different to the measured viscosity, which eventually impacts the diffusion coefficient. This is especially true, if the the cosolvent is much larger than the investigated molecule. Therefore larger molecules like PEG or dextran lead to a microviscosity very different to the macroviscosity. To demonstrate the effect of the reduced viscosity, experimentally determined diffusion coefficients of water for the different solutions and the diffusion coefficient calculated with the macroviscosity are displayed in Figure 4.11. The experimentally determined diffusion coefficients are approximated from measured values found in literature, see also section 7.1.2. The diffusion coefficients correlate only weakly to the macroviscosity. The measured diffusion coefficients are much higher than predicted, because the microviscosities are not as high as one would expect based on the measured macroviscosities. To account for the reduced microviscosity, one can introduce a

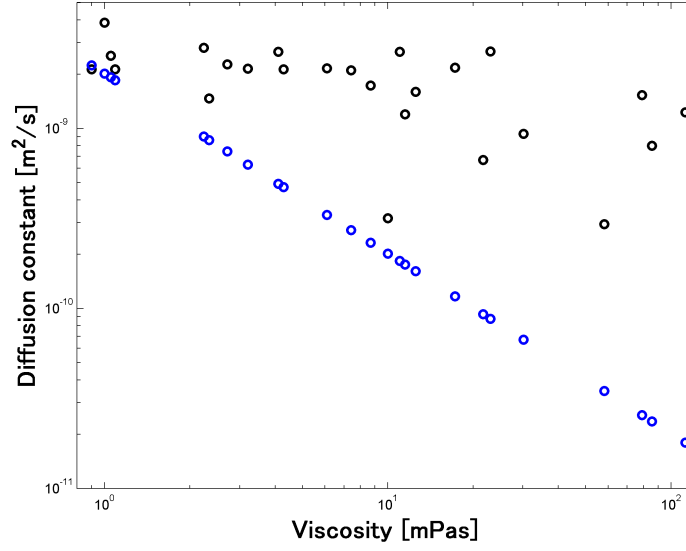


Figure 4.11: Diffusion coefficients of water, measured (black) and calculated (blue) for different macroviscosities.

scalar value  $s$  between 0 and 1 to the macroviscosity, like

$$\eta_{micro} = s \cdot \eta_{macro} \quad (4.18)$$

where  $\eta_{micro}$  denotes the microviscosity and  $\eta_{macro}$  the measured macroviscosity. The rotational correlation time is then,

$$\tau_r = \frac{4\pi r^3 \eta_{micro}}{3k_B T} \quad (4.19)$$

to account for the reduced viscosity experienced by water molecules. Of course the same is true for the diffusional correlation time

$$\tau_D = \frac{d^2}{D} = \frac{d^2 6\pi \eta_{micro} r}{k_B T} \quad (4.20)$$

A direct measure for the microviscosity is the diffusion coefficient, since  $D \propto 1/\eta$ . Since the diffusion coefficient in solution is measurable by NMR spectroscopy, one has a direct measure for the microviscosity. Therefore, one can use the measured diffusion coefficient and recalculate the microviscosity via

$$\eta_{micro} = \frac{k_B T}{6\pi D r} \quad (4.21)$$

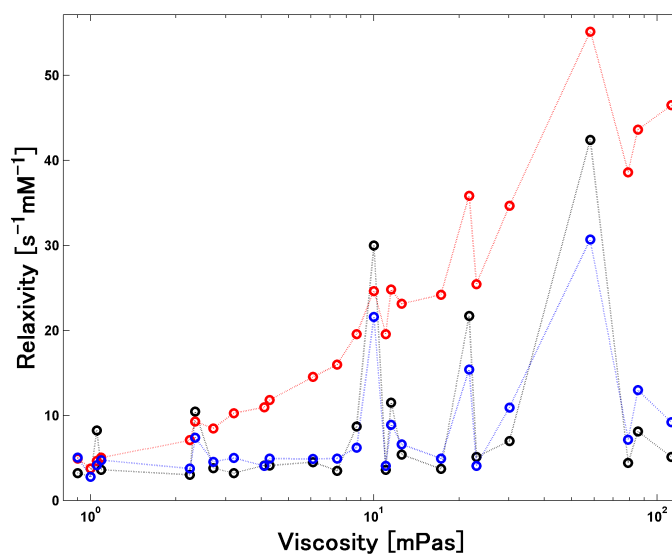


Figure 4.12: Measured relaxivity  $r_1$  (black),  $r_1$  simulated with  $\eta_{macro}$  (red), and  $r_1$  simulated with  $\eta_{micro}$  (blue) plotted against the different measured macroviscosities. The dashed lines are guides to the eye.

and perform a simulation with the calculated microviscosity. The result is shown in 4.12. The simulations performed with the help of the microviscosity fit much better to the experimental results than the simulations with the macroviscosity. This demonstrates, that indeed the calculation with the macroviscosity leads to an overestimation of the rotational and diffusional correlation time, leading to an overestimation of the relaxivity. And this is also the reason, why sucrose turns out to be the best relaxivity enhancer among the investigated cosolvents, since it is a smaller molecule, in comparison to PEG, Dex and so on.

### 4.1.3 High relaxivity in nanocapsules

Being able to adequately describe the relaxivity in solution, the focus of the next sections is the relaxivity of encapsulated gadobutrol. The influence of encapsulation on the relaxivity has been investigated for several polyurea nanocapsule systems. All of the following nanocapsule systems have been synthesized by Dr. Kerstin Malzahn, Max Planck Institute for Polymer Research, Mainz.<sup>78</sup> An overview is provided by Table 4.1. All systems are loaded with gadobutrol in different amounts. The polymer shell is composed of 1,6-diamino hexane



Table 4.1: Each column is: The used monomer, the gadobutrol concentration in the dispersed phase, the amount of monomer, the amount of TDI, the size determined by DLS, and the co-encapsulated substance, respectively.

Monomer	$c_{Gd}$ [mM]	$m_{Mon}$ [mg]	$m_{TDI}$ [mg]	Size [nm]	Load
DAH	10	116	262	$145 \pm 65$	-
DAH	100	116	262	$137 \pm 60$	-
DAB	10	88	262	$175 \pm 24$	-
DAB	100	88	262	$166 \pm 20$	-
DAE	10	60	262	$181 \pm 33$	-
DAB	10	88	262	$190 \pm 20$	sucrose

(DAH), 1,4-diamino butane (DAB) or 1,2-diamino ethylene (DAE) and 2,4-toluene diisocyanate (TDI). If not mentioned other, the ratio of the used diamine to TDI is always 1:1.5 and the initial concentration of gadobutrol in the dispersed phase is 10 mM. The concentration of gadolinium has been determined via Inductively Coupled Plasma Optical Emission Spectroscopy (ICP-OES). The nanocapsules are redispersed in water. The capsules will be named according to their used diamine. For example, capsules prepared from DAB in a ratio 1:1.5 TDI, with an initial concentration of gadolinium of 10 mM, will simply be named DAB-NC and so on. If anything is changing like the concentration or the ratio of monomer to TDI, it will be mentioned explicitly.

As mentioned, there are dozen of different attempts to tune the relaxivity to higher values than those of low molecular weight contrast agents. One approach is to encapsulate contrast agents, which then experience restricted diffusion.<sup>64, 66, 79</sup> However, only a few attempts have been made to theoretically describe this behavior.<sup>80</sup> Molecules which are confined in a closed environment will have a diffusion coefficient different to that in bulk, because of interactions with the confining system.<sup>81</sup> That effectively reduces the diffusion, which gives rise to a prolonged  $\tau_D$ , which again leads to high relaxation rates as already observed for relaxivity measurements in highly viscous solutions. This situation is sketched in Figure 4.13. An easy experiment to find out, if really the diffusion or rotation is restricted, is to measure

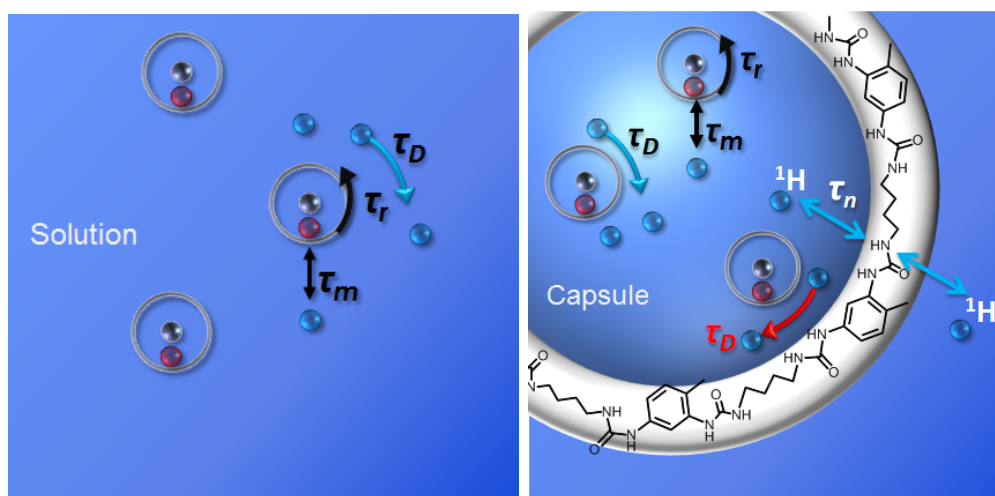


Figure 4.13: Left: Sketch of gadobutrol complexes in solution and the most important parameters,  $\tau_m$ ,  $\tau_r$  and  $\tau_D$ . Right: Sketch of gadobutrol complexes in a nanocapsule. The Diffusion changes because of interactions with the polymer shell, which slows down the diffusional correlation time  $\tau_D$  which is marked red. The proton exchange from the bulk to the inner of the capsule is referred to as  $\tau_n$ .

the relaxivities at high field, see Figure 4.14. The relaxivity is dramatically decreased at

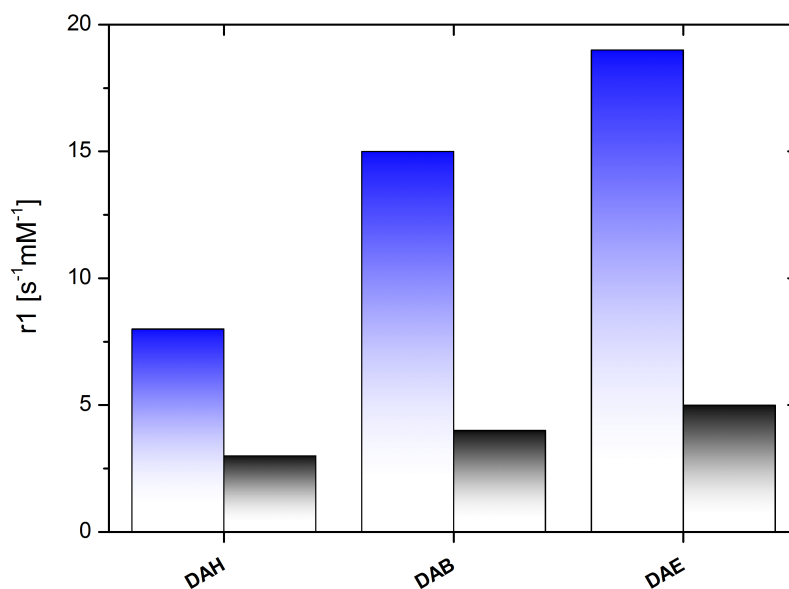


Figure 4.14: Relaxivities  $r_1$  for different capsule compositions at 64 MHz (blue) and 300 MHz (black).

high field. Since the gadobutrol complex is unchanged, one can easily consider the same

parameters to be important as in the case of gadobutrol which is not encapsulated. Apart from the parameters that are constant or are not influenced by the encapsulation process, the important parameters are the water exchange  $\tau_m$  from inner sphere to bulk, the electronic relaxation time  $T_{1,e}$ , the rotational correlation time  $\tau_r$  and the diffusional correlation time  $\tau_D$ . The water exchange is a field independent term and can therefore not be responsible for the decrease. The electronic relaxation time  $T_{1,e}$  is field dependent. This is a good point to recapture what actually determines the relaxivity in the end. Relaxivity is proportional to the spectral density function, e.g.

$$r_1 \propto \left[ \frac{3\tau_c}{1 + \omega_I^2 \tau_c^2} \right] \quad (4.22)$$

with

$$\frac{1}{\tau_c} = \frac{1}{T_{1,e}} + \frac{1}{\tau_m} + \frac{1}{\tau_r} \quad (4.23)$$

where the parameters have the meaning as defined in chapter 2. The overall correlation time  $\tau_c$  is dominated by whichever is the shortest time of  $T_{1,e}$ ,  $\tau_m$  or  $\tau_r$ . Like already mentioned the important thing here is that the spectral density function and hence relaxivity will increase with increasing  $\tau_c$  till the point where  $\omega_I^2 \tau_c^2$  is equal to one. As soon as  $\omega_I^2 \tau_c^2$  gets larger than one, the relaxivity starts to decrease again. Therefore it is beneficial to prolong the correlation time  $\tau_c$  but only up to a certain point. For gadobutrol in water  $\tau_r$  is on the order of some tenth of picoseconds, whereas  $T_{1,e}$  is in the area of some ns.<sup>52,56,71</sup> As  $T_{1,e}$  is increasing quadratically with the magnetic field strength, it is only important at low magnetic fields and becomes less important with increasing field strengths.<sup>52</sup> This results in  $\tau_r$  being the most important parameter to increase in case of the inner sphere relaxation. One can make similar considerations for the outer sphere relaxation rate, in which then  $\tau_D$  turns out to be the most important parameter. Eventually, only  $\tau_r$  and  $\tau_D$  are left over, which can give rise to such a large relaxivity, without any further gadobutrol complex modification. However, as the gadobutrol complex is not modified but just encapsulated, the rotational correlation should not differ too much. To support this argument,  $^{17}\text{O}$  measurements were performed. For low molecular weight contrast agents, like gadobutrol,  $^{17}\text{O}$  measurements can independently reveal most of the important parameters like the rotational correlation time.<sup>71</sup> It has been found, that for  $^{17}\text{O}$  the longitudinal relaxation is dominantly inner sphere in nature and that

Table 4.2:  $T_1$  times of  $^{17}\text{O}$  obtained for different temperatures.

$T$ [K]	$T_1^{H_2O^{17}}$ [ms]	$T_1^{DAH}$ [ms]	$T_1^{DAB}$ [ms]	$T_1^{DAE}$ [ms]
298	6.9	n.a.	6.7	n.a.
303	7.9	7.8	7.6	7.5
308	8.9	n.a.	8.5	n.a.
313	9.9	9.8	n.a.	9.2
318	11.2	n.a.	10.3	n.a.
323	12.2	11.7	11.3	11.2
333	14.7	14.1	13.7	13.2

the outer sphere contribution can be neglected.<sup>82</sup> If  $\tau_r$  is much shorter than  $\tau_m$  and  $T_{1,e}$ , the inner sphere relaxation rate will simply be proportional to  $\tau_r$ , e.g.  $R_1^{17\text{O}} \propto \tau_r$ .<sup>83</sup> A  $R_1^{17\text{O}}$  measurement has been performed at 700 MHz, for which the electronic relaxation time can be calculated to be 0.2  $\mu\text{s}$ . The water exchange is for gadobutrol already on the order of 0.15  $\mu\text{s}$  and even longer for encapsulated gadobutrol, as will be shown later. Hence, the condition  $\tau_r \ll T_{1,e}, \tau_m$  is easily fulfilled. Since  $\tau_r$  is a function of temperature, one can determine the rotational correlation time via a fit of the longitudinal relaxation rates acquired for different temperatures. However, in case of the capsules, no significant difference in  $T_1$  for neat  $\text{H}_2\text{O}^{17}$  and different capsule compositions has been found for different temperatures, see Table 4.2. In all cases, the change is less than 10%. That means, the inner sphere contribution is negligible, which in turn means that it is not the rotation which is diminished or at least not as much as would be necessary to explain the sixfold increase of relaxivities in nanocapsules. The same observation has been made for gadofullerenes, for which the  $T_1$  relaxation of  $^{17}\text{O}$  was found to be within a margin of 15% for the gadolinium loaded fullerenes in comparison to water. Since water cannot penetrate into the fullerene cage, there is no inner sphere contribution. Instead and like expected an outer sphere contribution was proposed to be the source of high relaxivity.<sup>16, 84</sup>

That leaves the diffusion which gives rise to a longer  $\tau_D$  and hence higher  $r_1$ . In order to further investigate the diffusion, DOSY measurements have been performed on DAB-NC

without gadobutrol. If the water exchange is slow enough, one would expect at least two contributions: One coming from the inside of the capsule, experiencing restricted diffusion and one coming from the bulk phase. To prevent that the result is influenced by proton exchange, the measurement was performed on  $^{17}\text{O}$  enriched  $\text{H}_2\text{O}^{17}$ . The result is shown in Figure 4.15. Again, there is no observable second component. With a mono-exponential

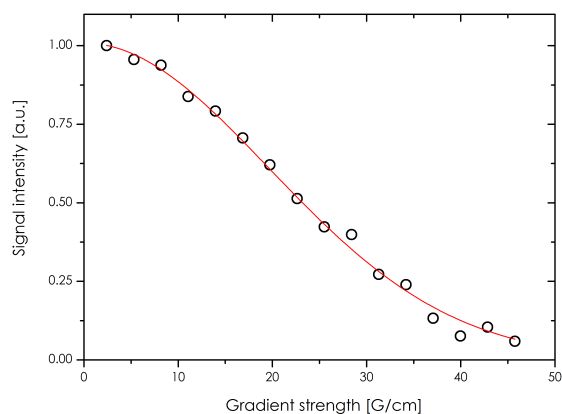


Figure 4.15: DOSY measurement on DAB-NC in  $\text{H}_2\text{O}^{17}$ . Red line is the fit with equation 3.3.

fit the curve is well described. Since the diffusion time in the sequence is on the order of some ms, the fast exchange makes it impossible to measure two separated diffusion coefficients. Instead, the water molecules experience different kind of environments within the given diffusion time, which gives rise to an averaged diffusion coefficient. To get a direct experimental proof that indeed the diffusion is restricted, NMRD measurements on DAB-NC without gadobutrol have been performed (Figure 4.16) by Dr. Oliver Neudert at the University of Ilmenau. Interestingly the relaxation rate decreases rather slowly. For freely and isotropically diffusing water, one would expect a  $\omega^{-2}$  dependency. However, in this case, a power function with  $R_1 \propto \omega^{-\chi}$  could be fitted, where  $\chi \approx 0.46$ . This behavior could fit with a relaxation model called Reorientation Mediated by Translational Displacements (RMTD).<sup>85</sup> It was found, that in this case  $\chi$  is  $0.50 \pm 0.04$ , which matches within the error with the value found here. The key point in this model is, that the molecules under investigation, e.g. water, are not freely diffusing anymore, but temporarily bind to a solid matrix. The solid matrix here would be the polymer shell of the capsule. Though it is not entirely clear, if really the RMTD mechanism is responsible for the altered relaxation behavior, the water dynamics in the nanocapsules are definitely slowed down in comparison to water in the bulk

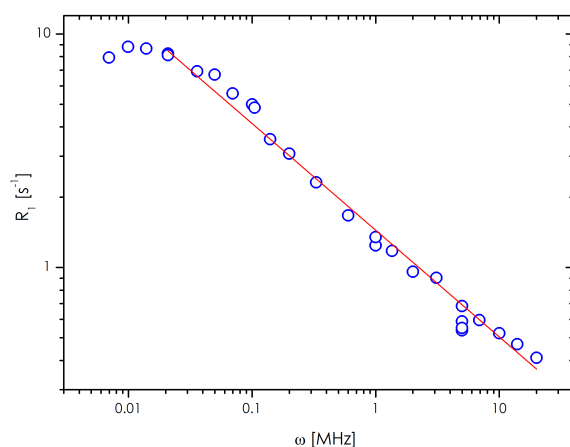


Figure 4.16:  $^1\text{H}$  relaxation rate for different Larmor frequencies for DAB-NC.

phase. Eventually for the NCs this gives rise to a strong outer sphere effect and therefore to the increased relaxivity.

Thinking about medical applications, one should keep in mind, that in fact the total relaxation rate is more interesting than just the relaxivity. Since the total relaxation rate is proportional to the relaxivity in product with the gadolinium concentration, a low relaxivity can be counterbalanced by a high concentration and *vice versa*. Therefore, the influence of the gadolinium loading on the relaxivity is investigated. For that, different capsules have been synthesized, with an initial concentration of gadobutrol in the dispersed phase of 10 mM and 100 mM, respectively. The investigated systems are DAH-NC and DAB-NC. The relaxivities are shown on the left side of Figure 4.17. The first thing one notices is the dramatically increased relaxivity, depending on the monomer used in comparison to neat gadobutrol in water. This relaxivity increase will be discussed below. Furthermore the relaxivity decreases for increasing gadobutrol loading in the capsules. This behavior has already been observed in literature.<sup>68,86</sup> To further elucidate the origin of this observation, one can measure the relaxivity for high concentrations in solution, see right side of Figure 4.17.

As one can see, even for concentrations as high as 100 mM, the highest concentration used for gadobutrol in the dispersed phase, there is almost no deviation from the linear behavior known for low concentrations. This shows that the drop in relaxivity is not an intrinsic effect for high concentrations of gadobutrol, but rather a special characteristic of nanocapsules. Figure 4.18 shows the difference between the two different situations of nanocapsules with

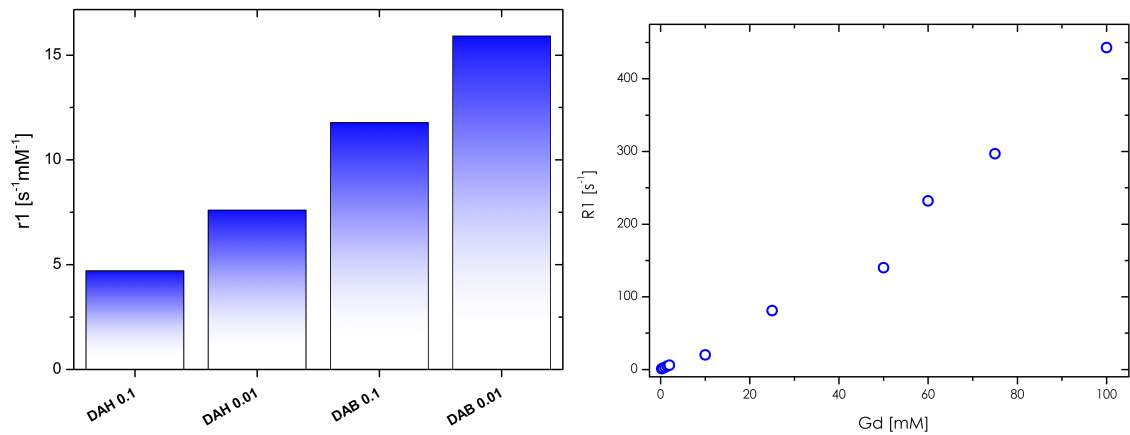


Figure 4.17: Left: Relaxivity  $r_1$  for different compositions of the nanocapsule system. DAH and DAB stand for the investigated systems DAH-NC and DAB-NC, respectively. The number stands for the gadobutrol concentration in the dispersed phase in Mol. Right: Relaxation rate  $R_1$  of gadobutrol in water for high concentrations.

a low and high loading of gadobutrol, respectively. In Figure 4.18 a.) the capsule has a

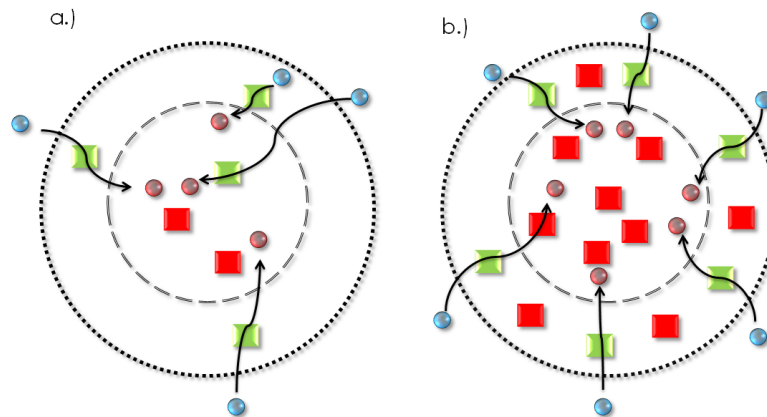


Figure 4.18: Sketch of capsules (black dashed circle) loaded with gadobutrol (green and red squares). Green squares correspond to active gadobutrol complexes, red squares to inactive gadobutrol complexes. Blue circles indicate water, red circles stand for water which is already relaxed. The gray dashed circle in the middle is to ease the visualization. The case of low loading correspond to situation a.), the capsule with high loading to situation b.).

low loading of gadobutrol. Water protons, that exchange through the polymer shell of the capsule are effectively relaxed by gadobutrol complexes at the surface. These complexes will

for now be called active complexes. Some gadobutrol complexes however, will only "see" water molecules which have been already relaxed (red circles). Therefore, these gadobutrol complexes are not contributing to the relaxivity, since they do not relax any water which has not been relaxed before. They will be referred to as inactive complexes. In case of the situation in Figure 4.18 b.) the loading of gadobutrol is increased in comparison to Figure 4.18 a.). In this situation, even more gadobutrol complexes are inactive. The situation is even worse for the capsules, since the relaxivity is increased. This means, the gadobutrol complexes at the inner surface of the capsule will relax incoming water molecules very effectively. This in turn decreases the chance for gadobutrol complexes in the inner part of the capsule to get in contact with water which has not been relaxed. From the point of view of the relaxation rate, these complexes do not exist, hence the conventional formula  $R_1 = R_1^{dia} + r_1 \cdot [c]$  would actually be written as

$$R_1 = R_1^{dia} + r_1 \cdot ([c_{act}^i] + [c_{inact}^i]) \quad i \in \{10 \text{ mM}, 100 \text{ mM}\} \quad (4.24)$$

$[c_{act}^i]$  is the concentration of active gadobutrol complexes,  $[c_{inact}^i]$  is the concentration of inactive complexes for 10 mM and 100 mM respectively. Since only the active gadobutrol complexes contributing to the relaxivity, the measured relaxation rate will be

$$R_1 = R_1^{dia} + r_1 \cdot [c_{act}] \quad (4.25)$$

which is equal to

$$R_1 = R_1^{dia} + r_1 \cdot ([c] - [c_{inact}^i]) \quad i \in \{10 \text{ mM}, 100 \text{ mM}\} \quad (4.26)$$

Since  $c_{inact}^{100 \text{ mM}} > c_{inact}^{10 \text{ mM}}$ , the measured relaxation rate  $R_1$  will be decreased and hence the calculated relaxivity  $r_1$ .

Having discussed the difference between capsules with 10 mM and 100 mM loading, one should continue with the difference between DAH and DAB capsules. The major difference between these two compositions is the number of urea bonds in the polymer shell. It is known that  $-NH_2$  and  $-OH$  groups can chemically exchange protons.<sup>42,87</sup> The exchange rate can be higher than  $10^4 \text{ s}^{-1}$ .<sup>88</sup> This represents an effective means of proton transfer, without the need to exchange a whole water molecule by diffusion through the polymer shell.<sup>89</sup> Because protons of the polymer shell will have a decreased mobility, they will have a decreased  $T_2$



time.<sup>87</sup> To test this, DAB-NC capsules have been synthesized without gadobutrol, to see to which extent the  $T_1$  and the  $T_2$  time are affected by the presence of the polymer shell alone, see Figure 4.19. Though the capsules are without gadobutrol, they are related to a gadolinium concentration. Details can be found in section 7.1.3. The first observation is that  $R_1$  is barely affected by the polymer shell alone. On the other hand  $R_2$  is influenced significantly. The relaxivities for the polymer shells are  $r_1^{dia} = 0.3 \text{ s}^{-1}\text{mM}^{-1}$  and  $r_2^{dia} = 10.3 \text{ s}^{-1}\text{mM}^{-1}$ . This means that the diamagnetic contribution is concentration dependent rather than constant, hence the formula for the relaxivity would actually be written as

$$R_i = R_i^{dia} + r_i^{dia} \cdot [c] + r_i \cdot [c] \quad i \in \{1, 2\} \quad (4.27)$$

where  $r_i^{dia}$  has been introduced, a diamagnetic relaxivity due to the presence of the nanocapsules.

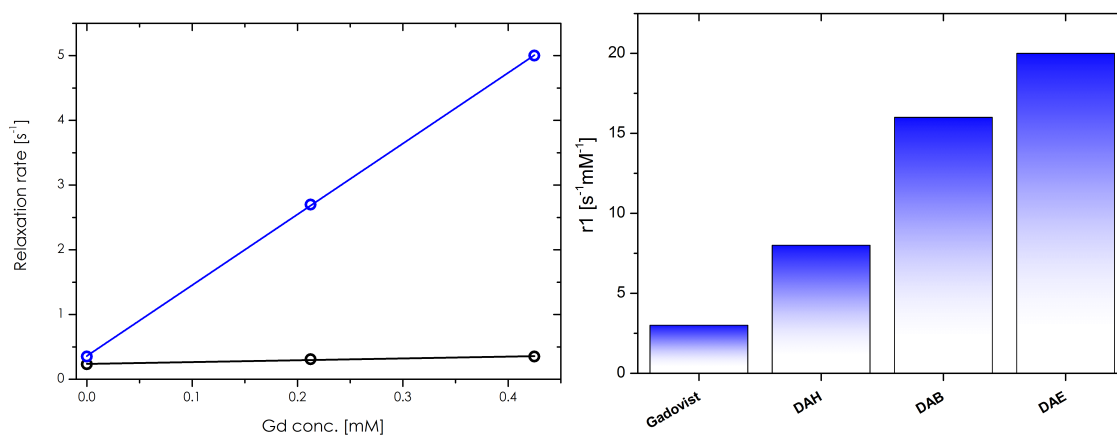


Figure 4.19: Left: Relaxation rates  $R_1$  (black) and  $R_2$  (blue) for DAB-NC for different gadolinium concentrations. Right: Relaxivities  $r_1$  for Gadovist, DAH-NC, DAB-NC and DAE-NC respectively.

In order to further investigate the influence of the nanocapsules on the relaxivity, nanocapsules with DAE have been prepared and the relaxivities are shown on the right side of Figure 4.19. Since the number of -NH groups is increasing with the number of urea bonds, the DAB capsules can exchange more protons than DAH capsules. To further test this assumption, capsules with DAE have been prepared, which increases the density of urea bonds even further. On the right side of Figure 4.19 one can see that the relaxivity increases with the use of DAE in comparison to DAB and DAH like expected. Hence, the relaxivity of the capsules

would be higher, if the proton exchange would be faster. This indicates, that the gadobutrol in the capsules could relax even better if the proton exchange would be higher. Moreover, the transverse relaxivity increases non-linear. To emphasize these results, one can look at the relaxivity for different temperatures. The change in temperature has two consequences. On one hand  $\tau_r$  and  $\tau_D$  are becoming shorter with increasing temperature. On the other hand, the proton and water exchange rate increases with increasing temperature, see left side of Figure 4.20. A decreasing relaxivity with increasing temperature indicates a system in which the water exchange is the limiting factor. If the temperature leads to an increase in relaxivity then the water exchange is the limiting factor. The relaxivity for different systems and temperatures is shown on the right side of Figure 4.20. For gadobutrol the relaxivity decreases

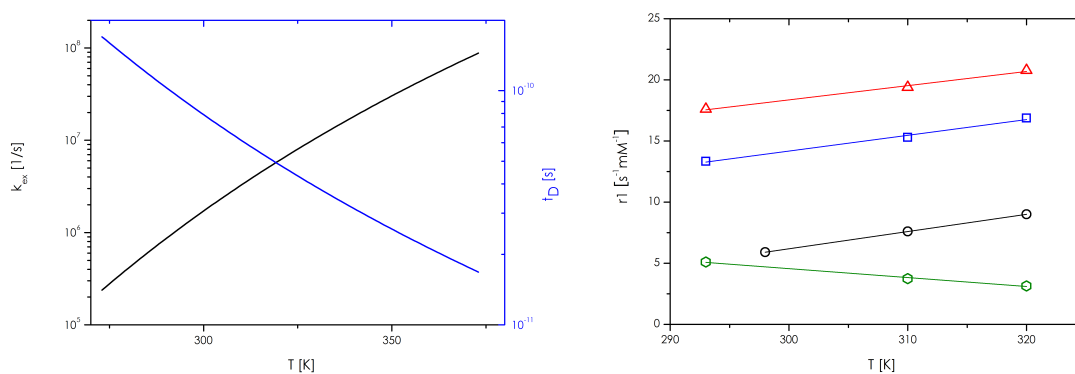


Figure 4.20: Left: Diffusional correlation time  $\tau_D$  (blue line) and water exchange time  $\tau_m$  (black line) for different temperatures. Right: Relaxivity  $r_1$  for DAE-NC (red triangles), DAB-NC (blue squares) and DAH-NC (black circles) and neat gadobutrol (green hexagons).

with increasing temperature, as mentioned above, this indicates a fast exchange system. In comparison, three nanocapsule systems have been investigated, namely DAE-NC, DAB-NC and DAH-NC and for all of them the relaxivity increases with increasing temperature, as expected for systems slowly exchanging protons. However, for the DAE capsules, the relaxivity increases from 293 K to 320 K by only 17%, for DAB by 26% and for DAH by more than 70%. This shows, that for DAH capsules, the relaxivity is quenched because of the slow proton exchange. These findings can be compared to observations of polymersomic systems, for which it has been found, that the relaxivity can be tripled, if water permeation through pores in the polymersomes is enabled.<sup>90</sup>

#### 4.1.4 Increasing relaxivity by co-encapsulation

In the last sections, it was shown, that sucrose can enhance the relaxivity by some orders of magnitude. Furthermore, it has been demonstrated, that the relaxivity can be increased by encapsulation and the resulting change in water molecules diffusion. To combine the beneficial effects, the versatility of nanocapsules has been used to not only encapsulate gadobutrol, but in addition sucrose in DAB-NC.<sup>78</sup> This situation is sketched in Figure 4.21. It has been shown, that the sucrose molecules are distributed within the capsule, rather than being attached to the inner surface of the capsule.<sup>78</sup> Hence, one can assume, that the sucrose within the capsule has the same effect as in solution. On the right side of Figure 4.21, the relaxivity for capsules with co-encapsulated sucrose is plotted in comparison to other capsule compositions. As shown, the relaxivity increases up to a value of  $28.6 \text{ s}^{-1}\text{mM}^{-1}$ , which

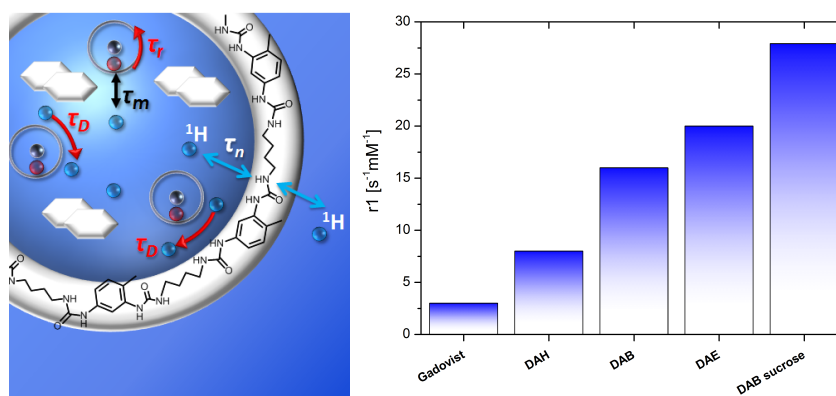


Figure 4.21: Left: Sketch of a nanocapsule, with co-encapsulated sucrose (white hexagons). Because of the encapsulation of viscous sucrose,  $\tau_r$  and  $\tau_D$  in the interior changes. Right: Relaxivity of capsules with sucrose encapsulated in comparison to NC without co-encapsulation.

corresponds to a ten-fold increase in relaxivity in comparison to gadobutrol in water alone. Therefore sucrose has the anticipated effect.

#### 4.1.5 Exchange of water in and out of nanocapsules

As already said, the water exchange from the bulk phase to the inner sphere of the gadobutrol complex is of the utmost importance. To transfer the relaxation effect of the paramagnetic center to the bulk phase outside the nanocapsule, it is equally important to have a fast water

exchange from the bulk phase to the interior of the nanocapsule and *vice versa*. For low molecular weight contrast agents,  $^{17}\text{O}$   $T_2$  measurements have been shown to give analytical access to the water exchange  $\tau_m$  from the inner sphere to the bulk.<sup>71,91</sup> The advantage of  $^{17}\text{O}$  is that, unlike  $^1\text{H}$  it cannot chemically exchange. Hence, in opposition to  $^1\text{H}$ -NMR, one tracks the whole water molecules and not just the single protons. The  $^{17}\text{O}$  transverse relaxivity for  $\text{Gd}^{3+}$  complexes is in contrast to  $^1\text{H}$  relaxation very dependent on the scalar contribution. That is because  $^{17}\text{O}$  is directly bound to the  $\text{Gd}^{3+}$  center, which makes the scalar interaction much stronger than in case of protons, since in the latter case it is mediated over two bonds. For long electronic relaxation times, e.g.  $\omega_0^2 T_{1,e}^2 > 1$ , the relaxivity is written as<sup>82</sup>

$$r_2^{17\text{O}} = \frac{1}{T_{2,m} + \tau_m} = \frac{3}{\frac{1}{S(S+1)\tau_m} \left(\frac{A}{\hbar}\right)^{-2} + \tau_m} \quad (4.28)$$

in which the parameters have their usual meaning but for  $^{17}\text{O}$ , hence  $S = 5/2$  and  $\frac{A}{\hbar} = -2.8 \cdot 10^{-6}$ .<sup>71</sup> Since  $\tau_m$  is temperature dependent, the water exchange can be obtained via temperature dependent  $T_2$  measurements. The outcome of such a measurement is displayed on the left side of Figure 4.22, for which the relaxivity has been measured for a solution of gadobutrol in water. To make sure that the electronic contribution is negligible, the measurement has been performed with an external magnetic field of 700 MHz, for which the electronic relaxation time can be calculated to be on the order of hundreds of nanoseconds. The condition  $\omega_0^2 T_{1,e}^2 > 1$  is then easily fulfilled. As one can see, the relaxivity first increases with temperature up to a certain point, at which  $\tau_m$  is short with respect to  $T_{2,m}$  and hence dominates the expression in equation 4.28. Beyond this point, the relaxivity decreases again. The region before the crossover is the so called slow exchange regime. In this region the relaxivity is determined and limited by slow water exchange. In this area, the relaxivity increases, because with increasing temperature the water exchange gets faster, which in this case is beneficial. After the crossover, the relaxivity decreases with temperature. That is because the water exchange is too fast and  $^{17}\text{O}$  is not sufficiently relaxed anymore. The data points have been fitted with equation 4.28 and for 310 K a water exchange of  $\tau_m$  of  $409 \pm 73$  ns has been obtained, which is above the literature value of  $176 \pm 21$  ns.<sup>71</sup> However, the result is at least the right order of magnitude and considering that only four data points have been acquired and that the confidence interval is rather broad, the result is fair. On

the right side of Figure 4.22, the results for the same measurement are shown but this time for nanocapsules. The relaxivity increases with temperature for all systems, as also indicated

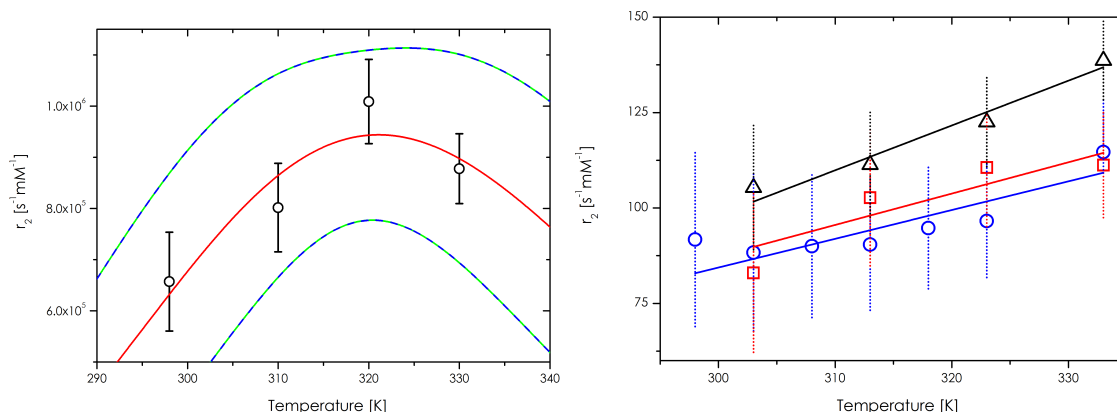


Figure 4.22: Left: Relaxivity  $r_2$  for  $^{17}\text{O}$  for different temperatures and capsule compositions. The errors are calculated via Gauss error propagation, under assumption of a 5% error on the  $T_2$  measurements. The green/blue dashed line for the left diagram indicates the 95% confidence interval, the red curve is the fit to the data points. Right: Same measurement for DAH-NC (red squares), DAB-NC (blue circles) and DAE-NC (black triangles). Lines are linear fits to the data points.

by the line fits. That indicates, that the encapsulated gadobutrol is in the slow exchange regime. For none of the systems was the changeover to the fast exchange regime observed. Also one can state, that within the assumed error, the capsules have around the same time for the water exchange. This demonstrates, that the exchange of whole water molecules is not too different for different systems. If protons would only be exchanged via the whole water molecule, the slow exchange would probably quench the relaxivity.

One should recapture, that in clinical MRI one actually looks at the protons of the water molecules rather than the oxygen. Therefore it is important to have a fast proton transfer, for instance via chemical exchange. The time constant for the water exchange from the bulk to the interior of the capsule will be denoted as  $\tau_n$ , as already introduced in section 3.5, see Figure 4.23. If one imagines a capsule which can not exchange protons with the bulk phase, the protons in the interior will be relaxed immediately after encapsulation of the gadobutrol. However, by that only very few protons can be relaxed whereas the bulk remains completely unaffected and has the relaxation rate of pure water. Therefore one has to counterbalance the

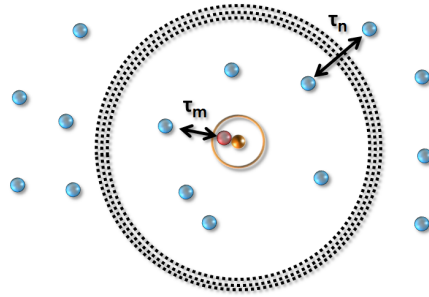


Figure 4.23: Water exchange from the bulk phase to the interior of the capsule  $\tau_n$  and exchange from the interior to the inner sphere of the gadobutrol denoted as  $\tau_m$ .

permeability of the capsule to water or protons, whereas at the same time, the gadobutrol complex should stay encapsulated. Like already mentioned in chapter 3.5 there are several NMR sequences to measure the water exchange from bulk phase to the inner of the capsule, like DEXSY or ARTDECO. In Figure 4.24 ARTDECO has been measured for two physically separated solutions of water and  $\text{CuSO}_4$  and neat ethylene glycol (EG). The system therefore has two components, with two different  $T_2$  times. On the left side of Figure 4.24 one sees the experimental result, in the middle the two dimensional fit and on the right side, the deviation  $d_i$  of the fit from the experimental result, which is simply given by

$$d_i = S_i^{exp} - S_i^{fit} \quad (4.29)$$

where  $S_i^{exp}$  is the signal intensity in the experiment and  $S_i^{fit}$  the signal intensity of the fit for a given point  $i$ . As one can see, is the deviation at nearly all points in the green area, which corresponds to zero percent. Hence, the experimental result is well described by the fit. In

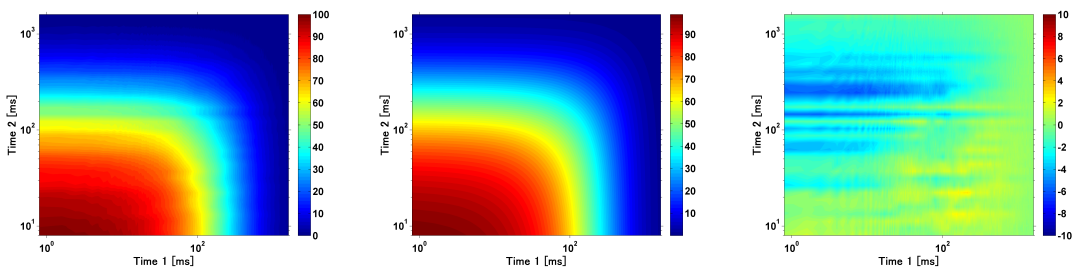


Figure 4.24: Experimental result for ARTDECO for two physically separated solutions of water and EG (left), fit of the experimental result (middle), and the percentage deviation % (right).

Table 4.3 the result from the fit is summarized. To have a measure for the overall quality of

the fit, the deviation  $d_i$  of all points are summed up and divided by the number of acquired points  $n$ , e.g.

$$\sigma = \sum_{i=1}^n \sqrt{d_i^2}/n \quad (4.30)$$

Since the systems are physically separated, there is no exchange at all. Therefore, the

Table 4.3: Parameters obtained from 2D fit on the ARTDECO results.

$\tau_n$ [ms]	$a_{11}$ [a.u.]	$a_{12}$ [a.u.]	$a_{21}$ [a.u.]	$a_{22}$ [a.u.]	$\sigma$
1	53	0	0	50	0.17

measurement has been performed for only one exchange time  $\tau_n$  of 1 ms. As expected for two physically separated samples of equal volume, one gets two components  $a_{11}$  (water) and  $a_{22}$  (EG) of equal size and no exchange components  $a_{12}$ , which would correspond to an exchange of the reservoir of water to that of EG. In the same way  $a_{21}$  is zero.

Now, DAB-NC are measured but without having gadobutrol encapsulated. The reason is the much too short  $T_2$  time of water within the capsule, if gadobutrol is encapsulated, which makes it then difficult to measure a  $T_2$  time. For nanocapsules it is beneficial to use ARTDECO instead of DEXSY, since  $T_2$  is easier to measure and in opposition to diffusion measurements does not destroy the signal. The results are shown in Figure 4.25. Again is on the left side the experimental result, in the middle the two dimensional fit and on the right side the deviation in percent of the fit from the experimental result. The experimental result is well described by the fit, as the right plot of Figure 4.25 is predominantly green.

The parameters obtained from the two dimensional fit of the experimental results are shown in Table 4.4. The experimental results are well described by the fit. The deviation is close to zero in all cases. There is a very predominant component  $a_{22}$  for all exchange times, whereas all the other components are almost negligible, especially the exchange components  $a_{1,2}$  and  $a_{2,1}$ . The difference for  $\tau_n$  of 100 ms is because this exchange times is on the order of the  $T_2$  time. Therefore, the signal has decayed already, which leads to big uncertainties, indicated by a  $\sigma$  threefold higher than for the other exchange times. Apart from that and even more important, there is almost no difference between the different exchange times. As already

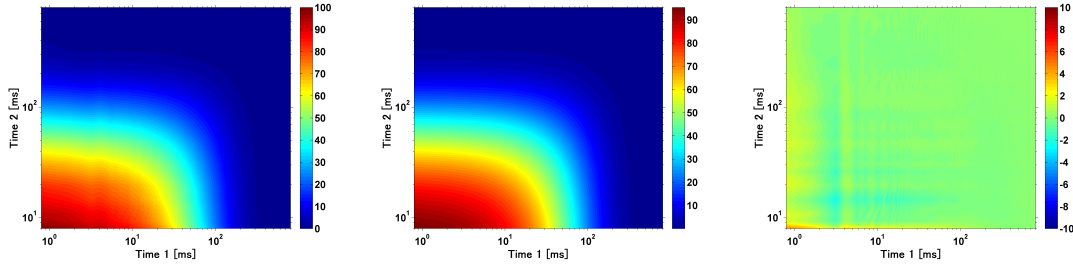


Figure 4.25: Experimental result for ARTDECO with an exchange time of  $100 \mu\text{s}$  (left), fit of the experimental result (middle), and the residuals (right).

Table 4.4: Parameters obtained from 2D fit on the ARTDECO results.

$\tau_n$ [ms]	$a_{11}$ [a.u.]	$a_{12}$ [a.u.]	$a_{21}$ [a.u.]	$a_{22}$ [a.u.]	$\sigma$
0.1	8	3	3	95	0.17
1	10	5	0	98	0.14
5	10	4	0	100	0.14
10	12	4	0	99	0.17
100	1	2	12	100	0.55

mentioned in chapter 3.5, if only one component is measured, this can have two meanings: Either no exchange at all, or an exchange which is so fast, that only an averaged component is measured. The first option is impossible, because that would lead to capsules without any relaxation effect. This is not true as will be shown. The other option means the protons have exchanged already completely and experienced all environments. Then only one component is measured. That indicates, that the exchange must not be slower than some hundred  $\mu\text{s}$ . To reinforce the result, another experiment was performed. This time, the capsules are redispersed not in water but in neat Gadovist. The signal from water molecules, which exchange from the capsule to the bulk phase will immediately decay because of the extremely high relaxation rate of Gadovist. Hence, the signal in the bulk phase is completely suppressed. If the water exchange would be slow, one would only see the signal coming from the interior of the capsules. Because the signal decay in Gadovist is too fast, no  $T_1$  or  $T_2$  relaxation times are measurable, which has been confirmed experimentally. One can only estimate, if



the relaxivity is the same as for low concentrations, that the relaxation rate in the one molar Gadovist solution is around  $R_1 \approx r_1 \cdot [c] \approx 5600 \text{ s}^{-1}\text{mM}^{-1}$ , the  $R_2$  rate is in the same order or even higher. Under the assumption, that  $T_1 \approx T_2 = 1/R_2 \approx T_2^* = 1/(5600\text{s}^{-1}\text{mM}^{-1}) \approx 180 \mu\text{s}$ , the FID in this solution will decay at around three times  $T_2^*$ , hence  $550 \mu\text{s}$ . The FID after accumulation of 4096 scans of pure Gadovist and capsules with water inside and Gadovist in the bulk phase are shown in Figure 4.26. The FID for the neat Gadovist solution

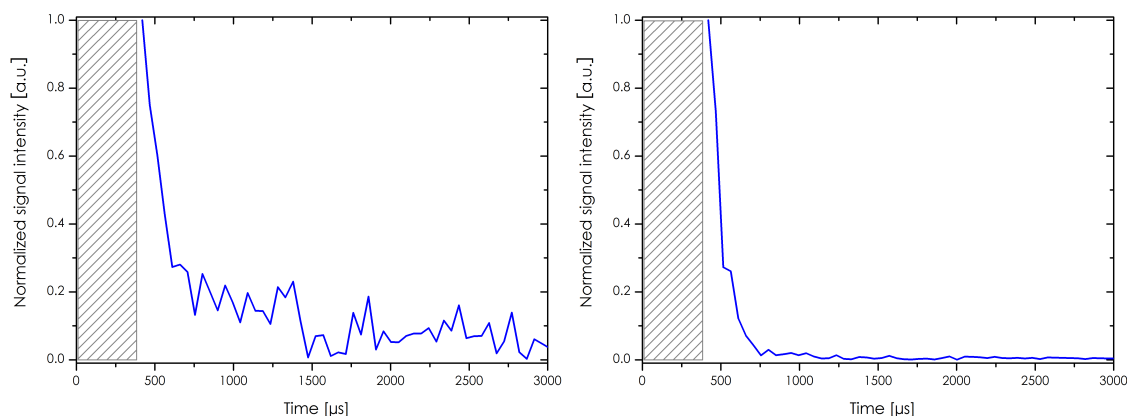


Figure 4.26: FID for 1 molar Gadovist solution (left) and for nanocapsules with water inside and 1 molar Gadovist as bulk phase (right). The gray dashed box indicates the dead time.

decays within some hundred  $\mu\text{s}$ , like expected. Because of the dead time, no signal decaying faster than  $300 \mu\text{s}$  is recordable. The same experiment with the nanocapsules, gives the same result. The signal again decays on the order of hundreds of  $\mu\text{s}$ . Under the assumption, that the exchange is for example on the order of some ms, one would expect two components: One component coming from the water inside the capsule, and another component from the Gadovist outside, which again decays rapidly. Therefore, this experiment goes along with the exchange measurement ARTDECO. In both cases, one can only give an upper limit for the exchange of protons, which must be on the order of, at maximum, some hundreds  $\mu\text{s}$ .

#### 4.1.6 In vivo imaging

To test the performance of the nanocapsules as contrast agents, imaging experiments have been performed *in vitro* as well as *in vivo*. The nanocapsules are DAB-NC capsules, but with an initial gadolinium concentration of 100 mM in the dispersed phase. As seen above, the

relaxivity for capsules with an initial loading of 100 mM is lower than for 10 mM. In this case, the relaxivity  $r_1$  is  $11.4 \text{ s}^{-1}\text{mM}^{-1}$ , whereas the same capsules with 10 mM loading have an  $r_1$  of  $15.9 \text{ s}^{-1}\text{mM}^{-1}$ . However, the total gadolinium concentration in the first case is around 1.5 mM whereas in the latter it is around 0.5 mM. Hence, for the 10 mM capsules  $R_1 = R_1^{dia} + r_1 \cdot [c] = 0.23 \text{ s}^{-1} + 15.9 \text{ s}^{-1}\text{mM}^{-1} \cdot 0.5 \text{ mM} = 8.18 \text{ s}^{-1}$ , whereas in the case of 100 mM capsules it is  $R_1 = 0.23 \text{ s}^{-1} + 11.4 \text{ s}^{-1}\text{mM}^{-1} \cdot 1.5 \text{ mM} = 17.3 \text{ s}^{-1}$ . Hence, the low relaxivity is counterbalanced by a higher total gadolinium concentration, resulting in a higher total relaxation rate. To be compatible with physiological conditions, the capsules have been redispersed in a 0.9 wt% NaCl solution for which the  $T_1$  and  $T_2$  time was found to be comparable to neat water (data not shown). The *in vitro* results are compared to 1 wt% agarose, which is known to mimic  $T_1$  and  $T_2$  times that can arise *in vivo*.<sup>92,93</sup> As a control, pure water has been imaged too. The results of the *in vitro* experiments are shown in Figure 4.27. The solution with nanocapsules appears very bright in comparison to the 1

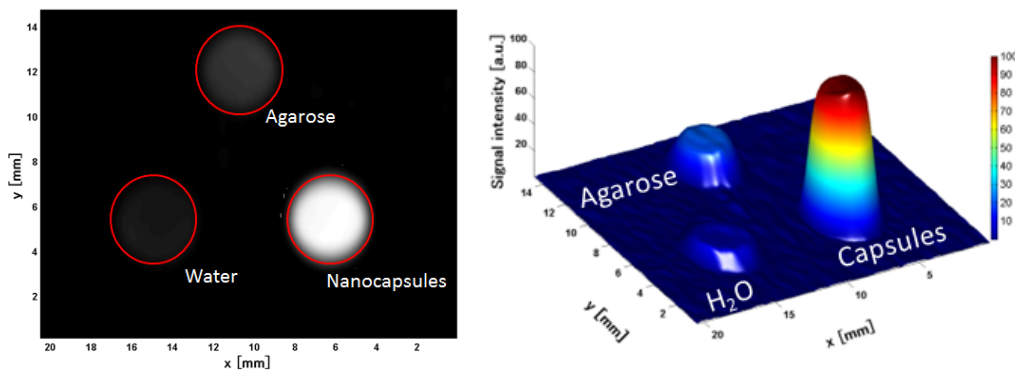


Figure 4.27: Left: Coronal view for solutions of DAB capsules in a ratio 1:1.5 to TDI and a gadolinium loading of 100 mM, agarose and neat water. Right: Signal intensity in three dimensions. The sequence was a spin echo sequence with a repetition delay of 300 ms and an echo time of 8 ms.

wt% agarose and even brighter in comparison to water. In fact, only if the signal intensity is shown in three dimensions, like done on the right side of Figure 4.27, one is able to identify the water signal at all. In the sequence, a short repetition delay of 300 ms has been chosen to obtain a  $T_1$  weighted image. This prevents the slowly relaxing agarose and water from recovering their thermal magnetization and gives rise to a diminished signal intensity. In opposition to that the nanocapsule solution has an  $R_1$  of  $17.3 \text{ s}^{-1}$ , which equals a  $T_1$

time of 55 ms. Hence, the 300 ms are sufficient to fully recover the magnetization, which eventually leads to the bright signal. Though the *in vitro* experiments are very promising, the conditions that arise *in vivo* are very different. The blood interacts with the nanocapsules in a very different way than water, the capsules flow in the blood stream and must withstand shear forces and macrophages can take up nanocapsules which can slow down the water exchange. These are just few examples which can change the relaxation behavior in a way that is hardly influenceable. Therefore, *in vivo* experiments must demonstrate the benefit of encapsulated gadobutrol and that the nanocapsules are working in the anticipated way. For the experiments, a C57BL/6 (B6, or black 6) laboratory mouse was used, with a total weight of around 26 g. The images have been acquired by Dipl. Ing. Andrea Kronfeld (University Medical Center, Mainz). The first image 4.28 is the coronal view of the mouse. On the left side is the mouse before the nanocapsules have been injected into the tail vein. On the right side approximately 15 min after injection of the nanocapsules. The tail vein shows up

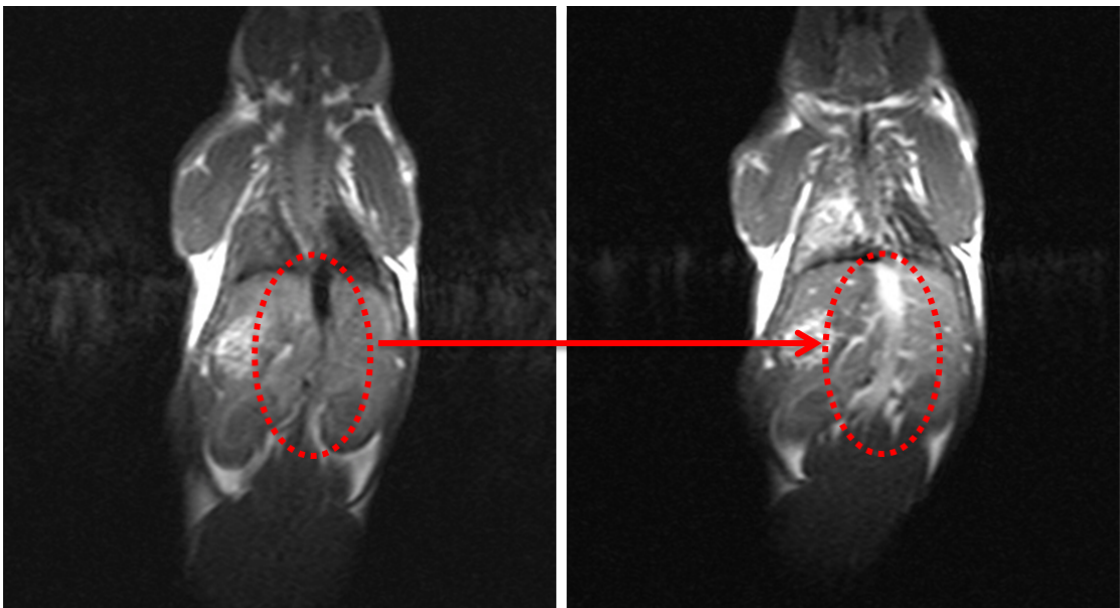


Figure 4.28: MR image of a mouse in coronal view. Left side prior to injection of nanocapsules, right side post injection. Red dashed circle mark the vein.

intensely after the nanocapsules have been injected. It is even possible to see smaller blood vessels, which are barely visible in the native image. In the next plane of the coronal view, the heart shows up, see Figure 4.29. The heart also is much brighter after the nanocapsules

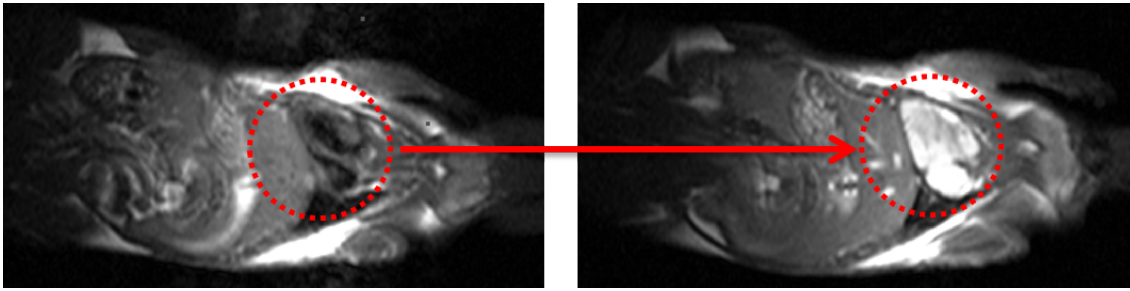


Figure 4.29: MR image of a mouse in coronal view. Left side prior to injection of nanocapsules, right side post injection. Red dashed circle highlights the heart.

have been injected. The images nonambiguously demonstrate that the nanocapsules can work as contrast agents. Since the signal intensity is directly correlated to the position of the nanocapsules one can see where the capsules are going to with time, see Figure 4.30. The signal intensity has been analyzed for different times and areas of the body, for details see the experimental section 7.1.4. At time zero, one has an intensity of 25 in arbitrary

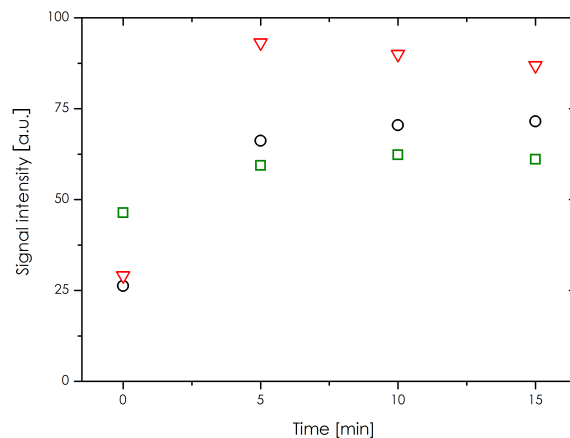


Figure 4.30: Signal intensity in different region (Heart [red diamond], vein [black circles] and liver [green squares]) for different times.

units for the vein and the heart and around 50 for the liver. Five minutes after injection, the intensity at the vein has increased threefold and for the heart fourfold. That corresponds approximately to the situation already observed in the *in vitro* experiments. For the liver, the increase is not that high, probably because the time of observation is too short to see the nanocapsules accumulating. Unfortunately the mouse died approximately 20 min after injection because of an erroneous anesthesia.

## 4.2 Negative contrast agents<sup>#</sup>

Having discussed positive contrast agents in the last section, this section is about  $T_2$  contrast agents. It starts with a short introduction to the investigated systems. Then the theory behind transverse relaxivity will be introduced and used to explicitly calculate the transverse relaxivity. Afterward, a second approach to predict transverse relaxivities will be introduced, which is especially helpful for nanocapsules. Subsequently, the last subsection compares and evaluates the results gained by the two different approaches.

### 4.2.1 Introduction of the systems

All systems have been prepared by Dr. Markus Bannwarth.<sup>24,95</sup> In total ten different  $T_2$  contrast agents are investigated, which can be divided into three groups. The first group are single SPIOs with different diameter, namely  $8 \pm 1$  nm,  $16 \pm 3$  nm and  $20 \pm 4$  nm. The second group are nanoparticles of diameter  $146 \pm 39$  nm and  $156 \pm 46$  nm, see Figure 4.31. Both NPs are loaded with 8 nm SPIOs. The last group are nanocapsules with diameter of 250

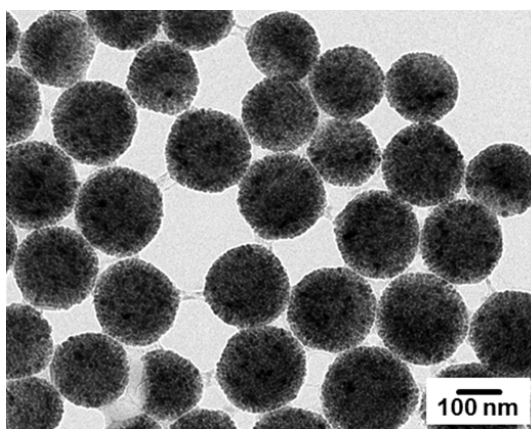


Figure 4.31: Transmission Electron Microscopy (TEM) image of NP-156.

<sup>#</sup>This section in parts is based on the publication "How Morphology Influences Relaxivity - Comparative Study of Superparamagnetic Iron Oxide/Polymer Hybrid Nanostructures" by Sandro Ebert, Markus B. Bannwarth, Anna Musyanovich, Katharina Landfester and Kerstin Münnemann in *Contrast Media and Molecular Imaging*, 2015<sup>94</sup> and on the publication "Tailor-Made Nanocontainers for Combined Magnetic-Field-Induced Release and MRI" Markus B. Bannwarth, Sandro Ebert, Maximilian Lauck, Ulrich Ziener, Stephanie Tomcin, Gerhard Jakob, Kerstin Münnemann, Volker Mailänder, Anna Musyanovych and Katharina Landfester in *Macromolecular Bioscience*, 2014.<sup>24</sup>

$\pm 76$  nm, which are loaded with 10 nm SPIOs,  $400 \pm 121$  nm loaded with 20 nm SPIOs and three nanocapsules with a diameter of  $200 \pm 51$  nm, which are loaded to different amounts with 16 nm SPIOs, see Figure 4.32.<sup>24</sup> All of the systems are named according to their

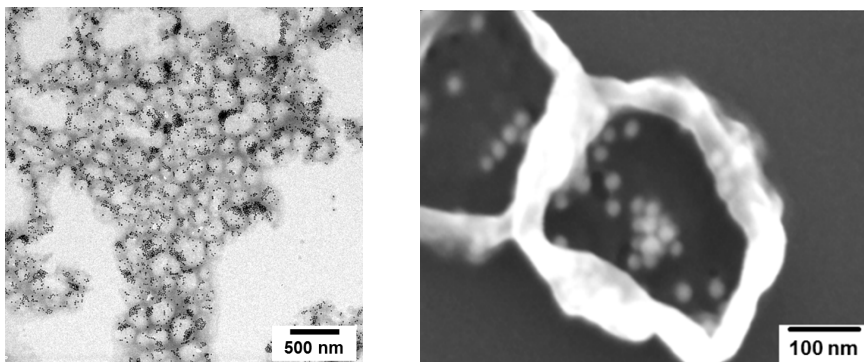


Figure 4.32: Left: TEM image of NC-200-H. Right: Scanning Electron Microscopy (SEM) image of NC-400.

morphology and diameter, hence S-8, S-16 and S-20 for the 8 nm SPIO, the 16 nm SPIO and the 20 nm SPIO, respectively. In the same way, the nanoparticles are called NP-146 and NP-156 and the nanocapsules NC-250 and NC-400. The nanocapsules loaded with S-16 SPIOs will be called NC-200-L, NC-200-M and NC-200-H, where L stands for the lowest, M for a medium and H for the highest loading with S-16 SPIOs, respectively. Please note, that in the given reference, NC-200-L, NC-200-M and NC-200-H are named VA-060-Low, VA-060-Med and VA-060-High, respectively. For all systems, the longitudinal relaxivity  $r_1$  is smaller than  $2 \text{ s}^{-1}\text{mM}^{-1}$  (data not shown). As already mentioned in the theoretical section,  $R_1$  decreases for too long correlation times, see also Figure 2.3 in section 2.1. This leads to an often observed low  $r_1$  value.<sup>25,96</sup> For example, Ai *et al.* found magnetite loaded micelles, which have an  $r_2$  as high as  $471 \text{ s}^{-1}\text{mM}^{-1}$ , but for the same system an  $r_1$  as low as  $2 \text{ s}^{-1}\text{mM}^{-1}$ .<sup>97</sup>

#### 4.2.2 Theory and simulation of transverse relaxivity

The relaxation rates of the introduced systems can be simulated in a semi-empirical approach. To analyze the nanoparticles and nanocapsules, they were assumed to behave as clusters of SPIOs. They are treated as weakly magnetized particles, like is common in literature.<sup>98</sup>

This is sketched in Figure 4.33. To prevent the SPIOs from agglomeration, they are coated

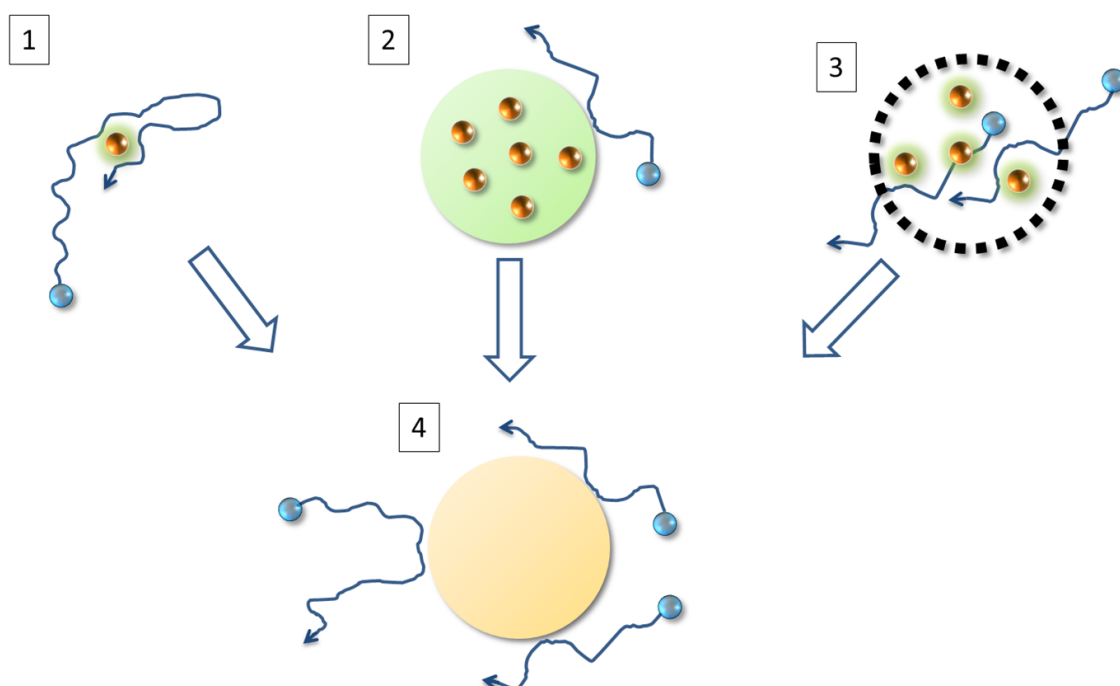


Figure 4.33: Different NP and NC morphologies (1,2 and 3) and how they are included in the simulation (4). Blue spheres stand for water, orange spheres for iron oxide particles, black dashed circles for the polymeric shell, green areas for polymeric material.

with oleate, which is estimated to result in an 1 nm layer around the SPIO. Hence, the magnetic field felt by the water molecules diffusing near the SPIO is effectively reduced.<sup>99</sup> The SPIO then behaves like a weakly magnetized sphere, which has a larger effective radius of  $r_{SPIO}^{eff} = r_{SPIO} + d$  where  $r_{SPIO}$  denotes the radius of the iron oxide core and  $d$  the coating thickness. Because there is no formalism to explicitly consider the coating of SPIOs or the polymer shell around NPs, the hydrodynamic radii experimentally determined by DLS have been used for the simulations. In principal the inner and outer sphere relaxivity theory depicted for  $T_1$  contrast agents also holds true for negative contrast agents. But the inner sphere contribution is negligible in comparison to outer sphere contributions.<sup>10</sup>

Even more important is an effect experimentally observed by Josephson *et al.* but not predicted by SBM theory and the Freed model.<sup>25</sup> According to Josephson the relaxivity of iron oxides first increases with the particle size, but above a certain level starts to decrease,

whereas the SBM theory and Freed model predict a steadily increasing relaxivity with increasing particle size. The experimental observations of Josephson have been underlined by Monte Carlo simulations of a group in Belgium.<sup>26</sup> Roch, Gillis, Muller, Brooks *et al.* derived a set of equations feasible to describe the observed behavior.<sup>26, 60, 100–103</sup> An overview can be found in a recent review.<sup>10</sup>

The iron oxide containing nanoparticle is considered as a large magnetized sphere, with a total magnetic moment growing according to Langevin's law

$$M = N\mu_{sp}L(x) \quad (4.31)$$

with  $N$  being the number of iron oxides per particle,  $\mu_{sp}$  the magnetic moment of one iron oxide,  $L(x)$  the Langevin function

$$L(x) = \coth(x) - 1/x \quad (4.32)$$

and

$$x = \frac{N\mu_{sp}B_0}{k_B T}. \quad (4.33)$$

In equation 4.33  $\mu_{sp}$  denotes the magnetic moment of one elementary iron oxide crystal.

Before making the next steps, one defines  $\Delta\omega$ , the difference in Larmor frequency between the bulk water and the one at the surface of the nanoparticle<sup>10, 102</sup>

$$\Delta\omega = \frac{\mu_0 M \gamma_I}{3} \quad (4.34)$$

with  $M$  being the particle magnetization. The relaxation behavior is now divided in three regions:<sup>10, 102</sup>

1.) Motional averaging (MA) regime in which are mostly small nanoparticles. For these small nanoparticles, the magnetic field is averaged to zero by the diffusion of the water molecules around the particle.<sup>58, 59, 102</sup> To fall into this regime, nanoparticles must fulfill  $\Delta\omega\tau_D < 1$ , with  $\tau_D$  the diffusional correlation time like defined in equation 4.12. The relaxation rate then is given by

$$R_2 = 16/45 \cdot f_A \Delta\omega^2 \tau_D \quad (4.35)$$

All parameters are denoted like above. In the motional averaging regime  $T_2$  equals  $T_2^*$ . That is because  $\tau_D$  is much shorter than usual echo times of some hundred  $\mu_s$ . Refocusing pulses



are inefficient then, because the environment of a particle changes faster than the refocusing pulse can rephase the spins.

2.) Static dephasing (SD) regime for intermediate size particles for which  $\tau_D > \frac{\pi\sqrt{3}}{2\Delta\omega}$  holds true. The static dephasing regime originally was introduced by Brown.<sup>104</sup> He assumed uniformly distributed and motionless magnetic grains, which do not affect each other. These particles act as magnetic moments which do not move. The condition  $\tau_D < \tau_L$  must be fulfilled<sup>102</sup> with

$$\tau_L = \frac{1.49}{\Delta\omega} x^{1/3} (1.52 + f_{NP}x)^{5/3} \quad (4.36)$$

and  $x = \Delta\omega t_E/2$ ,  $t_E$  the echo time between two 180° pulses in a CPMG echo train, and  $f_{NP}$  the volumetric fraction between nanoparticles and solution.  $R_2$  then is given by

$$R_2 = R_2^* = 2\pi\sqrt{3}f_{NP}\frac{\Delta\omega}{9} \quad (4.37)$$

3.) The so called echo limiting (EL) regime in which the big particles are found.<sup>100</sup> In this regime, the relaxivity is a function of the echo time between two 180° pulses, hence the echo time. If  $\tau_D > \tau_L$  the relaxation rate decrease with the radius<sup>101</sup>

$$R_2 = 1.8f_{NP}x^{1/3}(1.52 + f_{NP}x)^{5/3}/\tau_D. \quad (4.38)$$

For all three regions the phase shift  $\phi$  of a proton due to the presence of a magnetic particle inducing a field  $B$  is

$$\phi = B\gamma_I t \quad (4.39)$$

where  $t$  is the the time of the proton in this field.<sup>104</sup>

From an MRI point of view, equation 4.38 is interesting, because of two points: First of all, it is obvious that the relaxation rate decreases with the radius of the nanoparticle. Secondly, the echo sequence plays an important role. If the echo times are too long, the refocusing pulses are still inefficient like in the MA regime. But if the echo time  $t_E$  is short enough, it gets into the same region of the diffusion time  $\tau_D$  of the nanoparticles. That makes refocusing pulses efficient and in the end the difference between  $T_2$  and  $T_2^*$ .

The three different regimes are shown in in Figure 4.34. In the first regime there is no difference between  $T_2$  and  $T_2^*$ , refocusing pulses are inefficient because they are too long

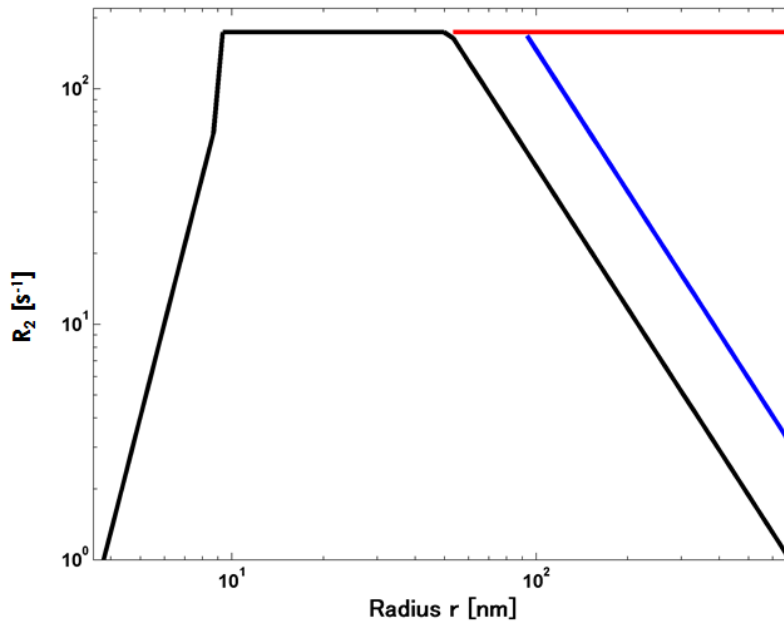


Figure 4.34: Relaxation rate  $R_2$  for increasing nanoparticle radii and different regions. In this example, the MA regime is up to a size of around 10 nm. The region of the plateau is given by the SD regime. In the EL regime,  $T_2^*$  is still constant (red line), whereas  $R_2$  is decreasing (black line). The blue line is simulated for an echo time which is longer than in case of the black line.

in comparison to the diffusion time. The plateau is described by the SD regime. Above a certain size, in the EL regime,  $R_2$  start to decrease whereas  $R_2^*$  stays constant at the level of the static dephasing regime. Additionally the relaxation rates for two different echo times are shown. Like expected, the relaxation rate is increasing with longer echo times. The different regimes are not as strictly separated as one might expect. Rather the different conditions must be understood as approximations. This is also the reason why the curve has no smooth transitions between different regimes.<sup>60</sup>

Having introduced the basic equations, the relaxivities can be simulated. All simulations again have been performed with Matlab, the corresponding code can be found in section 8.3.3. First, with the help of Thermogravimetric Analysis (TGA) the number of SPIOs in a nanoparticle and the number of nanoparticles in a given volume were calculated. The volume occupied by inorganic content is denoted as  $\%_{TGA}$ , with which the average density of a

particle calculated to be

$$\rho = \rho_{SPIO} \cdot \%_{TGA} + (100\% - \%_{TGA}) \cdot \rho_{Polymer} \quad (4.40)$$

with  $\rho_{SPIO}$  and  $\rho_{Polymer}$  being the weight density of a SPIO and the polymer of a NP, respectively. One particle then has the mass  $m$  of

$$m = \frac{4}{3} \cdot \pi \cdot r_{NP}^3 \cdot \rho \quad (4.41)$$

in which  $r_{NP}$  is the particle radius. The solid content per volume is obtained with solid content analysis, and is named  $\rho_{sc}$ . The number of particles per volume is then calculated with

$$Z = \frac{\rho_{sc}}{m} \quad (4.42)$$

The iron oxide mass  $m_{Fe_3O_4}$  can be calculated with  $m \cdot \%_{TGA}$ . The iron oxide core mass of a SPIO is calculated with

$$m_{SPIO}^{core} = \frac{4}{3} \cdot \pi \cdot r_{SPIO}^3 \cdot \rho_{Fe_3O_4} \quad (4.43)$$

where  $r_{SPIO}$  is the iron oxide core radius and  $\rho_{Fe_3O_4}$  the weight density of magnetite. The radii of SPIOs has been analyzed via TEM images. In one nanoparticle one has  $Z_{SPIO}$  SPIOs, which is calculated with

$$Z_{SPIO} = \frac{m_{Fe_3O_4}}{m_{SPIO}^{core}} \quad (4.44)$$

For SPIOs  $Z_{SPIO}$  is one. In nanocapsules a big part is water, hence the approach to calculate the number of SPIOs is different. The number of capsules is calculated directly with the solid content

$$Z_{NC} = \frac{\rho_{sc} (100\% - \%_{TGA})}{\rho_{Polymer} \frac{4}{3} \pi (r_{NC}^3 - (r_{NC} - l)^3)} \quad (4.45)$$

where  $r_{NC}$  denotes the hydrodynamic radius of the capsule and  $l$  the thickness of the capsule wall. Based on TEM images, the capsule wall thickness is estimated to be 15 nm. The mass  $m_{NC}$  of one nanocapsule is then calculated with

$$m_{NC} = \frac{\rho_{sc}}{Z_{NC}} \quad (4.46)$$

The number of SPIOs in one NC is calculated analogue to NPs. With ICP-OES the iron concentration  $[Fe]$  is determined. Since the concentration is proportional to  $\%_{TGA}$ , the number of particles in a volume of one liter and for a concentration of 1 mM can be calculated. For the next step, the intra-aggregate volume  $\phi_{int}$  needs to be introduced, which is the ratio of the volume of iron oxide in a nanoparticle to the total volume of the nanoparticle.<sup>98, 105</sup> In this way the reduced iron content in a particle is considered, since big parts are polymer. For the capsules,  $\phi_{int}$  is calculated as ratio of the volume of iron to the volume of polymer and iron, being equivalent to subtracting the water core from the capsule. Otherwise the volume fraction  $f_A$  would be overestimated. That in turn would lead to an overestimation of the iron content and eventually to the overestimation of the relaxivity. The volume fraction  $f_A$  of particles or capsules is then given by

$$f_A = Z \cdot \frac{4}{3} \pi \cdot r_{ex}^3 \cdot \phi_{int} \quad ex \in \{SPIO, NP, NC\} \quad (4.47)$$

To calculate the magnetization  $M$  of the SPIO iron oxide core, the saturation mass magnetization is needed and can be determined with VSM.

$$M = m_s \cdot \rho_{Fe_3O_4} \quad (4.48)$$

where  $\rho_{Fe_3O_4}$  is the density of magnetite. Because the SPIOs have a oleate coating on top, the magnetic field felt by the water molecules is effectively reduced. That makes the SPIO acting as a weakly magnetized sphere, which has then an effective radius of

$$r_{SPIO}^{eff} = r_{SPIO} + d \quad (4.49)$$

The frequency shift  $\Delta\omega_{SPIO}$  of the SPIO is then calculated as

$$\Delta\omega_{SPIO} = \frac{\mu_0 \gamma_I M}{3} \cdot \frac{r_{SPIO}^3}{(r_{SPIO} + d)^3} \quad (4.50)$$

where  $d$  is the thickness of oleate coating. To calculate the frequency shift  $\Delta\omega_{NP}$  of clustered magnetic nanoparticles, the magnetization of this cluster is needed, which is given by<sup>106</sup>

$$M_{NP} = Z_{SPIO} \cdot M \cdot \frac{r_{SPIO}^3}{r_{NP}^3} \quad (4.51)$$

With that the frequency shift is given by

$$\Delta\omega_{NP} = \frac{\mu_0 \gamma_I M_{NP}}{3} \quad (4.52)$$

The magnetization  $M_{NC}$  of NCs and the frequency shift  $\Delta\omega_{NC}$  is calculated in the same way. After the fundamental parameters have been calculated and set in the Matlab code, the relaxivities for the different systems are simulated with the equations introduced above. All systems are redispersed in 1 wt% Agarose, for which the diffusion coefficient of water is assumed to be the one in neat water. It has been found, that this is a very good approximation.<sup>43</sup>

### 4.2.3 The unified approach

Vuong *et al.* performed a Monte Carlo (MC) simulation on the classical theory and gained an unified equation describing all three regimes with one equation.<sup>27</sup> This approach has one major advantage over the "classical" theory: It explicitly distinguishes for nanocapsules between the "outer sphere" contribution, e.g. water that is relaxed by seeing the NC as a weakly magnetized sphere and the "inner sphere" contribution, stemming from water relaxed by the single SPIOs in the NC. The terms outer sphere and inner sphere must not be confused with the one used like in the case of  $T_1$  contrast agents. In addition, this approach allows water to diffuse into and out of the capsule. The simulation should therefore lead to significantly better results in comparison to the classical theory, which is not considering the inner sphere contribution. In one publication, SPIO loaded vesicles have been compared to MC simulations.<sup>107</sup> However, the authors were interested in the understanding of unexpected relaxation rate behavior and not in developing a fundamental theory. Consequently, the authors did not present any equations in the given reference. The equation describing all three regimes is

$$r_2^{unif}(r, B_{eq}, f_A) = f_A \frac{(a \cdot B_{eq} \cdot r)^2}{1 + b \cdot r \cdot B_{eq}^\alpha + (c \cdot r \cdot B_{eq}^\alpha)^2 + (d \cdot r \cdot B_{eq}^\alpha)^3 + (e \cdot r \cdot B_{eq}^\alpha)^4} \quad (4.53)$$

in which  $r$  is the radius of the particle,  $B_{eq}$  the equatorial field of the particle,  $\alpha = 0.42$ ,  $a = 2.5209 \cdot 10^{12}$ ,  $b = -0.177 \cdot 10^9$ ,  $c = 0.1295 \cdot 10^9$ ,  $d = 0.0532 \cdot 10^9$ , and  $e = 0.0566 \cdot 10^9$ .<sup>27</sup> For non-agglomerated systems like a single SPIO, the radius  $r$  is equal to the effective SPIO radius as denoted in equation 4.49. The equatorial field is

$$B_{eq} = \frac{\Delta\omega_{SPIO}}{\gamma_l} \quad (4.54)$$

Hence, the relaxivity is given by

$$r_2^{SPIO} = r_2^{unif}(r_{SPIO}^{eff}, B_{eq}, f_A) \quad (4.55)$$

The relaxivity for NPs is calculated in the same manner by  $r_2^{unif}(r_{NP}, B_{NP}, f_{NP})$  in which  $r_{NP}$ ,  $B_{NP}$ , and  $f_{NP}$  stand for the hydrodynamic radius, the equatorial field, and the volume fraction of the NP, respectively. The equatorial field is given by

$$B_{NP} = Z_{SPIO} B_{eq} \left( \frac{r_{SPIO}^{eff}}{r_{NP}} \right)^3 \quad (4.56)$$

For nanocapsules, one gets two contributions, one for the NCs acting as a weakly magnetized sphere, for which the bulk volume fraction is

$$f_{bulk} = Z_{NC} \frac{4}{3} \pi r_{NC}^3 \phi_{int} \quad (4.57)$$

The equatorial field  $B_{NC}$  is calculated analog to equation 4.56 by replacing the NP radius  $r_{NP}$  with the NC radius  $r_{NC}$ . Since the NC is carrying SPIOs, which itself can relax protons, one has a second component for the volume fraction, which is the volume fraction of the SPIOs inside the NC,

$$f_{inner} = Z_{SPIO} \cdot \left( \frac{r_{SPIO}^{eff}}{r_{NC} - l} \right)^3 \cdot \phi_{int} \quad (4.58)$$

where  $f_{inner}$  stands for the inner aggregate fraction and  $\phi_{int}$  corresponds to  $\phi_{int}$  of the SPIOs. Now, one has two relaxation rates: One coming from the weakly magnetized NC, and one coming from single SPIOs inside the NC. In the limiting case of very fast exchange between bulk water and water inside the capsule, the relaxivity can be calculated with

$$r_2^{NC} = p_{Bulk} \cdot r_2^{unif}(r_{NC}, B_{NC}, f_{bulk}) + p_{inner} \cdot r_2^{unif}(r_{SPIO}^{eff}, B_{eq}, f_{inner}) \quad (4.59)$$

where  $p_{bulk}$  is the fraction of water molecules outside the capsule, and  $p_{inner}$  the one inside the capsules. Of course, the fraction outside the NC is nearly one, whereas  $p_{inner}$  is very small. For NCs the water exchange plays a crucial role, which is considered in the case of the unified approach resulting in  $r_2^{MC}$ . This exchange gives rise to a second contribution, stemming from water coming in contact to single SPIOs, besides that coming from the NC as a weakly magnetized sphere. The complete situation is sketched in Figure 4.35.

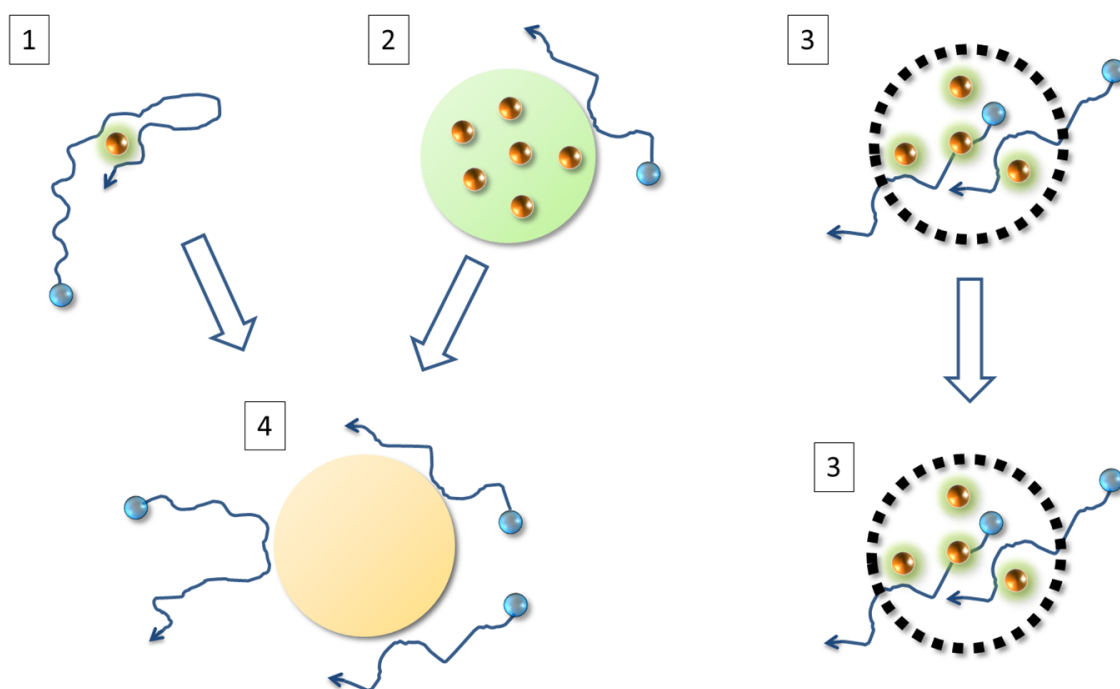


Figure 4.35: Different NP morphologies (1,2) and how they are included in the simulation (4). NC morphology (3) is included as it is. Blue spheres stand for water, orange spheres for iron oxide particles, black dashed circles for the polymeric shell, green areas for polymeric material.

#### 4.2.4 Results and discussion

To differentiate the relaxivities simulated with the classical approach and the one gained with the unified approach, they are called  $r_2^{class}$  and  $r_2^{MC}$ , respectively. The main parameters for the different systems and outcome of the simulation is summarized in Table 4.5. The single SPIOs are all in the MA regime. They have an increasing relaxivity with increasing diameter, like expected. Only S-20 did not fit into the MA nor the SD regime, either the criterion  $\Delta\omega\tau_D < 1$  failed, because  $\Delta\omega$  and  $\tau_D$  are already too big or just not big enough to fulfill  $\tau_D > \frac{\sqrt{3}}{2\Delta\omega}$ . However, as mentioned above, the different regimes are not as clearly separated as one might expect from the given conditions.<sup>98,101</sup> If S-20 is placed in the MA regime, the simulation almost fits the experiment, if it is placed in the SD regime, the simulation overestimates the experimental result by 200%. This is why S-20 is placed in the MA regime, which is considered to describe SPIOs the best. For particles that are in the transition zone

Table 4.5: Each column is: The system, the number of SPIOs per NP or NC, the measured  $r_2$ , simulated  $r_2$  by the classical approach and simulated  $r_2$  with the unified approach, respectively.

System	$Z_{SPIOs}$	$r_2$ [ $s^{-1}mM^{-1}$ ]	$r_2^{class}$ [ $s^{-1}mM^{-1}$ ]	$r_2^{MC}$ [ $s^{-1}mM^{-1}$ ]
S-8	1	$99 \pm 9$	69	43
S-16	1	$140 \pm 14$	100	121
S-25	1	$167 \pm 18$	158	122
NP-146	468	$216 \pm 12$	94	76
NP-156	3959	$165 \pm 5$	253	281
NC-250	33	$43 \pm 10$	10	51
NC-400	959	$114 \pm 4$	13	19
VA-060-Low	24	$55 \pm 3$	13	89
VA-060-Med	39	$120 \pm 11$	13	89
VA-060-High	89	$96 \pm 9$	96	231

between two different regimes, polydispersity can lead to circumstances in which some parts of the sample are in one regime, whereas the rest of the sample is actually in another regime.<sup>98</sup> The most interesting point for the SPIOs is probably the underestimation of the measured values by a factor of two, in the case of the unified approach, resulting in a low  $r_2^{MC}$ . Deviations this high have already been reported in the original publication of Vuong *et al.*<sup>27</sup> There they investigated a system which is pretty close to S-8, namely SPIOs with radius of 5 nm and a magnetization of 320 kA/m, for which they get an  $r_2^{ex}$  of  $100 s^{-1}mM^{-1}$  and a  $r_2^{MC}$  of  $50 s^{-1}mM^{-1}$ . Both results fit well with the corresponding results gained here. Vuong *et al.* attributed this deviation to the polydispersity of the samples. Generally speaking, the polydispersity of samples in combination with size determination by TEM and DLS can lead to big uncertainties.<sup>108,109</sup> To see the dramatic influence on the relaxivity, the  $r_2$  for different iron oxide sizes has been simulated. But this time a second simulation has been performed in which the radius has a Gaussian noise of 25% of the radius, which correspond to the situation of a 25% size deviation as observed for the different systems. That means, the values that the radius can take on are in the area of  $r \pm 0.25 \cdot r$ . The result is shown in Figure 4.36. The



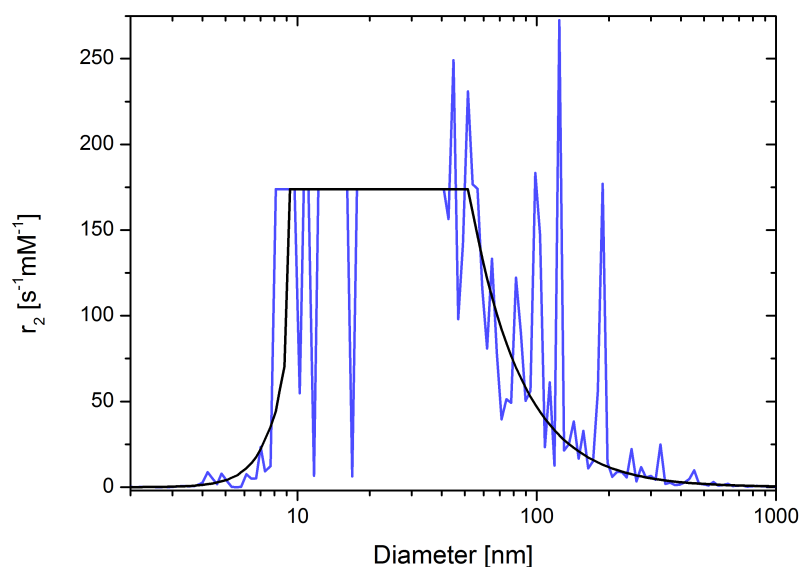


Figure 4.36: Relaxivity  $r_2$  for different sizes of the iron oxide cluster. Black curve is simulated without noise, blue curve is simulated with 25% gaussian noise on the radius.

outcome nonambiguously demonstrates, that the error on the radius can lead to a situation, in which the simulated relaxivity is far off the experimental relaxivity. Moreover, to demonstrate the effect of the coating, the magnetic field around a S-8 has been simulated with COMSOL Multiphysics 4.3, see Figure 4.37. One can see, how the magnetic flux density around the SPIO gradually decreases as one goes away from the surface. If one imagines a hydrophobic coating on top, it is easy to see, that the magnetic field has already decreased to much smaller values, even for a distance as low as 1 nm. In all theories, magnetic nanoparticles are treated as weakly magnetized spheres, without taking into account the special conditions that may arise by the use of different coatings.<sup>110</sup> For example it is known, that a hydrophilic coating on magnetic particles can drastically change the diffusion coefficient in the closer environment of the cluster, which in turn impacts the relaxivity.<sup>111</sup> Also, the size of the coating around a SPIO is often just estimated, which leads to erroneous estimations of the radii and again to wrong relaxivities. Especially in the case of small particles, the coating can heavily influence the radius. Though there is still no exact procedure to account for the coating, it is possible to consider polydispersity in the simulation.<sup>108</sup> Unfortunately, because of the already mentioned impact of the coating on the relaxivity, it is hardly possible to compare different values found in literature. For example Jun *et al.* investigated a system

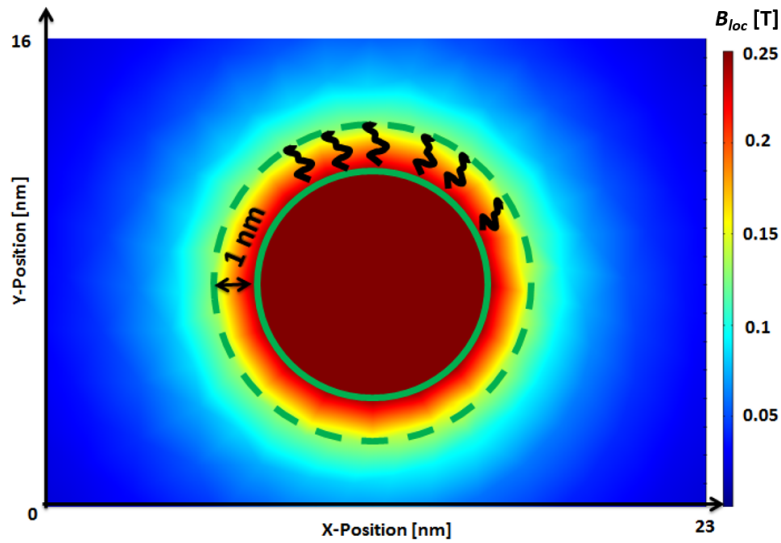


Figure 4.37: Simulation of the magnetic flux density  $B_{loc}$  induced by a SPIO with 8 nm radius. The black wiggly lines, bordered by the green dashed line, indicate a coating on top of the iron oxide core. The green circle indicates the iron oxide core.

with a diameter of 9 nm and a magnetization of 80 emu/g, which is comparable to S-8. Still, they found relaxivities which are 30% higher.<sup>112</sup> To have a more general approach at hand, a universal scaling law was developed, for which it was found that within good agreement particles which belong to the MA regime, follow a quadratic dependence on the diameter.<sup>98</sup> Namely it is

$$\frac{r_2^{ex}}{M^2} \phi_{int} = 11.6 \cdot 10^{-12} (2r_{SPIO}^{eff})^2 \quad (4.60)$$

where  $r_2^{ex}$  stands for the experimentally determined relaxivity. The left side stands for the experimentally determined values and the right side for the theoretically expected ones. If there is a perfect matching between the measured and simulated values, both sides would give the same result. Since all investigated SPIOs are in the MA regime, the scaling law can be used to compare the experimental and theoretical values. The values found are  $1.1 \cdot 10^{-9}$  and  $1.2 \cdot 10^{-9}$  for the left and right side of equation 4.60,  $1.8 \cdot 10^{-9}$  and  $3.8 \cdot 10^{-9}$ , and  $4.2 \cdot 10^{-9}$  and  $5.9 \cdot 10^{-9}$ , for S-8, S-16, and S-20, respectively. These results agree well with each other and the reported values in literature.<sup>98</sup> Again, for this theoretical approach systems have been found, which match poorly with the predicted values. Pothayee *et al.* found for their system, with a hydrophilic coating, that the scaling law underestimates the

experimental relaxivity by a factor of five.<sup>111</sup>

The next two systems are SPIO loaded nanoparticles. For both of them, the relaxivity is higher than for the single SPIOs S-8, due to the effect of clustered SPIOs.<sup>106, 109</sup> The simulations differ around 50% from the experimental results. Again it is very likely that the radius plays the crucial role here.

The last systems are nanocapsules, which have relaxivities that are in the area of the one for SPIOs and below the NPs. It is known, that vesicles like micellar and liposomic systems can have relaxivities that are not much higher than the one of the single SPIOs they have encapsulated.<sup>113, 114</sup> One can imagine that some loose aggregates form, but not permanent, which prevents the NCs having relaxivities as high as these of NPs. Unfortunately, it is not possible to gain any information on the SPIO distribution inside NCs. Clusters of SPIOs seen on TEM images are probably drying artifacts. Since the SPIO distribution inside NCs is highly dynamic, it is not possible to make any assumptions on the relaxation behavior. MC simulations have shown, that linear aggregates formed out of SPIOs can have relaxivities much smaller than the single SPIOs which are forming the linear aggregate.<sup>27</sup> When the relaxivities of the NCs are compared with  $r_2^{class}$  and  $r_2^{MC}$ , one notices that apart from one case,  $r_2^{class}$  heavily underestimates the relaxivity of nanocapsules. See also Figure 4.38, where the simulated relaxivities are plotted against their experimental counterpart. Whereas in the case of SPIOs and NPs there is only a slight deviation between the values from  $r_2^{class}$  and  $r_2^{MC}$ , the values for NCs differ a lot from each other, depending on the chosen simulation model. Since  $r_2^{MC}$  is more detailed about the given conditions, the matching between the simulated and the experimental values is improved. Though the deviations are still big, the unified approach gives a more realistic impression, whereas the computed values with the classical approach are off by a factor of 10 in comparison to  $r_2^{ex}$ . The deviation for both models might in parts be because of restricted diffusion inside the nanocapsules. Like discussed in the previous section, for  $T_1$  contrast agents this is known to change the outer sphere contribution.<sup>80</sup> It has already been shown, that this can have an unconsidered influence on the simulated relaxivity.<sup>111, 115</sup> Of course, erroneous results in size determination are again a source of wrongly estimated relaxivities. However, considering the complexity of the systems and the many assumptions made, it is already a success that the relaxivities can

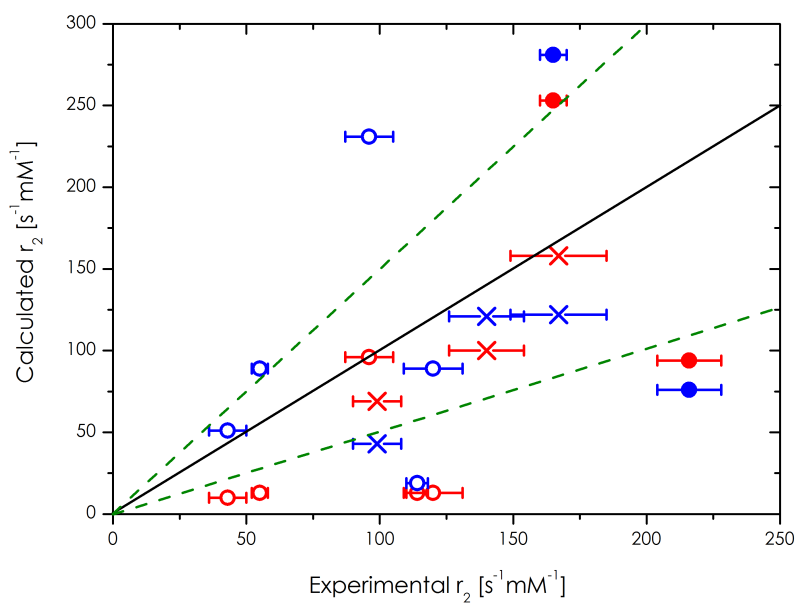


Figure 4.38: Transverse simulated relaxivities  $r_2^{class}$  (red) and  $r_2^{MC}$  (blue) plotted against the experimentally determined relaxivities  $r_2^{ex}$ . Crosses, filled circles, and hollow circles correspond to SPIOs, NPs, and NCs, respectively. The black line indicates perfect matching. The green dashed line borders the area of 50% deviation from  $r_2^{ex}$ . Error bars represent error on  $r_2^{ex}$ .

be estimated in the right order of magnitude.

---

## 5 Summary

The aim of this thesis was to investigate, understand and optimize nanocapsules as high relaxivity contrast agents. Two kinds of contrast agents were investigated:

Firstly, positive contrast agents, for which the starting point were nanocapsules, exhibiting relaxivities similar to that of commercially available contrast agents.<sup>18</sup> To avoid a trial and error approach, a very general concept of relaxivity was established by looking at the relaxivity in different polymer solutions. In this work it was shown, that with only a few assumptions, almost every relaxivity in solution could, at least qualitatively, be predicted by just taking the viscosity into account. The influence of the temperature as well as of the magnetic field strength was shown and simulations led to predictable results. Simulations also identified the microviscosity, rather than macroviscosity as the determining parameter for the relaxivity. The encapsulation of gadobutrol leads to high relaxivity values, up to a value of five times the relaxivity of neat gadobutrol. In this work it was shown, that the water exchange is of utmost importance for the relaxivity. By different techniques it has been shown, that the proton exchange has an upper limit of some hundred  $\mu\text{s}$ . Moreover, it was found out by high field  $^{17}\text{O}$  and NMR dispersion measurements that the origin of the high relaxivity is the restricted diffusion of water molecules in nanocapsules. The findings from the experiment and the simulation for solution, led to the development of capsules which have sucrose co-encapsulated and relaxivities which are increased ten times, in comparison to gadobutrol alone. Finally, as demonstrated by *in vitro* and *in vivo* experiments nanocapsules can give rise to a high local contrast in the MR image. In summary, in this work the source of high relaxivity nanocapsules was investigated and understood and led to an increase in relaxivity by a factor of ten and an increased contrast in *in vivo* imaging.

Secondly, nanocapsules have been investigated as  $T_2$  contrast agents. Three different classes, SPIOs, nanoparticles and nanocapsules have been investigated using two different approaches. One was the classical theoretical approach, the other one an unified approach based on a MC simulation. It has been shown, that the relaxivities for different morphologies

can be estimated with a semi-empirical approach, in which experimentally gained parameters were used to predict the relaxivity. By that, the relaxivity for SPIOs as well as for nanoparticles could be predicted qualitatively. It turned out, that the uncertainty in radius has a large influence on the results. However, for nanocapsules the different approaches led to very different results. In case of the classical theoretical approach, the unconsidered proton exchange plays a crucial role and leads to heavily underestimated relaxivities in nearly all cases. It was shown, that the unified approach, in which water or proton exchange is taken into account, gives a better agreement between simulation and experiment. Again, like in the case of  $T_1$  contrast agents, the proton exchange is a crucial factor in designing high relaxivity nanocapsules. It has also been shown, that nanocapsules can have relaxivities similar to the ones of clustered SPIOs in nanoparticles. The strength of nanocapsules is their combined use as both contrast agent and drug carrier, which can release their cargo through thermal decomposition and potentially other routes.<sup>33,116,117</sup> Therefore, one must get more insight into the relaxation rate behavior, for which the unified approach turned out to be a valuable method. In summary, in this work the different parameters, which lead to high relaxivity  $T_2$  contrast agents have been determined in a semi-empirical approach and successfully used to qualitatively predict the relaxivities.

---

## 6 Zusammenfassung

Das Ziel dieser Arbeit war es, Nanokapseln als Hochrelaxivitätskontrastmittel zu untersuchen, zu verstehen und zu optimieren. Es wurden zwei Arten von Kontrastmitteln untersucht:

Erstens wurden sogenannte positive Kontrastmittel untersucht, für welche der Ausgangspunkt Nanokapseln waren, mit Relaxivitäten ähnlich denen von bereits kommerziell erhältlichen Kontrastmitteln.<sup>18</sup> Um ein rein systematisches Ausprobieren zu vermeiden, wurde die Relaxivität zunächst ganz allgemein untersucht in verschiedenen Polymerlösungen. In dieser Arbeit konnte gezeigt werden, dass mit nur wenigen Annahmen, beinahe jede Polymerlösung und deren Relaxivität zumindest qualitativ gut beschrieben werden kann, indem lediglich die Viskosität als Parameter mitberücksichtigt wurde. Der Einfluss der Temperatur und des Magnetfeldes auf die Relaxivität wurde untersucht und konnte über Simulationen auch beschrieben werden. Desweiteren konnte über Simulationen gezeigt werden, dass die Mikroviskosität und nicht die Makroviskosität entscheidend ist für die Relaxivität. Die Verkapselung von Gadobutrol führt zu Relaxivitäten, welche bis zu sechs mal größer sind als die von reinem Gadovist. Es hat sich herausgestellt, dass der Protonenaustausch von höchster Wichtigkeit ist, damit Nanokapseln als Kontrastmittel funktionieren können. Über verschiedene Techniken wurde demonstriert, dass der Protonenaustausch schneller sein muss als ein paar hundert Mikrosekunden. Desweiteren haben <sup>17</sup>O und NMR Dispersion Messungen gezeigt, dass die Kapselwände zu einer Veränderung der Diffusion und damit zu einer erhöhten Relaxivität führen. Die Erkenntnisse, gefunden über Experimente und Simulationen in verschiedenen Polymerlösungen, führten zur Entwicklung von Kapseln, in welchen zusätzlich Zucker verkapselt ist. Dies wiederum führte dazu, dass die Relaxivität nochmal auf einen Faktor zehn gegenüber einfachem Gadovist gesteigert werden konnte. Zusammenfassend kann gesagt werden, dass in dieser Arbeit Nanokapseln untersucht und das Zustandekommen der hohen Relaxivität identifiziert und verstanden wurde. Dies führte zur Entwicklung von Kapseln mit einer Relaxivität, die zehnmal höher ist als die von Gadovist und einer Kontrasterhöhung in der Kernspintomographie.

Zweitens wurden Nanokapseln als negative Kontrastmittel untersucht. Drei verschiedene Arten wurden untersucht, nämlich superparamagnetische Eisenoxide, Nanopartikel in welchen superparamagnetische Eisenoxide einpolymerisiert wurden und Nanokapseln, in welchen superparamagnetische Eisenoxide verkapselt waren. Für die Simulation der Systeme wurden zwei Ansätze gewählt: Zum einen der klassische Ansatz über die sogenannte "outer sphere" Theorie und ein zweiter, sogenannter vereinheitlichter Ansatz, basierend auf MC-Simulationen. Die Relaxivitäten für die verschiedenen Arten von Kontrastmitteln und verschiedenen Morphologien konnten über einen semi-empirischen Ansatz abgeschätzt werden, in welchem experimentell erhaltene Daten genutzt wurden, um die Relaxivitäten vorherzusagen. Es hat sich herausgestellt, dass die Polydispersität einen großen Fehler in den Rechnungen verursacht, trotzdem konnte die Relaxivität von superparamagnetischen Eisenoxiden und auch von Nanopartikeln qualitativ bestimmt werden. Für Nanokapseln hingegen führten die zwei gewählten theoretischen Ansätze zu fundamental verschiedenen Ergebnissen. Mit den klassischen theoretischen Ansätzen führte der nicht berücksichtigte Wasser- bzw. Protonenaustausch zu stark unterschätzten Relaxivitäten. Der vereinheitlichte Ansatz hingegen, in welchem der Austausch von Protonen mit berücksichtigt wird, ergab eine Verbesserung in der Übereinstimmung zwischen Experiment und Simulation. Wie im Falle der  $T_1$  Kontrastmittel spielt der Protonenaustausch eine entscheidende Rolle für die Relaxivität von Nanokapseln. Desweiteren haben die Messungen ergeben, dass Nanokapseln Relaxivitäten haben können, welche mit denen von einfachen Eisenoxidpartikeln konkurrieren können. Der Vorteil der Nanokapseln liegt in der simultanen Nutzung als Kontrastmittel und Wirkstoffträger.<sup>33, 116, 117</sup> Daher ist es nötig, weitere Einsichten in das Relaxationsverhalten zu bekommen, für welche der vereinheitlichte Ansatz eine wertvolle Methode sein kann. Zusammenfassend konnte in dieser Arbeit gezeigt werden, dass über einen semi-empirischen Ansatz die Relaxivitäten von  $T_2$ -Kontrastmitteln, speziell auch Nanokapseln, qualitativ berechnet und vorhergesagt werden können.



---

## 7 Experimental and Simulations

### 7.1 Positive contrast agents

#### 7.1.1 Relaxivity in solution - Simulation

To compare the experimentally gained relaxivities with theoretical expectations, a semi empirical simulation based on SBM theory have been performed. For the outer sphere contribution the Hwang Freed model was used.

First, the parameters are taken from literature and set at the beginning. Please note, that the parameters are named according to according Matlab file 8.3.2, namely

$S = 7/2$  the electronic spin of Gd(III)<sup>9</sup>

$r = 3.1 \cdot 10^{-10}$  the distance in the inner sphere of gadolinium to water<sup>71</sup>

$p_m = 10^{-3}/55.56$  the mMol fraction of Metal ions per solvent molecule for 1 mM of gadolinium<sup>17</sup>

$A = 2.8 \cdot 10^6$  hyperfine coupling constant<sup>71</sup>

$d = 0.36 \cdot 10^{-9}$  distance of closest approach for outer sphere contribution<sup>71</sup>

$d_0 = 9 \cdot 10^{-10}$  estimated diameter of gadobutrol. Platzek *et al.* found that the volume  $V$  of the gadobutrol complex is  $2200 \text{ \AA}^3$ .<sup>118</sup> The diameter is approximated under the assumption, that the molecule is spherical with  $\frac{d_0}{2} = \sqrt[3]{\frac{3V}{4\pi}}$ .

$d_{H_2O} = 3 \cdot 10^{-10}$  diameter of H<sub>2</sub>O molecule<sup>119</sup>

$d_{suc} = 9.4 \cdot 10^{-10}$  diameter sucrose<sup>120</sup>

$\Delta_S = 37.2$  entropy of the activation process of the water exchange between inner sphere and bulk phase<sup>71</sup>

$\Delta_H = 47.4$  enthalpy of the activation process of the water exchange between inner sphere and bulk phase<sup>71</sup>

$\Delta = \frac{1.56 \cdot 10^{20}}{2.4}$  mean-square of the zero field splitting energy<sup>71</sup>

$t_{v298} = 6.5 \cdot 10^{-12}$  correlation time which modulates the electronic relaxation of the gadolinium<sup>71</sup>

Table 7.1: Viscosities for different sucrose concentrations and temperatures. The subscript at  $\eta$  indicates the wt% of sucrose in solution.

$T$ [K]	$\eta_0$ [mPas]	$\eta_{15}$ [mPas]	$\eta_{30}$ [mPas]	$\eta_{40}$ [mPas]	$\eta_{50}$ [mPas]	$\eta_{65}$ [mPas]
278	1.5	3.2	5.5	11.5	33.4	484.1
283	1.3	2.7	4.5	9.2	25.4	315.3
288	1.2	2.3	3.8	7.5	19.7	212.8
293	1.0	2.0	3.0	6.2	15.5	148.0
298	0.9	1.7	2.8	5.2	12.5	106.1
303	0.7	1.5	2.4	4.4	10.2	77.9
308	0.5	1.3	2.1	3.8	8.4	58.4
313	0.3	1.2	1.8	3.3	7.0	44.7

$\Delta E = 0.9$  the activation energy for  $t_{v298}$ <sup>71</sup>

After the parameters have been set, one can simulate the relaxivity, with the equations given in section 4.1.1.

In order to describe the relaxivity as a function of viscosity, the viscosities for different temperatures and sucrose concentrations are set. The values can again be found in literature.<sup>121</sup> They are summarized in Table 7.1.

Then the diffusion coefficient, for different temperatures  $T$  and different sucrose concentrations  $\eta$ , of water, sucrose molecule and the gadobutrol complex respectively is calculated, with help of

$$D = \frac{k_B T}{6\pi\eta d_i/2} \quad i \in \{H_2O, suc, gd\} \quad (7.1)$$

where  $d_i$  is the diameter of the water ( $H_2O$ ), the sucrose (suc), or the gadobutrol (gd) molecule, respectively. Then the spectral density functions are calculated. Since the sucrose molecules themselves are bearing protons, they contribute to the  $^1H$  signal. Hence, they need to be considered in the simulations, but only in the outer sphere contribution to relaxivity, because the sucrose molecule is too big to enter the first coordination sphere of the gadolinium complex, like it is known for  $Mn^{2+}$  nitrate.<sup>75</sup> Though one could argue, that for higher

sucrose concentrations the total amount of water decreases, which would affect the inner sphere contribution, one has to consider, that due to proton exchange of the -OH groups of sucrose and water, there is always water which can enter the inner sphere of the gadobutrol complex. It has also been shown, that the water exchange between the inner sphere and the bulk phase is unaffected by changes outside at the inner coordination sphere.<sup>74,122</sup> For the outer sphere contribution, one has to consider, that the sucrose molecules are diffusing slower than the water molecule, because of their size. Therefore, the amount of protons provided by water and by sucrose molecules have been calculated. First, the amount of protons stemming from water  $n_{H_2O}$  in solution has been calculated, with

$$n_{H_2O} = 2 \cdot \frac{100\% - wt\%}{100\%} \cdot 55.55 mol \quad (7.2)$$

where wt% is the weight percentage for the corresponding sucrose solution and the 2 is coming from the two protons of a water molecule. The 55.55 mol is the molarity of 1 l of water. Then, based on the wt% of sucrose, the number of protons coming from sucrose  $n_{suc}$  is calculated with

$$n_{suc} = 22 \cdot \frac{wt\% \cdot 1000}{M_{suc}} \quad (7.3)$$

where  $M_{suc} = 342$  g/mol is the molecular weight of sucrose and the 22 the number of protons coming from one sucrose molecule. Eventually, the fraction of protons actually coming from water is calculated with

$$c = \frac{n_{H_2O}}{n_{H_2O} + n_{suc}} \quad (7.4)$$

Then one can calculate two outer sphere contributions, one coming from the protons of the water molecules

$$R_{1,H_2O}^{OS} = c \cdot f(\tau_{D_{H_2O}}) \quad (7.5)$$

where  $f$  stands for the function describing the outer sphere term and  $\tau_{D_{H_2O}}$  the diffusional correlation time of water. And the second contribution stems from the sucrose

$$R_{1,suc}^{OS} = (1 - c) \cdot f(\tau_{D_{suc}}) \quad (7.6)$$

with  $\tau_{D_{suc}}$  denoting the diffusional correlation time of sucrose.

### 7.1.2 Relaxivity for different diffusion coefficients

To test ternary solutions other than gadobutrol, water and sucrose, the sucrose was replaced by different polymers. To calculate the relaxivity not based on the macroscopic viscosity but on the diffusion coefficients, again simulations based on the SBM theory with the OS described by the Hwang Freed model were performed. The code is shown in section 8.3.2. First, the diffusion coefficients of water found for several solutions are set in the beginning. In many cases, not the exact same conditions could be found but instead the diffusion coefficient for the system closest to the investigated one is used. The diffusion coefficients are listed in Table 7.2. For sucrose, water diffusion coefficients for 303 K, 323 K and 343 K are available. However, with a line fit it was found that the diffusion coefficient in this region behaves almost linearly. Therefore, the average of the diffusion coefficient for 303 K and 323 K was calculated. The same is true for Trehalose. For Dextran, different molecular weights, hence chain lengths were used, like 6k, 40k and 70k. However, the chain length showed no impact on the relaxivity, only the wt% made the difference and in fact, 10 wt% of 35k Dex and 10 wt% of 70k Dex give the same relaxivity. Therefore, the water diffusion coefficient found in a solution together with 70k Dex was used. The same is true for the PEG systems, again different chain lengths did not result in any difference in the relaxivities. For the PEG systems, only diffusion coefficients for 278 K and 333 K were found. However, the difference between the two temperatures was only about 10%.<sup>126</sup> Therefore, again the average of the diffusion coefficient found for 278 K and 333 K was calculated. For PVA two different degree of hydrolysis were used. But it was found that the water diffusion coefficient is not dependent on the degree of hydrolysis.<sup>127</sup> For all systems, the diffusion of the polymer was not considered. That is because only the relative diffusion of the gadobutrol complex and the polymer was considered, which is dominated by the much faster diffusion of the gadobutrol complex.

The microviscosity is then calculated with

$$\eta_{micro} = \frac{k_B \cdot T}{6\pi D_L r_{H_2O}} \quad (7.7)$$

where  $r_{H_2O}$  is the radius of a water molecule and  $D_L$  the diffusion coefficient of water like found in literature. With  $\eta_{micro}$  all other parameter depending on the viscosity are calculated, like the diffusion coefficient of the gadobutrol complex, the rotational correlation time and so

Table 7.2: Diffusion coefficients of water for different solutions.  $P$ : Polymer in solution;  $wt\%$ : weight percentage of polymer;  $P_L$ : Polymer found in literature;  $wt\%_L$ : Weight percentage found in literature;  $D$ : Diffusion coefficient found in literature. a.) Diffusion coefficient is the average of 303 K and 323 K. b.) The temperature was 298 K. c.) Diffusion coefficient is average of 278 K and 333 K. d.) Water diffusion is not depending on the degree of hydrolysis. For all: Please see details in the text.

$P$	$wt\%$	$P_L$	$wt\%_L$	$D \cdot 10^9$ [m <sup>2</sup> /s]
H <sub>2</sub> O <sup>123</sup>	100	H <sub>2</sub> O	100	2.9
Sucrose <sup>124</sup>	15	Sucrose <sup>a)</sup>	16	2.0
Sucrose <sup>124</sup>	30	Sucrose <sup>a)</sup>	32	1.3
Sucrose <sup>124</sup>	40	Sucrose <sup>a)</sup>	43	0.9
Sucrose <sup>124</sup>	50	Sucrose <sup>a)</sup>	55	0.5
Sucrose <sup>124</sup>	65	Sucrose <sup>a)</sup>	66	0.2
Trehalose <sup>124</sup>	10	Sucrose <sup>a)</sup>	16	1.9
Trehalose <sup>124</sup>	30	Sucrose <sup>a)</sup>	32	1.1
6k Dex <sup>125</sup>	3	70k Dex <sup>b)</sup>	3	1.6
40k Dex <sup>125</sup>	10	70k Dex <sup>b)</sup>	10	1.6
40k Dex <sup>125</sup>	20	70k Dex <sup>b)</sup>	25	1.2
40k Dex <sup>125</sup>	30	70k Dex <sup>b)</sup>	33	0.7
70K Dex <sup>125</sup>	5	70k Dex	3	1.7
70K Dex <sup>125</sup>	10	70k Dex	10	1.6
70k Dex <sup>125</sup>	35	70k Dex	33	0.6
0.4k PEG <sup>126</sup>	10	0.4k PEG <sup>c)</sup>	10	1.6
8k PEG <sup>126</sup>	10	20k PEG <sup>c)</sup>	10	1.6
35k PEG <sup>126</sup>	2	20k PEG <sup>c)</sup>	2	2.1
35k PEG <sup>126</sup>	6	20k PEG <sup>c)</sup>	6	1.6
35k Peg <sup>126</sup>	10	20k PEG <sup>c)</sup>	10	1.6
35k PEG <sup>126</sup>	20	20k PEG <sup>c)</sup>	20	1.2
35k PEG <sup>126</sup>	30	20k PEG <sup>c)</sup>	30	0.9
PVA 80% <sup>127</sup>	10	PVA <sup>d)</sup>	10	2.0
PVA 90% <sup>127</sup>	10	PVA <sup>d)</sup>	10	2.0

on. The rest is calculated as described above, again considering the outer sphere contribution separately for the polymer and the water.

### 7.1.3 Relaxivity for unloaded nanocapsules

To obtain a relaxivity for nanocapsules that actually have no gadobutrol encapsulated, the number of capsules in solution has been estimated based on the solid content. The sample has been freeze dried and the total weight of all nanocapsules  $m_{tot}$  measured. With an estimated density for the polymer composition  $\rho_p$  and the volume of the polymer shell  $V_{ps}$  with

$$V_{ps} = \frac{4}{3}\pi (r^3 - (r - d)^3) \quad (7.8)$$

where  $d$  is the thickness of the polymer shell and  $r$  the radius of the capsule. With that, the mass of one capsule  $m_{nc}$  can be calculated via

$$m_{nc} = \rho_p \cdot V_{ps} \quad (7.9)$$

The number of capsules in solution  $n_{nc}$  is then calculated as

$$n_{nc} = \frac{m_{tot}}{m_{nc}} \quad (7.10)$$

It has been found, that the number of capsules has around the same order of magnitude in case of capsules with and without gadobutrol inside. Hence, one can correlate unloaded nanocapsules to a certain gadolinium concentration.

### 7.1.4 In vivo experiments

For analyzing the *in-vivo* experiments ImageJ 1.48v has been used, a picture analyzing tool free of charge. With that, a region of interest (ROI) on an image is drawn and after that the intensity analyzed. Then, for different times, the intensity for a certain ROI can be analyzed and plotted against the time. By that, the change in signal intensity over time is analyzed.

---

## 8 Appendix

In the first two sections, the most important abbreviations and parameters are summarized. Then, the most important Matlab codes are shown.

### 8.1 Abbreviations

ARTDECO	Altered Relaxation Times Detect Exchange Correlation (NMR sequence for measuring Water exchange)
CA	Contrast Agent
CGS	Centimetre Gram Second (Metric system)
CPMG	Carr, Purcell, Meiboom, and Gill (NMR pulse sequence)
DAB	1,4-diamino butane
DAB-NC	Nanocapsules made from DAB in a ratio 1:1.5 to TDI, with 10 mM gadobutrol
DAE	1,2-diamino ethylene
DAE-NC	Nanocapsules made from DAE in a ratio 1:1.5 to TDI, with 10 mM gadobutrol
DAH	1,6-diamino hexane
DAH-NC	Nanocapsules made from DAH in a ratio 1:1.5 to TDI, with 10 mM gadobutrol
FDA	U.S. Food and Drug Administration
FID	Free Induction Decay (Signal in NMR)
MC	Monte Carlo
MRI	Magnetic Resonance Imaging
NC	Nanocapsule
NMR	Nuclear Magnetic Resonance
NMRD	Nuclear Magnetic Resonance Dispersion

NP	Nanoparticle
SBM	Solomon, Bloembergen, and Morgan (Relaxation theory)
SE	Spin Echo (MRI pulse sequence)
SPIO	Superparamagnetic Iron Oxide
TDI	2,4-toluene diisocyanate

## 8.2 Parameters

$B_0$	Static external magnetic field [T]
$\Delta\omega$	Difference in Larmor frequency between bulk and particle surface [Hz]
$[c]$	Concentration of contrast agents [mmol/L]
$\eta$	Viscosity [mPas]
$\gamma_I$	Nuclear gyromagnetic ratio [Hz/T]
$k_B$	Boltzmann constant [J/K]
$\mu_0$	Permeability of vacuum [Vs/Am]
$\mu_B$	Bohr magneton [J/T]
$\mu_{sp}$	Magnetic moment of one elementary iron oxide crystal [J/T]
$N_A$	Avogadro constant
$r_i$	Relaxivity with $i \in \{1, 2\}$ [ $s^{-1}mM^{-1}$ ]
$R_i$	Relaxation rate with $i \in \{1, 2\}$ [ $s^{-1}$ ]
$R_i^{dia}$	Diamagnetic relaxation rate with $i \in \{1, 2\}$ [ $s^{-1}$ ]
$T$	Absolute temperature [K]
$\tau_c$	Correlation time [s]
$\tau_D$	Diffusional correlation time [s]
$t_E$	Echo time [s]
$T_i$	Relaxation time with $i \in \{1, 2\}$ [s]
$\tau_m$	Residence time of water molecule at metal ion [s]
$\tau_r$	Rotational correlation time [s]
$\omega_{S,I}$	Larmor frequency of an electron (S) or a nucleus (I) [Hz]



## 8.3 Matlab code

Here the most important home written matlab codes which have been used are shown.

### 8.3.1 Automatic evaluation of relaxation times

This home written Matlab code has been used to automatically read in and evaluate  $T_1$  and  $T_2$  relaxation time measurements:

```

1 %% Automated evaluation of T1 and T2
2 %*****
3 %*   Sandro Ebert, 10/2012
4 %*****
5 %%
6 clc; clear all; close all;
7 %+++++
8 pathname_pro = 'C:\Work\MRI\T1 und T2 Messungen\Kerstin\001\001\';
9
10 T2_est = 100*10^3; %expected value for T2
11 %% Calculation
12 %%%%%%%%% Evaluation of T2 %%%%%%%%%
13
14 dir_name=[pathname_pro 'T2\'];
15 cd(dir_name);
16
17 file_name = 'tau.dat';
18 tau = dlmread(file_name);
19 npts = length(tau);
20
21 A=zeros(size(tau));
22 %% Reading parameters
23 for n=1:npts;
24     cd(dir_name)
25     file_name = ['EXP',num2str(n),'.00001.Par.Txt'];
26     fid = fopen( file_name,'r');    % open file mit Name fname
27     fseek(fid,0,'bof');            % Sets pointer at beginning of file
28     string = char(fread(fid,inf,'char'))';
29
30     s = strfind(string,'NECH'); %number of echos
31     if isempty(s)==0;
32         fseek(fid,s + 13,'bof');
33         NECH = str2double(char(fread(fid,4,'char'))');
34         else disp('Parameter "NECH" doesnt exist');

```

```

35     end
36
37     s = strfind(string, 'SI'); % SI
38     if isempty(s)==0;
39         for k = 1:2; % splits the resulting two pointer values
40             eval('s(k);'); % because SI matches different parameters
41         end
42         fseek(fid,s(1) + 12, 'bof'); % matching for 'SI', not the others
43         SI = str2double(char(fread(fid,4, 'char')));
44     else disp('Parameter "SI" doesnt exist');
45     end
46
47     %% Evaluation
48     data_name = 'T2.Dat';
49     c=dlmread(data_name);
50     s2(:,1)=c(:,n); s4 = zeros(SI,NECH); T = zeros(NECH,1);
51     laufindex = zeros(SI,1);
52
53     for i= 1:NECH % Integrating the echos
54         T(i,1) = 2*tau(n)*i;
55         for j = (i-1)*SI + 1: (i-1)*SI + SI;
56             l = j-(i-1)*SI;
57             s4(l,i) = s2(j,1);
58         end
59     end
60     %% Fitting
61
62     if SI == 1 %In case of only one point, sum(s4) is wrong
63         s3 = s4';
64     else
65         s3(:,1) = sum(s4);
66     end
67
68     T = dlmread('EXP1.00001.Dat.Txt');
69     T = T(:,1)*10^6;
70
71     e=zeros(3,1);
72     exp_t2='e(1)*exp(-T/e(2))+e(3)';
73
74     f=inline(exp_t2, 'e', 'T');
75
76     ev=[max(s3(:,1)), T2_est, min(s3(:,1))];
77
78     [fit,r,J,COVB]=nlinfit(T,s3(:,1),f, ev);

```

```

79
80     y=fit(1)*exp(-T/fit(2))+fit(3);
81
82     A(n,1)=fit(1);
83     A(n,2)=fit(2); % T2 time
84     A(n,3)=sqrt(COVB(2,2)); % standard error (Like in Origin 8.5)
85 end
86
87 % R2 for the single echos
88 R2=1./(A(:,2)/10^6);
89 error_R2 = (1./(A(:,2)./10^6).^2).*A(:,3)./10^6;
90
91 %%%%%%%%%%%%%%%%%%%%%%%%%%%%%%%%%%%%%%%%%%%%%%%%%%%%%%%%%%%%%%%%%%%%%%%%% Evaluation of T1 %%%%%%%%%%%%%%%%%%%%%%%%%%%%%%%%%%%%%%%%%%%%%%%%%%%%%%%%%%%%%%%%%%%%%%%%%
92 dir_name=[pathname_pro 'T1\'];
93 fname = [dir_name 'T1_invrec.dat'];
94 c=dlmread(fname);
95 [C,I] = min(c(:,3));
96
97 s=zeros(3,1);
98 exp_T1='s(1)*abs(1-2*exp(-c(:,1)/s(2))) + s(3)'; % For Inv-Rec Fit
99 f=inline(exp_T1,'s','c(:,1)');
100
101 ev_T1 = [-max(c(:,3)), c(length(c),1)/5, max(c(:,3))];
102
103 [fit_a,r,J,COVB,mse]=nlinfit(c(:,1),c(:,3),f, ev_T1);
104 z_T1=fit_a(1)*abs(1-2*exp(-c(:,1)/fit_a(2))) + fit_a(3);
105
106 T1=fit_a(2)/1000;
107 Delta_T1=sqrt(COVB(2,2))/1000;
108
109 R1=1/fit_a(2)*10^6;
110 Delta_R1 = 1/(T1/10^3)^2*(Delta_T1/1000);
111 %% Display
112 set(0,'DefaultFigureWindowStyle','docked');
113
114 fprintf(['T_2 [ms] = ',num2str(fit(2)/10^3,'%1.2f'), '\n']);
115 fprintf(['R_2 (averaged) [Hz] = ',num2str(R2_av,'%1.2f')...
116         , ' +/- ' num2str( error_R2_av,'%1.2f') '\n\n']);
117
118 fprintf(['T_1 [ms] = ',num2str(T1,'%1.2f')...
119         , ' +/- ' num2str(Delta_T1,'%1.2f') '\n']);
120 fprintf(['R_1 [Hz] = ',num2str(R1,'%1.2f')...
121         , ' +/- ' num2str(Delta_R1,'%1.2f') '\n\n']);
122

```

```

123 figure(4);
124 subplot(2,1,1)
125 plot(c(:,1)/10^6, c(:,3)), hold on; plot(c(:,1)/10^6,z_T1), hold off
126 title('T_1'); xlabel('Delay [s]'); ylabel('Signal intensity [a.u.]')
127 set(gcf, 'Color', 'w'); axis tight;
128
129 subplot(2,1,2)
130 plot(T, s3(:,1)); hold on; axis tight;
131 plot(T,y, 'r'), hold off; set(gcf, 'Color', 'w');
132
133 status = fclose( 'all'); % closes all open files

```

### 8.3.2 Relaxivity in solution for different viscosities

To calculate relaxivities for different solutions with Gadovist, based on diffusion coefficients, the following code has been used:

```

1 %% Calculation of relaxivity based on diffusion constants
2 %*****
3 %* Sandro Ebert, 2014
4 %*****
5 clc; close all; clear all;
6 %% Measured data
7 r1 = [2.8 4.1 8.7]'; % Measured relaxivity
8 etha = [1 4.1 8.7]*10^-3; % Macroviscosity
9 percprot = [1 0.83 0.66]'; % Percentage of molecule protons
10 percIS = [1 1 1]; % IS percentage
11 D = [2.9 2 1.3]*10^-9; % Experimental diffusion constant of H2O
12 D_mol = [0 20.6 18.2]*10^-11; % Exp. diffusion constant of molecule
13 d_mol = [0 9.4 9.4]*10^-10; % diameter molecule
14 %% Constants
15 S = 7/2; % spin
16 gamma_I = 2.675*10^8; % gyromagnetic ratio
17 mu_0 = 4*pi*10^-7; % permeability of vacuum
18 g = 2;
19 mu_B = 9.274*10^-24; % Bohr magneton
20 p_m = 10^-3/55.56; % mMol fraction of Metal ions
21 N_A = 6.02*10^23;
22 A = 2.8*10^6; % hyperfine coupling constant
23 r = 3.1*10^-10; % proton metal ion distance
24 d = 0.36*10^-9; % distance of closest approach (OS)
25 d_0 = 9*10^-10; % Diameter of Gadobutrol

```

```

26 d_mole      = 3.6*10^-10;           % dist. of closest approach molecule
27 d_H2O       = 3*10^-10;           % Diameter of H2O particle
28 k_B        = 1.38*10^-23;
29 R          = 8.314;
30 Delta_S    = 37.2;                % Entropy of the process
31 Delta_H    = 47.4*1000;           % Enthalpy of the process
32 h          = 6.62*10^(-34);       % Planck constant
33 Delta      = 1.56*10^20/2.4;       % ZFS Tensor
34 t_v298     = 6.5*10^-12;
35 Delta_E    = 0.9*1000;
36 B_0        = 1.5;                 % Main field [T]
37 T          = 310;                 % Temperature in K
38 %% zero functions
39 j=zeros(length(r1)); j2=zeros(length(r1)); R1_OS=zeros(1,length(r1));
40 R1=zeros(length(r1),4); a=zeros(length(r1),2); R1_S = zeros(length(r1));
41 j_mol =zeros(length(r1),1); j2_mol =zeros(length(r1),1);
42 a_mol =zeros(length(r1),2);
43 %% Calculation
44     omega = gamma_I*B_0; omega_s=657.4*omega;
45     C1 = 2/15 * (mu_0/(4*pi))^2 * gamma_I^2*g^2*mu_B^2*S*(S+1)/r^6;
46
47     etha2 = k_B*T./(6*pi.*D*d_H2O/2);
48     etha2(25) = k_B*T./(6*pi.*D_mol(25).*d_mol(25)/2);
49
50     t_v = t_v298*exp(Delta_E/R*(1/T - 1/298.15));
51     B = 1/ 25 * Delta * t_v * (4*S*(S+1) -3) * ...
52         ( 1/(1+omega_s^2*t_v^2) + 4/(1 + 4*omega_s^2*t_v^2));
53     C = 1/ 50 * Delta * t_v * (4*S*(S+1) -3)*...
54         (3 + 5/(1+omega_s^2*t_v^2) + 2/(1 + 4*omega_s^2*t_v^2));
55     T_e = 1/B; T_e2 = 1/C;
56
57     t_m = h/(k_B*T*exp(Delta_S/R - Delta_H/(R*T)));
58
59     for i=1:length(D_mol)
60         if D_mol(i) == 0
61             D_mol(i) = k_B*T/(6*pi*etha2(i)*d_mol(i)/2);
62         end
63     end
64
65     D_Gado = k_B*T./(6*pi.*etha2*d_0/2); %Diffusion Gadobutrol
66
67     D_mol = D_Gado + D_mol;
68     D      = D_Gado + D;
69

```

```

70     t_D = d^2./D; t_D_mol = d_mole^2./D_mol;
71     t_r = 4*pi*(d_0/2)^3.*etha2/(3*k_B*T);
72
73     z    = 1/t_m + 1./t_r + 1/T_e;    b = 1/t_m + 1./t_r + 1/T_e2;
74     t_c = 1./z; t_c2 = 1./b;
75     tau_e2 = 1/t_m + 1/T_e2;
76
77     for l = 1:length(r1);
78
79         a(l,1) = sqrt(1i*omega*t_D(l) + t_D(l)/T_e );
80         a(l,2) = sqrt(1i*omega_s*t_D(l) + t_D(l)/T_e2 );
81         a_mol(l,1) = sqrt(1i*omega*t_D_mol(l) + t_D_mol(l)/T_e );
82         a_mol(l,2) = sqrt(1i*omega_s*t_D_mol(l) + t_D_mol(l)/T_e2 );
83
84         j(1) = (4 + a(l,1) ) / ( 4 + 4*a(l,1) ...
85             + 21/9*a(l,1)^2 + 4/9*a(l,1)^3 );
86         j2(1) = (4 + a(l,2) ) / ( 4 + 4*a(l,2) ...
87             + 21/9*a(l,2)^2 + 4/9*a(l,2)^3 );
88
89         j_mol(1) = (4 + a_mol(l,1) ) / ...
90             ( 4 + 4*a_mol(l,1) + 21/9*a_mol(l,1)^2 + 4/9*a_mol(l,1)^3 );
91         j2_mol(1) = (4 + a_mol(l,2) ) / ...
92             ( 4 + 4*a_mol(l,2) + 21/9*a_mol(l,2)^2 + 4/9*a_mol(l,2)^3 );
93
94         R1_OS(l) = percprot(l)*32*pi/405* C1*15/2 * r^6 * N_A *...
95             real( 3 * j(1) + 7 * j2(1) ) / (d*D(l)) + ...
96             (1-percprot(l))*32*pi/405* C1*15/2 * r^6 *...
97             N_A * real( 3 * j_mol(1) + 7 * j2_mol(1) ) /...
98             (d_mole*D_mol(l));
99
100        R1_S(l) = 2/3*S*(S + 1)*A^2*( tau_e2^-1 /...
101            ( 1 + omega_s^2 * t_c2(l)^2 ) ); % Scalar contribution
102        R1(l,1) = C1 *( 3*t_c(l)/(1 + omega^2*t_c(l)^2 ) +...
103            7*t_c2(l)/(1 + omega_s^2 * t_c2(l)^2)); % dipolar contribution
104
105        R1(l,2) = p_m / ( 1/(R1(l,1) + R1_S(l)) + t_m ) + R1_OS(l); % r1
106    end
107
108    D_calc = k_B*T./(6*pi.*etha*d_H2O/2) + k_B*T./(6*pi.*etha*d_0/2);
109
110    %% Calculation with Macroviscosity
111    R1_MV=zeros(length(r1),4);
112
113    D_MV = k_B*T./(6*pi.*etha*d_H2O/2);

```

```

114
115     for i=1:length(D_mol)
116         D_mol(i) = k_B*T/(6*pi*etha(i)*d_mol(i)/2); %Diffusion molecule
117     end
118
119     D_Gado = k_B*T./(6*pi.*etha*d_0/2); %Diffusion Gadobutrol
120
121     D_mol = D_Gado' + D_mol;
122     D_MV    = D_Gado + D_MV;
123
124     t_D = d^2./D_MV;
125     t_D_mol = d_mole^2./D_mol;
126     t_r = 4*pi*(d_0/2)^3.*etha/(3*k_B*T);
127
128     z = 1/t_m + 1./t_r + 1/T_e;    b = 1/t_m + 1./t_r + 1/T_e2;
129     t_c = 1./z; t_c2 = 1./b;
130     tau_e2 = 1/t_m + 1/T_e2;
131
132     for l = 1:length(r1);
133
134         a(l,1) = sqrt(1i*omega*t_D(l) + t_D(l)/T_e );
135         a(l,2) = sqrt(1i*omega_s*t_D(l) + t_D(l)/T_e2 );
136         a_mol(l,1) = sqrt(1i*omega*t_D_mol(l) + t_D_mol(l)/T_e );
137         a_mol(l,2) = sqrt(1i*omega_s*t_D_mol(l) + t_D_mol(l)/T_e2 );
138
139         j(l) = (4 + a(l,1) ) / ...
140             ( 4 + 4*a(l,1) + 21/9*a(l,1)^2 + 4/9*a(l,1)^3 );
141         j2(l) = (4 + a(l,2) ) / ...
142             ( 4 + 4*a(l,2) + 21/9*a(l,2)^2 + 4/9*a(l,2)^3 );
143
144         j_mol(l) = (4 + a_mol(l,1) ) / ...
145             ( 4 + 4*a_mol(l,1) + 21/9*a_mol(l,1)^2 + 4/9*a_mol(l,1)^3 );
146         j2_mol(l) = (4 + a_mol(l,2) ) / ...
147             ( 4 + 4*a_mol(l,2) + 21/9*a_mol(l,2)^2 + 4/9*a_mol(l,2)^3 );
148
149         R1_OS(l) = percprot(l)*32*pi/405* C1*15/2 * r^6 * N_A *...
150             real( 3 * j(l) + 7 * j2(l) ) / (d*D(l)) + ...
151             (1-percprot(l))*32*pi/405* C1*15/2 * r^6 * N_A * ...
152             real( 3 * j_mol(l) + 7 * j2_mol(l) ) / ...
153             (d_mole*D_mol(l));
154
155         R1_S(l) = 2/3*S*(S + 1)*A^2*( tau_e2^-1 / ...
156             ( 1 + omega_s^2 * t_c2(l)^2 ) ); % Scalar contribution
157         R1(l,1) = C1 * ( 3*t_c(l)/(1 + omega^2*t_c(l)^2 ) + ...

```

```

158         7*t_c2(1)/(1 + omega_s^2 * t_c2(1)^2)); % dipolar contribution
159
160         R1_MV(1,2) = p_m / ( 1/(R1(1,1) + R1_S(1)) + t_m) + R1_OS(1);% r1
161     end
162
163     r1a = R1(:,2);
164     r1_MV = R1_MV(:,2);
165
166     quot = (r1a-r1)./r1*100;
167
168     dev = round(sum(abs(r1a-r1))/(length(r1a))*10)/10;
169     dev_MV = round(sum(abs(r1_MV-r1))/(length(r1_MV))*10)/10;
170
171     etha=etha*10^3;
172     %% Display
173
174     l=length(r1);
175     y=linspace(1,l,l); line = zeros(l,1); linegreen = 50*ones(l,1);
176     linegreen2 = 25*ones(l,1);
177
178     figure(3)
179     loglog(etha(1,l:1), D(1:l,1)); hold on; loglog(etha,D_calc); hold off;
180     legend({'Measured', 'Calculated'})
181     xlabel('Viscosity [mPas]'); ylabel('Diffusion constant [m^2/s]');
182
183     r1sort = r1; rlasort=r1a; r1_MVsort=r1_MV;
184     [etha,I] = sort(etha,2);
185     for i=1:length(I)
186         r1sort(i) = r1(I(i));
187         rlasort(i) = r1a(I(i));
188         r1_MVsort(i) = r1_MV(I(i));
189     end
190
191     figure(4)
192     semilogx(etha,r1sort); hold on; semilogx(etha,r1_MVsort); hold on;
193     semilogx(etha,rlasort); hold off;
194     xlabel('Viscosity [mPas]'); ylabel('Relaxivity [Hz/mM]'); axis tight;
195
196     figure(5)
197     semilogx(etha2*1000,r1); hold on; semilogx(etha2*1000,r1a); hold off;
198     title('\color{blue}SIM \color{black}vs. EXP')
199     xlabel('Calc. microviscosity [mPas]'); ylabel('Relaxivity [Hz/mM]');

```



### 8.3.3 Negative contrast agents - Matlab code

The code to calculate relaxivities for agglomerated SPIO systems and the theoretical relaxivity:

```

1 %% Calculation of relaxivity for agglomerated iron oxides
2 %*****
3 %*   Sandro Ebert, 2014
4 %*****
5 clc; close all; clear all;
6
7 mu_0    = 4*pi*10^-7; % permeability of vacuum
8 gamma_I = 2.675*10^8; % gyromagnetic ratio
9 % Measured r2:
10 R2_mess = [99, 140, 167, 216, 165, 49, 120, 114, 96, 55];
11 % Radius of NP:
12 a_exp   = [4.23, 8.05, 10.25, 73, 78, 125, 100, 200, 100, 100]*10^-9;
13 % Number of SPIOs/NP:
14 N_exp   = [1, 1, 1, 468, 3959, 33, 39, 959, 89, 24];
15 % concentration for 1 cubicmeter
16 C_exp   = [6830, 656, 368, 12.7, 1.2, 4.4, 11.2, 2, 9.9, 18.6]*10^16;
17 % Magnetization of SPIOs:
18 m       = [80, 62, 45, 80, 80, 45, 62, 80, 62, 62];
19 r_sp    = [4.23, 8.05, 10.25, 4.23, 4.23, ...
20           10.25, 8.05, 4.23, 8.05, 8.05]*10^-9;
21 % Density magnetite:
22 rho     = [5.1, 5.368, 5.1, 5.1, 5.1, 5.1, 5.368, 5.1, 5.368, 5.368]*10^3;
23 % Half of echo time:
24 TE      = [110, 110, 110, 110, 110, 110, 110, 110, 110, 110]*10^-6;
25 D       = [1.8, 2.9, 1.8, 1.8, 1.8, 1.8, 2.9, 1.8, 2.9, 2.9]*10^-9;
26 % To calculate with radius of NP:
27 s       = [1, 1, 1, 0, 0, 2, 2, 2, 2, 2];
28 q       = [1, 1, 1, 0, 0, 2, 2, 2, 2, 2];
29 d_SPIO  = 1*10^-9; % length coating
30 f_A     = N_exp.*C_exp.*4/3*pi.*r_sp.^3; % volume fraction
31 % Percentage of iron oxide in particle
32 corr    = [0.53, 0.71, 0.76, 0.09, 0.64, 0.05, 0.03, 0.04, 0.11, 0.03];
33
34 r_np = zeros(size(s)); delta_omega = zeros(size(s));
35
36 for i = 1:length(s)
37
38     if s(i) == 1

```

```

39
40     r_np(i) = r_sp(i)+d_SPIO;
41     f_A(i) = f_A(i)*r_np(i)^3/r_sp(i)^3*corr(i);
42     delta_omega(i) = mu_0*gamma_I*m(i)*rho(i)*r_sp(i)^3/(3*r_np(i)^3);
43
44     elseif s(i) == 0
45
46         r_np(i) = a_exp(i);
47         delta_omega(i) = mu_0*gamma_I*N_exp(i)*m(i)*rho(i)*r_sp(i)^3/...
48             (3*r_np(i)^3);
49         f_A(i) = C_exp(i)*4/3*pi*a_exp(i)^3*corr(i);
50
51     elseif s(i) == 2
52
53         r_np(i) = a_exp(i);
54         delta_omega(i) = mu_0*gamma_I*m(i)*N_exp(i)*rho(i)*r_sp(i)^3/...
55             (3*r_np(i)^3);
56         f_A(i) = corr(i)*C_exp(i)*4/3*pi*a_exp(i)^3;
57
58     end
59 end
60
61 tau_D_NP    = r_np.^2./D;
62 tau_sdr    = pi*sqrt(3)./(2.*delta_omega);
63 tau_L      = (1.49./delta_omega).*(delta_omega.*TE).^ (1/3).*...
64     (1.52 + f_A.*delta_omega.*TE).^ (5/3);
65
66 MR = zeros(size(s));
67
68 for i = 1:length(s)
69
70     if delta_omega(i) < 1/tau_D_NP(i) || q(i) == 1
71
72         MR(i) = 16/45*f_A(i)*delta_omega(i)^2*tau_D_NP(i);
73
74         % Test for scaling law behavior; th: theory, ex: experimental
75         th = R2_mess(i)*corr(i)/(m(i)*rho(i)*r_sp(i)^3/(r_np(i)^3))^2;
76         ex = 11.6*10^(-12)*(2*r_np(i)*10^9)^2;
77
78     elseif tau_D_NP(i) > tau_sdr(i) && tau_D_NP(i) < tau_L(i) || q(i) == 2
79
80         MR(i) = 2*pi*sqrt(3)* f_A(i)*delta_omega(i)/9;
81
82     elseif tau_D_NP(i) > tau_L(i) || q(i) == 3

```

```

83
84     MR(i) = 1.8*f_A(i)*(delta_omega(i)*TE(i))^(1/3)*...
85           (1.52 + f_A(i)*delta_omega(i)*TE(i))^(5/3)/tau_D_NP(i);
86
87     end
88 end
89 %% Calculation according to unified approach
90 a = 2.5209*10^12;
91 b = -0.177*10^9;
92 c = 0.1295*10^9;
93 d = 0.0523*10^9;
94 e = 0.0566*10^9;
95 z = 0.42;
96
97 s      = [1, 1, 1, 0, 0, 2, 2, 2, 2, 2];
98 B_eq = m.*rho.*(r_sp./(r_sp+d_SPIO)).^3.*mu_0/3;
99 f_A    = N_exp.*C_exp.*4/3*pi.*r_sp.^3;
100
101 R2 = zeros(1,10); B = zeros(3,10); f_bulk = zeros(1,10);
102 f_inner = zeros(1,10); R2_inner=zeros(1,10); R2_bulk=zeros(1,10);
103 p_bulk = zeros(1,10); p_inner = zeros(1,10);
104 for i = 1:length(s)
105
106     if s(i) == 1
107
108         f_A(i)    = f_A(i)*(r_sp(i) + d_SPIO)^3/r_sp(i)^3*corr(i);
109         B (1,i) = B_eq(i); r_np(i) = r_sp(i)+d_SPIO;
110         R2(i) = f_A(i)*(a*B(1,i)*r_np(i))^2/(1 + b*r_np(i)*B(1,i)^z + ...
111             (c*r_np(i)*B(1,i)^z)^2 + (d*r_np(i)*B(1,i)^z)^3 + ...
112             (e*r_np(i)*B(1,i)^z)^4 );
113
114     elseif s(i) == 0
115
116         B(2,i) = B_eq(i)*N_exp(i)*(r_sp(i)+d_SPIO)^3/a_exp(i)^3;
117         r_np(i) = a_exp(i);
118         f_A(i) = C_exp(i)*4/3*pi*a_exp(i)^3*corr(i);
119
120         R2(i) = f_A(i)*(a*B(2,i)*r_np(i))^2/(1 + b*r_np(i)*B(2,i)^z + ...
121             (c*r_np(i)*B(2,i)^z)^2 + (d*r_np(i)*B(2,i)^z)^3 + ...
122             (e*r_np(i)*B(2,i)^z)^4 );
123
124     elseif s(i) == 2
125
126         r_np(i) = r_sp(i) + d_SPIO;

```

```

127     B(3,i) = N_exp(i)*B_eq(i)*((r_sp(i)+d_SPIO)/a_exp(i))^3;
128     f_bulk(i) = C_exp(i)*4/3*pi*a_exp(i)^3*corr(i);
129
130     %For consideration of the right SPIOs
131     corr_2 = [0.53, 0.71, 0.76, .53, .53, .76, .71, .53, 0.71, 0.71];
132     f_inner(i) = N_exp(i)*(r_sp(i)+d_SPIO)^3/(a_exp(i)-15*10^-9)^3*...
133         corr_2(i);
134
135     R2_inner(1,i) = f_inner(i)*(a*B_eq(i)*r_np(i))^2/...
136         (1 + b*r_np(i)*B_eq(i)^z + (c*r_np(i)*B_eq(i)^z)^2 + ...
137         (d*r_np(i)*B_eq(i)^z)^3 + (e*r_np(i)*B_eq(i)^z)^4 );
138     R2_bulk(1,i) = f_bulk(i)*(a*B(3,i)*a_exp(i))^2/...
139         (1 + b*a_exp(i)*B(3,i)^z + (c*a_exp(i)*B(3,i)^z)^2 + ...
140         (d*a_exp(i)*B(3,i)^z)^3 + (e*a_exp(i)*B(3,i)^z)^4 );
141
142     p_bulk(1,i) = 1-C_exp(i)*4/3*pi*a_exp(i)^3;
143     p_inner(1,i) = 1-p_bulk(i) - N_exp(i)*4/3*pi*...
144         (r_sp(i)+d_SPIO)^3-C_exp(i)*4/3*pi*...
145         (a_exp(i)^3 - (a_exp(i)-15*10^-9)^3);
146
147     R2(i) = p_bulk(i)*R2_bulk(1,i) + p_inner(1,i)*R2_inner(1,i);
148
149     end
150 end
151 %% Display
152 display(round(MR.*1)./1)
153 display(round(R2.*1)./1)
154 %% Theoretical calculations
155 gamma_I = 2.675*10^8; % gyromagnetic ratio
156 mu_0 = 4*pi*10^-7; % permeability of vacuum
157 mu_B = 9.274*10^-24; % Bohr magneton
158 N_A = 6.02*10^23;
159 D = 2.27*10^-9; % relative diffusion coefficient
160 k_B = 1.38*10^-23; % Boltzmann constant
161 T = 310; % Absolute temperature
162 B_0 = 4.7; % static external field
163 V_EZ = 592.39*10^-30;% Volume of unit cell of one Fe3O4 crystal
164 mu_sp = 4.1*mu_B; % magnetic moment
165 Delta_omega = 0.5*gamma_I*(8*mu_sp/V_EZ)*mu_0/3; % Difference larmor freq.
166 C_a = 10^-6; % Agglomerate concentration
167 f_A = 5*10^-6; % volumetric fraction of NP
168 t_e = 100*10^-6; % Echo time
169
170 a2 = transpose(logspace(-9, -6, 150));

```

```

171 a = a2 + 0.30.*a2.*randn(size(a2));
172 tau_D = zeros(length(a),1); R2=zeros(length(a), 5);
173 x = zeros(length(a),2); N_g = zeros(length(a)); L = zeros(length(a),2);
174
175 for i = 1 : length(a)
176
177     tau_D(i) = a(i)^2/D;
178
179     if Delta_omega*tau_D(i) < 1
180
181         N_g(i)      = 8*4/3*pi*a(i)^3/V_EZ; % Number of elementary crystals
182         x(i,1)      = N_g(i)*mu_sp*B_0/(k_B*T);
183         L(i,1)      = coth(x(i)) - 1/x(i);
184
185         R2(i, 1) = (64*pi/135)*(mu_0*gamma_I*mu_sp*N_g(i)*L(i,1)/...
186             (4*pi))^2*(N_A*C_a)/(a(i)*D);
187
188     else
189         x = Delta_omega*t_e/2;
190
191         tau_L = (1.49/Delta_omega)*x^(1/3)*(1.52 + f_A(1)*x)^(5/3);
192
193         if tau_D < tau_L
194
195             R2(i, 1) = 2*pi*sqrt(3)*f_A(1)*Delta_omega/9;
196
197             else
198
199                 R2(i, 1) = 1.8*f_A(1)*x^(1/3)*(1.52 + f_A(1)*x)^(5/3)/...
200                     tau_D(i);
201                 R2(i, 3) = 2*pi*sqrt(3)*f_A(1)*Delta_omega/9; % T2*
202
203                 x = Delta_omega*2000*10^-6/2;
204                 R2(i, 4) = 1.8*f_A(1)*x^(1/3)*(1.52 + f_A(1)*x)^(5/3)/...
205                     tau_D(i);
206
207             end
208         end
209     end
210
211 figure(5)
212 plot(a2*10^9, R2(:, 1));
213 xlabel('Radius r [nm]');
214 ylabel('R2 [Hz]');

```

---

## Bibliography

- [1] Damadian, Raymond: *Tumor Detection by Nuclear Magnetic Resonance*. Science, 171:1151 – 1153, 1971.
- [2] Lauterbur, P. C.: *Image Formation by Induced Local Interactions: Examples Employing Nuclear Magnetic Resonance*. Nature, 242:190 – 191, 1973.
- [3] Hinshaw, W. S., P. A. Bottomley and G. N. Holland: *Radiographic thin-section image of the human wrist by nuclear magnetic resonance*. Nature, 270(5639):722–723, December 1977.
- [4] Carr, D. H., J. Brown, G. M. Bydder, H. J. Weinmann, U. Speck, D. J. Thomas and I. R. Young: *Intravenous Chelated Gadolinium as a Contrast Agent in Nmr Imaging of Cerebral-Tumors*. Lancet, 1:484 – 486, 1984.
- [5] Sylvia, H. Heywang, D. Hahn, H. Schmidt, I. Krischke, W. Eiermann, R. Bassermann and J. Lissner: *MR Imaging of the Breast Using Gadolinium-DTPA*. Journal of Computer Assisted Tomography, 10:199 – 204, 1986.
- [6] Weissleder, R.: *Molecular Imaging in Cancer*. Science, 312:1169 – 1171, 2006.
- [7] Graafen, Dirk, Sandro Ebert, Oliver Neudert, Lisandro Buljubasich, María Belén Franzoni, Jan Falk Dechent and Kerstin Münnemann: *Chapter Four - 1H NMR Spectroscopy and MR Imaging with Hyperpolarised Substances*. In Webb, Graham A. (editor): *Annual Reports on NMR spectroscopy*, volume 82 of *Annual Reports on {NMR} Spectroscopy*, pages 167 – 215. Academic Press, 2014.
- [8] Viswanathan, Subha, Zoltan Kovacs, Kayla N. Green, S. James Ratnakar and A. Dean Sherry: *Alternatives to Gadolinium-Based Metal Chelates for Magnetic Resonance Imaging*. Chemical Reviews, 110(5):2960–3018, 2010.
- [9] Caravan, P, J J. Ellison, T J. McMurry and R B. Lauffer: *Gadolinium(III) Chelates as MRI Contrast Agents: Structure, Dynamics, and Applications*. Chemical Reviews, 99(9):2293–2352, 1999.
- [10] Laurent, S., D. Forge, M. Port, A. Roch, C. Robic, L. Vander Elst and R. N. Muller: *Magnetic Iron Oxide Nanoparticles: Synthesis, Stabilization, Vectorization, Physicochemical Characterizations, and Biological Applications*. Chem. Rev., 108:2064 – 2110, 2008.
- [11] Pierre, Valérie C., Matthew J. Allen and Peter Caravan: *Contrast agents for MRI: 30+ years and where are we going?* JBIC Journal of Biological Inorganic Chemistry, 19(2):127–131, 2014.
- [12] Lauffer, Randall B.: *Paramagnetic metal complexes as water proton relaxation agents for NMR imaging: theory and design*. Chemical Reviews, 87(5):901–927, 1987.
- [13] Caravan, P.: *Strategies for increasing the sensitivity of gadolinium based MRI contrast agents*. Chem. Soc. Rev., 35:512 – 523, 2006.
- [14] Wiener, E., M. W. Brechbiel, H. Brothers, R. L. Magin, O. A. Gansow, D. A. Tomalia and P. C.

- Lauterbur: *Dendrimer-based metal chelates: A new class of magnetic resonance imaging contrast agents*. *Magnetic Resonance in Medicine*, 31(1):1–8, 1994.
- [15] Livramento, J. B., É. Tóth, A. Sour, A. Borel, A. Merbach and R. Ruloff: *High Relaxivity Confined to a Small Molecular Space: A Metallostar-Based, Potential MRI Contrast Agent*. *Angewandte Chemie International Edition*, 44(10):1480–1484, 2005.
- [16] Bolskar, R. D., A. F. Benedetto, L. O. Husebo, R. E. Price, E. F. Jackson, S. Wallace, L. J. Wilson and J. M. Alford: *First Soluble M@C60 Derivatives Provide Enhanced Access to Metallofullerenes and Permit in Vivo Evaluation of Gd@C60[C(COOH)2]10 as a MRI Contrast Agent*. *Journal of the American Chemical Society*, 125(18):5471–5478, 2003.
- [17] Ananta, J. S., B. Godin, R. Sethi, L. Moriggi, X. Liu, R. E. Serda, R. Krishnamurthy, R. Muthupillai, R. D. Bolskar, L. Helm, M. Ferrari, L. J. Wilson and P. Decuzzi: *Geometrical confinement of gadolinium-based contrast agents in nanoporous particles enhances T1 contrast*. *Nat Nano*, 5(11):815–821, November 2010.
- [18] Sharma, S., U. Paiphansiri, V. Hombach, V. Mailänder, O. Zimmermann, K. Landfester and V. Rasche: *Characterization of MRI contrast agent-loaded polymeric nanocapsules as versatile vehicle for targeted imaging*. *Contrast Media Mol. Imaging*, 5:59–69, 2010.
- [19] Duguet, E., S. Vasseur, S. Mornet and J. M. Devoisselle: *Magnetic nanoparticles and their applications in medicine*. *Nanomedicine*, 1:57 – 68, 2006.
- [20] Seo, W. Seok, J. H. Lee, X. Sun, Y. Suzuki, D. Mann, Z. Liu, M. Terashima, P. C. Yang, M. V. McConnell, D. G. Nishimura and H. Dai: *FeCo/graphitic-shell nanocrystals as advanced magnetic-resonance-imaging and near-infrared agents*. *Nat Mater*, 5(12):971–976, December 2006.
- [21] Jang, J., H. Nah, J. Lee, S. H. Moon, M. G. Kim and J. Cheon: *Critical Enhancements of MRI Contrast and Hyperthermic Effects by Dopant-Controlled Magnetic Nanoparticles*. *Angew. Chem. Int. Edn.*, 48:1234 – 1238, 2009.
- [22] Lee, N., Y. Choi, Y. Lee, M. Park, W. K. Moon, s. H. choi and T. Hyeon: *Water-Disperseble Ferri-magnetic Iron Oxide Nanocubes with Extremely High  $r_2$  Relaxivity for Highly Sensitive in Vivo MRI of Tumors*. *Nano Lett.*, 12:3127 – 3131, 2012.
- [23] Katz, E. and I. Willner: *Integrated nanoparticle-biomelecule hybrid systems: Synthesis, properties, and applications*. *Angew. chem. Int. Edn.*, 17:109 – 113, 2004.
- [24] Bannwarth, M. B., S. Ebert, M. Lauck, U. Ziener, S. Tomcin, G. Jakob, K. Münnemann, V. Mailänder, A. Musyanovych and K. Landfester: *Tailor-Made Nanocontainers for Combined Magnetic-Field-Induced Release and MRI*. *Macromolecular Bioscience*, 14:1205 – 1214, 2014.
- [25] Josephson, L., J. Lewis, P. Jacobs, P. F. Hahn and D. D. Stark: *The effects of iron oxides on proton relaxivity*. *Magn. Reson. Imag.*, 6:647 – 653, 1988.
- [26] Muller, R. N., P. Gillis, F. Moyny and A. Roch: *Transverse relaxivity of particulate MRI contrast media: from theories to experiments*. *Magn. Reson. Med.*, 22:178 – 182, 1991.
- [27] Vuong, Q. L., P. Gillis and Y. Gossuin: *Monte Carlo simulation and theory of proton NMR transverse*

- relaxation induced by aggregation of magnetic particles used as MRI contrast agents*. JMR, 212:139 – 148, 2011.
- [28] Abragam, A.: *The principles of nuclear magnetism*. Oxford University Press, 1961.
- [29] Keeler, J.: *Understanding NMR spectroscopy*. WILEY, 2005.
- [30] Haken, H. and H. C. Wolf: *Atom- und Quantenphysik*. Springer, 2000.
- [31] Levitt, M. H.: *Spin Dynamics - Basics of Nuclear Magnetic Resonance*. John Wiley & Sons, Ltd, 2008.
- [32] Villaraza, A. J. L., A. Bumb and M. W. Brechbiel: *Macromolecules, Dendrimers and nanomaterials in magnetic resonance imaging: The interplay between size, function and pharmacokinetics*. Chem. Rev., 110:2921 – 2959, 2010.
- [33] Mahmoudi, M., H. Hosseinkhani, M. Hosseinkhani, S. Boutry, A. Simchi, W. S. Journey, K. Subramani and S. Laurent: *Magnetic Resonance Imaging Tracking of Stem Cells in Vivo Using Iron Oxide Nanoparticles as a Tool for the Advancement of Clinical Regenerative Medicine*. Chem. Rev., 111:253 – 280, 2011.
- [34] J., Frenkel and J. Doefman: *Spontaneous and Induced Magnetisation in Ferromagnetic Bodies*. Nature, 126:274 – 275, 1930.
- [35] Bean, C. P. and J. D. Livingston: *Superparamagnetism*. Journal of Applied Physics, 30(4):S120–S129, 1959.
- [36] Demtroeder, W.: *Experimentalphysik 2: Elektrizität und Optik*. Springer, 2008.
- [37] Brown, M. A. and R. Semelka: *MRI: Basic Principles and Applications*. Wiley-Blackwell, 2010.
- [38] Clare, S.: *Functional MRI: Methods and Applications*. PhD thesis, University of Nottingham, 1997.
- [39] Bjarnason, T. A.: *Proof that  $gmT_2$  is the Reciprocal of  $gmR_2$* . Concepts in Magnetic Resonance Part A, 38A:128 – 131, 2011.
- [40] Meiboom, S. and D. Gill: *Modified Spin-Echo Method for Measuring Nuclear Relaxation Times*. Review of Scientific Instruments, 29(8):688–691, 1958.
- [41] McConville, P. and J.M. Pope:  *$^1H$  NMR  $T_2$  relaxation in contact lens hydrogels as a probe of water mobility*. Polymer, 42:3559 – 3568, 2001.
- [42] Liepinsh, E. and G. Otting: *Proton Exchange Rates from Amino Acid Side Chains - Implications for Image Contrast*. MRM, 35:30 – 42, 1996.
- [43] Davies, E., Y. Huang, J. B. Harper, J. M. Hook, D. S. Thomas, I. M. Burgar and P. J. Lillford: *Dynamics of water in agar gels studied using low and high resolution  $^1H$  NMR spectroscopy*. Int. Journ. Food Science Tech., 45:2502 – 2507, 2010.
- [44] Jerschow, Alexej and N. Müller: *Suppression of Convection Artifacts in Stimulated-Echo Diffusion Experiments. Double-Stimulated-Echo Experiments*. Journal of Magnetic Resonance, 125(2):372 – 375, 1997.
- [45] Posse, Stefan and Walter P Aue: *Susceptibility artifacts in spin-echo and gradient-echo imaging*. Journal of Magnetic Resonance (1969), 88(3):473 – 492, 1990.
- [46] Callaghan, P. T. and I. Furi: *Diffusion-diffusion correlation and exchange as a signature for local order*



- and dynamics. *The Journal of Chemical Physics*, 120(8):4032–4038, 2004.
- [47] Jeener, J., B. H. Meier, P. Bachmann and R. R. Ernst: *Investigation of exchange processes by two-dimensional NMR spectroscopy*. *The Journal of Chemical Physics*, 71(11):4546–4553, 1979.
- [48] Washburn, K. E. and P. T. Callaghan: *Tracking Pore to Pore Exchange Using Relaxation Exchange Spectroscopy*. *Phys. Rev. Lett.*, 97:175502, Oct 2006.
- [49] Kimmich, R.: *NMR Tomography Diffusometry Relaxometry*. Springer, 1997.
- [50] Kimmich, R. and E. Ansaldo: *Field-cycling NMR relaxometry*. *Prog. Nucl. Magn. Reson. Spectr.*, 44:257 – 320, 2004.
- [51] Neudert, Oliver, Carlos Mattea, Hans Wolfgang Spiess, Siegfried Stapf and Kerstin Munnemann: *A comparative study of  $^1\text{H}$  and  $^{19}\text{F}$  Overhauser DNP in fluorinated benzenes*. *Phys. Chem. Chem. Phys.*, 15:20717–20726, 2013.
- [52] Caravan, P., C. T. Farrar, L. Frullano and R. Uppal: *Influence of molecular parameters and increasing magnetic field strength on relaxivity of gadolinium- and manganese-based  $T_1$  contrast agents*. *Contrast Media & Molecular Imaging*, 4(2):89–100, 2009.
- [53] Bloembergen, N.: *Proton Relaxation Times in Paramagnetic Solutions*. *J. Chem. Phys.*, 27:572 – 573, 1957.
- [54] Solomon, I.: *Relaxation Processes in a System of Two Spins*. *Phys. Rev.*, 99(2):559–565, Jul 1955.
- [55] Bloembergen, N. and L. O. Morgan: *Proton relaxation times in paramagnetic solutions. Effects on electron spin relaxation*. *Journ. Chem. Phys.*, 34:842 – 850, 1961.
- [56] Laurent, Sophie, L. Elst, A. Roch and R. N. Muller: *Structure, synthesis and characterization of contrast agents for magnetic resonance molecular imaging*. In *NMR-MRI,  $\mu\text{SR}$  and Mössbauer Spectroscopies in Molecular Magnets*, pages 71–87. Springer Milan, 2007.
- [57] Laurent, S., L. Elst, A. Roch and R. N. Muller: *NMR - MRI,  $\mu\text{SR}$  and Mössbauer Spectroscopies in Molecular Magnets*. Springer, 2007.
- [58] Ayant, Y. and E. Belorizky: *Calcul des Densités Spectrales Résultant d'un Mouvement Aléatoire de Translation en Relaxation par Interaction Dipolaire Magnétique dans les Liquides*. *Le Journ. de Phys.*, 36:991 – 1004, 1975.
- [59] Freed, J. H.: *Dynamic effects of pair correlation functions on spin relaxation by translational diffusion in liquids. II. Finite jumps and independent  $T_1$  processes*. *J. Chem. Phys.*, 68:4034 – 4037, 1978.
- [60] Brooks, R. A.:  *$T_2$  shortening by Strongly Magnetized Spheres: A Chemical Exchange Model*. *Magn. Reson. Med.*, 47:388 – 391, 2002.
- [61] Tanaka, K.: *Self-diffusion Coefficients of Water in Pure Water and in Aqueous Solutions of Several Electrolytes with  $^{18}\text{O}$  and  $^2\text{H}$  as Tracers*. *J. Chem. Soc.*, 74:1879 – 1881, 1978.
- [62] Koenig, S. H.: *From the Relaxivity of  $\text{Gd}(\text{DTPA})^{2-}$  to Everything Else*. *Magn. Reson. Med.*, 22:183 – 190, 1991.
- [63] Pubanz, D., G. Conzales, D. Hugh Powell and A. E. Merbach: *Unexpectedly large change of water exchange rate and mechanism on  $[\text{Ln}(\text{DTPA-BMA})(\text{H}_2\text{O})]$  complexes along the Lanthanide(III) series*.

- Inorg. Chem., 34:4447 – 4453, 1995.
- [64] Aime, S., L. Frullano and S. Geninatti Crich: *Compartmentalization of a Gadolinium Complex in the Apoferritin Cavity: A Route To Obtain High Relaxivity Contrast Agents for Magnetic Resonance Imaging*. *Angewandte Chemie*, 114(6):1059–1061, 2002.
- [65] Mulder, W. J. M., G. J. Strijkers, G. A. F. van Tilborg, A. W. Griffioen and K. Nicolay: *Lipid-based nanoparticles for contrast-enhanced MRI and molecular imaging*. *NMR in biomedicine*, 19:142 – 164, 2006.
- [66] Wartenberg, N., P. Fries, O. Raccurt, A. Guillermo, D. Imbert and M. Mazzanti: *A Gadolinium Complex Confined in Silica Nanoparticles as a Highly Efficient T1/T2 MRI Contrast Agent*. *Chemistry A European Journal*, 19(22):6980–6983, 2013.
- [67] Rieter, W. J., J. S. Kim, K. M. L. Taylor, H. An, W. Lin, T. Tarrant and W. Lin: *Hybrid Silica Nanoparticles for Multimodal Imaging*. *Angewandte Chemie International Edition*, 46(20):3680–3682, 2007.
- [68] Davis, J. J., W.-Y. Huang and G.-L. Davies: *Location-tuned relaxivity in Gd-doped mesoporous silica nanoparticles*. *J. Mater. Chem.*, 22:22848–22850, 2012.
- [69] Zhang, Z., M. T. Greenfield, M. Spiller, T. J. McMurry, R. B. Lauffer and P. Caravan: *Multilocus Binding Increases the Relaxivity of Protein-Bound MRI Contrast Agents*. *Angewandte Chemie International Edition*, 44(41):6766–6769, 2005.
- [70] Nishiyabu, R., N. Hashimoto, T. Cho, K. Watanabe, T. Yasunaga, A. Endo, K. Kaneko, T. Niidome, M. Murata, C. Adachi, Y. Katayama, M. Hashizume and N. Kimizuka: *Nanoparticles of Adaptive Supramolecular Networks Self-Assembled from Nucleotides and Lanthanide Ions*. *J. Am. Chem. Soc.*, 131:2151 – 2158, 2009.
- [71] Laurent, S., L. Vander Elst and R. N. Muller: *Comperative study of the physicochemical properties of six clinical low molecular weight gadolinium contrast agents*. *Contr. Media & Molec. Imag.*, 1:128 – 137, 2006.
- [72] *Data Sheet Gadovist* .
- [73] Chen, John W., Robert B. Clarkson and R. Linn Belford: *Rotational Dynamics of MRI Paramagnetic Contrast Agents in Viscous Media*. *The Journal of Physical Chemistry*, 100(20):8093–8100, 1996.
- [74] Nicolle, G. M., É. Tóth, K-P Eisenwiener, H. R. Mücke and A.. Merbach: *From monomers to micelles: investigation of the parameters influencing proton relaxivity*. *JBIC Journal of Biological Inorganic Chemistry*, 7(7-8):757–769, 2002.
- [75] Vishnevskaya, G.P., A.F. Karimova and B.M. Kozyrev: *Electron paramagnetic relaxation in viscous Mn<sup>2+</sup> solutions*. *Journal of Structural Chemistry*, 12(1):33–37, 1971.
- [76] Rinck, P.: *Magnetic Resonance in Medicine. The Basic Textbook of the European Magnetic Resonance Forum*. N.A., 8th edition edition, 2014.
- [77] Lavalette, D, M. A. Hink, M. Tourbez, C. Tétreau and A. J. Visser: *Proteins as micro viscosimeters: Brownian motion revisited*. *European Biophysics Journal*, 35(6):517–522, 2006.

- [78] Malzahn, Kerstin: *Saccharide based nanocapsules - From monomer building blocks to improved capsules properties*. PhD thesis, Johannes Gutenberg University Mainz, 2014.
- [79] Platas-Iglesias, Carlos, L. Vander Elst, W. Zhou, R. N. Muller, C. F. G. C. Geraldes, T. Maschmeyer and J. A. Peters: *Zeolite GdNaY Nanoparticles with Very High Relaxivity for Application as Contrast Agents in Magnetic Resonance Imaging*. *Chemistry A European Journal*, 8(22):5121–5131, 2002.
- [80] Fries, Pascal H.: *Two-particle random walk simulation of outer-sphere nuclear relaxation*. *The Journal of Chemical Physics*, 132(22):–, 2010.
- [81] Price, W. S.: *Pulsed-field gradient nuclear magnetic resonance as a tool for studying translational diffusion: Part 1. Basic theory*. *Concepts in Magnetic Resonance*, 9(5):299–336, 1997.
- [82] Micskei, Károly, D. H. Powell, L. Helm, E. Brücher and A. E. Merbach: *Water exchange on [Gd(H<sub>2</sub>O)<sub>8</sub>]<sup>3+</sup> and [Gd(PDTA)(H<sub>2</sub>O)<sub>2</sub>]<sup>-</sup> in aqueous solution: A variable-pressure, -temperature and -magnetic field 17O NMR study*. *Magnetic Resonance in Chemistry*, 31(11):1011–1020, 1993.
- [83] Gonzalez, Gabriel, D. H. Powell, V. Tissieres and A. E. Merbach: *Water-exchange, electronic relaxation, and rotational dynamics of the MRI contrast agent [Gd(DTPA-BMA)(H<sub>2</sub>O)] in aqueous solution: a variable pressure, temperature, and magnetic field oxygen-17 NMR study*. *The Journal of Physical Chemistry*, 98(1):53–59, 1994.
- [84] Tóth, É, R. D. Bolskar, A. Borel, G. González, L. Helm, A. E. Merbach, B. Sitharaman and L. J. Wilson: *Water-Soluble Gadofullerenes: Toward High-Relaxivity, pH-Responsive MRI Contrast Agents*. *Journal of the American Chemical Society*, 127(2):799–805, 2005. PMID: 15643906.
- [85] Kimmich, R.: *Principles of Soft-Matter Dynamics*. Springer, 2012.
- [86] Csajbók, Éva, I. Bánayai, L. Vander Elst, R. N. Muller, W. Zhou and J. A. Peters: *Gadolinium(III)-Loaded Nanoparticulate Zeolites as Potential High-Field MRI Contrast Agents: Relationship Between Structure and Relaxivity*. *Chemistry Europe A European Journal*, 11(16):4799–4807, 2005.
- [87] Cole, William C., A. D. Leblanc and S. G. Jhingran: *The origin of biexponential T<sub>2</sub> relaxation in muscle water*. *Magnetic Resonance in Medicine*, 29(1):19–24, 1993.
- [88] Hills, B.P.: *The proton exchange cross-relaxation model of water relaxation in biopolymer systems*. *Molecular Physics*, 76(3):489–508, 1992.
- [89] Vasalatiy, O., P. Zhao, S. Zhang, S. Aime and A. D. Sherry: *Catalytic effects of apoferritin interior surface residues on water proton exchange in lanthanide complexes*. *Contrast Media & Molecular Imaging*, 1(1):10–14, 2006.
- [90] Cheng, Zhiliang, Daniel L. J. Thorek and Andrew Tsourkas: *Porous Polymersomes with Encapsulated Gd-Labeled Dendrimers as Highly Efficient MRI Contrast Agents*. *Advanced Functional Materials*, 19(23):3753–3759, 2009.
- [91] Swift, T. J. and R. E. Connick: *NMR-Relaxation Mechanisms of O<sub>17</sub> in Aqueous Solutions of Paramagnetic Cations and the Lifetime of Water Molecules in the First Coordination Sphere*. *The Journal of Chemical Physics*, 37(2):307–320, 1962.
- [92] Hoehn, M., E. Küstermann, J. Blunk, D. Wiedermann, T. Trapp, S. Wecker, M. Föcking, H. Arnold,

- J. Hescheler, B. K. Fleischmann, W. Schwindt and C. Bührle: *Monitoring of implanted stem cell migration in vivo: A highly resolved in vivo magnetic resonance imaging investigation of experimental stroke in rat*. Proceedings of the National Academy of Sciences, 99(25):16267–16272, 2002.
- [93] Regatte, R. R., S. V. S. Akella, A. Borthakur, J. B. Kneeland and R. Reddy: *In Vivo Proton MR Three-dimensional T1 $\rho$  Mapping of Human Articular Cartilage: Initial Experience*. Radiology, 229(1):269–274, 2003. PMID: 14519880.
- [94] Ebert, S., M.B. Bannwarth, A. Musyanovich, K. Landfester and K. Münnemann: *How Morphology Influences Relaxivity - Comparative Study of Superparamagnetic Iron Oxide/Polymer Hybrid Nanostructures*. Contrast Media and Molecular Imaging, DOI: 10.1002/cmml.1648, 2015.
- [95] Bannwarth, Markus B.: *Smart Magnetic Dispersions - From Switchable Release to Well-Defined Hybrid Nanofibers*. PhD thesis, Johannes Gutenberg University Mainz, 2014.
- [96] Hu, F., H. M. Joshi, V. P. Dravid and T. J. Meade: *High-performance nanostructured MR contrast probes*. Nanoscale, 2:1884 – 1891, 2010.
- [97] Ai, H., C. Flask, B. Weinberg, X. Shuai, M. Pagel, D. Farrell, J. Duerk and J. Gao: *Magnetite-Loaded Polymeric Micelles as Ultrasensitive Magnetic-Resonance Probes*. Advanced Materials, 17:1949 – 1952, 2005.
- [98] Vuong, Q. L., J. Berret, J. Fresnais, Y. Gossuin and O. Sandre: *A Universal Scaling Law to Predict the Efficiency of Magnetic Nanoparticles as MRI T<sub>2</sub>-Contrast Agents*. Adv. Healthcare Mater., 1:502 – 512, 2012.
- [99] LaConte, L. E.W., N. Nitin, O. Zurkiya, D. Caruntu, C. J. O'Connor, X. Hu and G. Bao: *Coating thickness of magnetic iron oxide nanoparticles affects R<sub>2</sub> relaxivity*. Journal of Magnetic Resonance Imaging, 26(6):1634–1641, 2007.
- [100] Brooks, R. A., Moyny F. and Gillis P.: *On T<sub>2</sub> shortening by Weakly Magnetized Particles: The Chemical Exchange Model*. Magn. Reson. Med., 45:1014 – 1020, 2001.
- [101] Gillis, P., F. Moyny and R. A. Brooks: *On T<sub>2</sub> shortening by Strongly Magnetized Spheres: A Partial Refocusing Model*. Magn. Reson. Med., 47:257 – 263, 2002.
- [102] Roch, A., Y. Gossuin, R. N. Muller and P. Gillis: *Superparamagnetic colloid suspensions: Water magnetic relaxation and clustering*. Journ. Magn. Mat., 293:532 – 539, 2005.
- [103] Lowery, T.: *Magnetic Nanomaterials*. Wiley-VCH, 2009.
- [104] Brown, R. J. S.: *Distribution of Fields from Randomly Placed Dipoles: Free-Precession Signal Decay as Result of Magnetic Grains*. Physical Review, 121:1379 – 1382, 1961.
- [105] Xu, Fenghua, C. Cheng, F. Xu, C. Zhang, H. Xu, X. Xie, D. Yin and H. Gu: *Superparamagnetic magnetite nanocrystal clusters: a sensitive tool for MR cellular imaging*. Nanotechnology, 20(40):405102, 2009.
- [106] Min, C., H. Shao, M. Liong, T. Yoon, R. Weissleder and H. Lee: *Mechanism of Magnetic Relaxation Switching Sensing*. ACS Nano, 6:6821 – 6828, 2012.
- [107] Chen, Y., C. Hsieh, C. Lin and D. Hwang: *NMR relaxation study of water dynamics in superpara-*

- magnetic iron-oxide-loaded vesicles*. The Journal of Chemical Physics, 138:064502–1 – 064505–8, 2013.
- [108] Carroll, M. R. J., R. C. Woodward, M. J. House, W. Y. Teoh, R. Amal, T. L. Hanley and T. G. St. Pierre: *Experimental validation of proton transverse relaxivity models for superpara nanoparticl MRI contrast agents*. Nanotechnology, 21:7, 2010.
- [109] Pösel, E., H. Kloust, U. Tromsdorf, M. Janschel, C. Hahn, C. Maßlo and H. Weller: *Relaxivity Optimization of a PEGylated Iron-Oxide-Based Negative Magnetic Resonance Contrast Agent for T<sub>2</sub>-Weighted Spin-Echo Imaging*. ACS Nano, 6:1619 – 1624, 2012.
- [110] Tong, S., S. Hou, Z. Zheng, J. Zhou and G. Bao: *Coating optimization of Superparamagnetic Iron Oxide Nanoparticles for High T<sub>2</sub> Relaxivity*. Nano Letters, 10:4607 – 4613, 2010.
- [111] Pothayee, N., S. Balasubramaniam, N. Pothayee, N. Jain, N. Hu, Y. Lin, R. M. Davis, N. Sriranganathan, A. P. Koretsky and J. S. Riffle: *Magnetic nanoclusters with hydrophilic spacing for dual drug delivery and sensitive magnetic resonance imaging*. J. Mater. Chem. B, 1:1142–1149, 2013.
- [112] Jun, Y.-W., Y.-M. Huh, J.-s. Choi, J.-H. Lee, H.-T. Song, S. Yoon, K.-S. Kim, J.-S. Shin, J.-S. Suh and J. Cheon: *Nanoscale Size Effect of Magnetic Nanocrystals and Their Utilization for Cancer Diagnosis via Magnetic Resonance Imaging*. Journal of the American Chemical Society, 127(16):5732–5733, 2005.
- [113] Martina, M., J. Fortin, C. Ménager, O. Clément, G. Barratt, C. Grabielle-Madelmont, G. Florence, V. Cabuil and S. Lesieur: *Generation of Superparamagnetic Liposomes Revealed as Highly Efficient MRI Contrast Agents for in Vivo Imaging*. JACS, 127:10676 – 10685, 2005.
- [114] Larsen, B. A., M. A. Haag, N. J. Serkova, K. R. Shroyer and C. R. Stoldt: *Controlled aggregation of superparamagnetic iron oxide nanoparticles for the development of molecular magnetic resonance imaging probes*. Nanotechnology, 19:265102, 2008.
- [115] Haan, H. W. de and C. Paquet: *Enhancement and degradation of the R<sub>2</sub><sup>\*</sup> relaxation rate resulting from the encapsulation of magnetic particles with hydrophilic coatings*. Magnetic Resonance in Medicine, 66(6):1759–1766, 2011.
- [116] Katagiri, K., Y. Imai, K. Koumoto, T. Kaiden, K. Kono and S. Aoshima: *Magneto-responsive On-Demand Release of Hybrid Liposomes Formed from Fe<sub>3</sub>O<sub>4</sub> Nanoparticles and Thermosensitive Block Copolymers*. Small, 7(12):1683–1689, 2011.
- [117] Hu, S. H., S. Y. Chen and X. H. Gao: *Multifunctional Nanocapsules for Simultaneous Encapsulation of Hydrophilic and Hydrophobic Compounds and On-Demand Release*. ACS Nano, 6:2558 – 2565, 2012.
- [118] Platzek, J., P. Blaszkiewicz, H. Gries, P. Luger, G. Michl, A. Müller-Fahrnow, B. Radüchel and D. Sülzle: *Synthesis and Structure of a New Macrocyclic Polyhydroxylated Gadolinium Chelate Used as a Contrast Agent for Magnetic Resonance Imaging*. Inorganic Chemistry, 36(26):6086–6093, 1997.
- [119] Abel, S., F. Sterpone, S. Bandyopadhyay and M. Marchi: *Molecular Modeling and Simulations of AOT - Water Reverse Micelles in Isooctane: Structural and Dynamic Properties*. The Journal of Physical Chemistry B, 108(50):19458–19466, 2004.

- [120] Lebrun, L. and G.-A. Junter: *Diffusion of sucrose and dextran through agar gel membranes*. Enzyme and Microbial Technology, 15(12):1057 – 1062, 1993.
- [121] Asadi, Mosen: *Beet-Sugar Handbook*. John Wiley & Sons, Inc., 2005.
- [122] Tóth Éva, L. Burai and A. E. Merbach: *Similarities and differences between the isoelectronic GdIII and EuIII complexes with regard to MRI contrast agent applications*. Coordination Chemistry Reviews, 216-217(0):363 – 382, 2001.
- [123] Holz, Manfred, S. R. Heil and A. Sacco: *Temperature-dependent self-diffusion coefficients of water and six selected molecular liquids for calibration in accurate 1H NMR PFG measurements*. Phys. Chem. Chem. Phys., 2:4740–4742, 2000.
- [124] Ekdawi-Sever, N., J. J. de Pablo, E. Feick and E. von Meerwall: *Diffusion of Sucrose and  $\alpha,\alpha$ -Trehalose in Aqueous Solutions*. The Journal of Physical Chemistry A, 107(6):936–943, 2003.
- [125] Brown, W., P. Stilbs and R. M. Johnsen: *Self-diffusion and sedimentation of dextran in concentrated solutions*. Journal of Polymer Science: Polymer Physics Edition, 20(10):1771–1780, 1982.
- [126] Nilsson, Per Gunnar and B. Lindman: *Water self-diffusion in nonionic surfactant solutions. Hydration and obstruction effects*. The Journal of Physical Chemistry, 87(23):4756–4761, 1983.
- [127] Petit, J.-M., X. X. Zhu and P. M. Macdonald: *Solute Probe Diffusion in Aqueous Solutions of Poly(vinyl alcohol) As Studied by Pulsed-Gradient Spin-Echo NMR Spectroscopy*. Macromolecules, 29(1):70–76, 1996.

---

## Lebenslauf

[Redacted]

[Redacted]	[Redacted]
[Redacted]	[Redacted]
[Redacted]	[Redacted]
[Redacted]	[Redacted]
[Redacted]	[Redacted]
[Redacted]	[Redacted]

[Redacted]  
[Redacted]

[Redacted]	[Redacted]
[Redacted]	[Redacted]
[Redacted]	[Redacted]
[Redacted]	[Redacted]
[Redacted]	[Redacted]
[Redacted]	[Redacted]
[Redacted]	[Redacted]
[Redacted]	[Redacted]
[Redacted]	[Redacted]
[Redacted]	[Redacted]
[Redacted]	[Redacted]
[Redacted]	[Redacted]
[Redacted]	[Redacted]

[Redacted]  
[Redacted]  
[Redacted]

### Publikationen zur Doktorarbeit in Peer-Review Journals

1. K. Malzahn<sup>‡</sup>, S. Ebert<sup>‡</sup>, I. Schlegel, O. Neudert, M. Wagner, G. Schütz, A. Ide, F. Roohi, K. Münnemann, D. Crespy, K. Landfester  
"Increasing Relaxivity of Magnetic Resonance Contrast Agents induced by confinement in Semipermeable Nanocapsules"  
Advance Materials Healthcare, currently under review, 2015  
<sup>‡</sup>: Authors contributed equally.
2. S. Ebert, M. B. Bannwarth, A. Musyanovych, K. Landfester, K. Münnemann  
"How Morphology Influences Relaxivity - Comparative Study of Superparamagnetic Iron Oxide/Polymer Hybrid Nanostructures"  
Contrast Media and Molecular Imaging, DOI: 10.1002/cmimi.1648, 2015
3. M.B. Bannwarth, S. Utech, S. Ebert, D. A. Weitz, D. Crespy, K. Landfester  
"Colloidal polymers with controlled sequence and branching constructed from magnetic field assembled nanoparticles"  
ACS Nano, 9: 2720 - 2728, 2015
4. M. B. Bannwarth, S. Ebert, M. Lauck, U. Ziener, S. Tomcin, G. Jakob, K. Münnemann, V. Mailänder, A. Musyanovych, K. Landfester  
"Tailor-Made Nanocontainers for Combined Magnetic-Field-Induced Release and MRI"  
Macromolecular Bioscience, 14: 1205 - 1214, 2014



---

## Acknowledgment

[Redacted text block containing multiple lines of obscured content]

[Redacted text block]